Università degli studi di Trento

DEPARTMENT OF MATHEMATICS

MASTER DEGREE IN MATHEMATICS

A computational study of the effect of the guide wire on the pressure drop in coronary stenosis

Supervisors:

Prof. Giorgio Rosatti
Prof. Christian Vergara

Graduant:

Patrizia Pretti

Assistant Supervisors:

Dott. Roberto Bonmassari (*Ospedale S. Chiara, Trento*)
Ing. Silvia Pozzi

DATE OF DISCUSSION: 18 JULY 2018

Contents

Introduction

Nowadays, cardiovascular disease has become one of the major cause of death in the world. In this context, an important role is played by coronary stenosis, a narrowing in the lumen blood vessel which, depending on its severity, can lead to myocardium infarction. Clinicians base the decision for medical treating principally on a diagnostic index: the FFR (Fractional Flow Reserve). This value is obtained in hospitals through invasive measurements of the trans-stenotic pressure drops by means of a pressure guide wire.

The aim of our work is to evaluate, with numerical experiments, the possible effects of the guide wire on the pressure drop in a real coronary stenosis. On this purpose, we compare numerical results obtained with two different configutations: a stenotic model with and without guide wire. To carry out this kind of work we firstly proceed by reconstructing the stenotic vessel from clinical radiological images, then we generate the meshes necessary for the computer simulations and, finally, we perform the simulations with appropriate boundary conditions, collecting the results obtained. More precisely, we divide our work in five chapters.

In Chapter 1 we present the physiological features of the clinical problem, specifying how the cardiovascular system works. Then we describe the diseases linked to the formation of atherosclerotic plaques and the diagnostic indexes used by clinicians to understand the gravity of the situation.

In Chapter 2 we translate the medical problem into the mathematical one. We describe the Navier-Stokes equations and the steps necessary to reach the weak formulation of the problem, which represent the starting point towards a Finite Element approximation. Then, in the second part, we describe our choices regarding the numerical approximation of the problem.

In Chapter 3 we present the tools and the steps necessary for the reconstruction of the stenotic vessel from medical images and for the generation of the mesh for the two case analyzed: our model with and without guide wire.

In Chapter 4 we describe the physical and computational settings, explaining in details our choices regarding boundary conditions. Then, we present our numerical results and we make some considerations on them.

Finally, in Chapter 5 we conclude our work by describing the limitations of our study and the possible future developments which could lead to better results.

The realization of this work was possible thanks to the collaboration with the MOX Laboratory of the Politecnico di Milano, which provided the tools for the numerical simulation and, in general, help and support for the computational part. Another important contribute for us comes from the collaboration with the Santa Chiara Hospital in Trento and U.O Multizonale di Radiologia del Distretto Est dell'APSS di Trento. In particular, we want to thank Doctor Roberto Bonmassari for his hints and support in the clinical part.

Chapter 1

The clinical problem

In this first chapter we are going to describe the main physiological properties of the cardiovascular system with the aim of better understanding the clinical problem of our interest. We focus our attention on heart's functions and coronary disease, presenting the implications for human life and the measures adopted by clinicians to treat and prevent these situations.

1.1 The cardiovascular system

The cardiovascular system consists of three components: blood, the heart and blood vessels. We can describe its work by listing its three main functions: it delivers oxygen and nutrients to the tissues and carries waste products to the organs responsible for elimination, it defends the body against foreign microbes and it regulates the body temperature.

According to the blood's path, the cardiovascular circulation consists of two different closed circuits, the *systemic circulation* and the *pulmonary circulation*, which are arranged in series: the output of one becomes the input of the other. The pulmonary circuit transports blood to and from the lungs, where it picks up oxygen and delivers carbon dioxide for exhalation. The systemic circuit, instead, transports oxygenated blood to all of the tissues of the body and returns deoxygenated blood to the heart to be sent back to the pulmonary circulation.

In the following subsections we try to give a brief description of the main features of these three important components of human body.

1.1.1 The blood

Blood is a liquid connective tissue, which has three general functions: it contributes to homeostasis by transporting oxygen, carbon dioxide and nutrients to and from body's cells (*transportation*), it helps regulate body pH and temperature (*regulation*) and it provides protection against diseases (*protection*).

Blood is denser and more viscous than water and it is composed by two components: **blood plasma** (55%) and **formed elements** (45%), see Figure 1.1. Blood plasma is about 91.5% water and 8.5% solutes, most of which are proteins, which includes albumins, globulins and fibrogen. The formed elements includes three principal components: red blood cells (RBCs), white blood cells (WBCs) and platelets. RBCs are biconcave discs with a diameter of 7-8 micron. They are highly specialized for the oxygen transport function because they have no nucleous and so all their internal space is available for oxygen transport. WBCs

have nuclei, do not contain hemoglobin and cover an important role in protecting the body against infectious diseases (they are the cells of the immune system). The platelets are cells fragments without cell nucleus, whose main function is to react to bleeding from blood vessels injury [3].

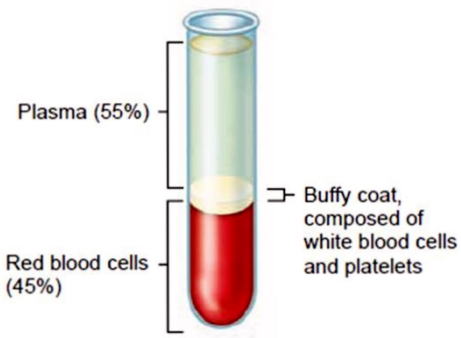

Figure 1.1: Composition of the blood.

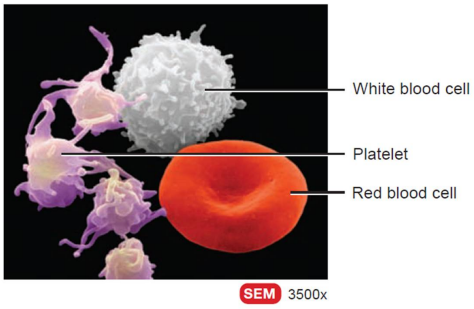

Figure 1.2: Scanning electron micrograph of the formed elements.

1.1.2 The heart

The heart is a powerful muscle slightly larger than a clenched fist located within the thoracic cavity. It works as a pump to send oxygen-rich blood through all the parts of the body.

It consists of four chambers and it is divided in two parts, the left side and the right side, each have one atrium and one ventricle. Each of the two superior chambers (the *right atrium* and the *left atrium*) acts as a receiving chamber and contracts to push blood into the lower chambers, the *right ventricle* and the *left ventricle*, whose role is to be the primary pump of the heart.

The so-called *atrioventricular valves* are the connection between atria and ventricles, in particular we have the *mitral valve* in the left heart and the *tricuspid valve* in the right heart. These valves play an important role, because, depending on their state (open or close), they allow or prevent the blood transfer form the atria to ventricles. All the four chambers are connected to the circulatory system. These connections are provided by the *aorta* for the the left ventricle, by the *pulmonary artery* for the right ventricle, by the *pulmonary veins* for the left atrium and by the superior and inferior *venae cavae* for the right atrium. Moreover, we have the *aortic valve* and *pulmonary valve*, which separate the circulatory system from the left ventricle and the right ventricle respectively.

The wall of the heart consists of three layers: the *endocardium* (inner layer), the *myocardium* (middle layer), which is the most thickest layer of the heart wall and which is the cardiac muscle responsible for heart pumping action, and the *epicardium* (external layer). In addition, there is the *pericardium*, the outermost membrane which surrounds and protects the heart.

Figure 1.3 gives a schematic representation of the components of the heart and the circulatory system.

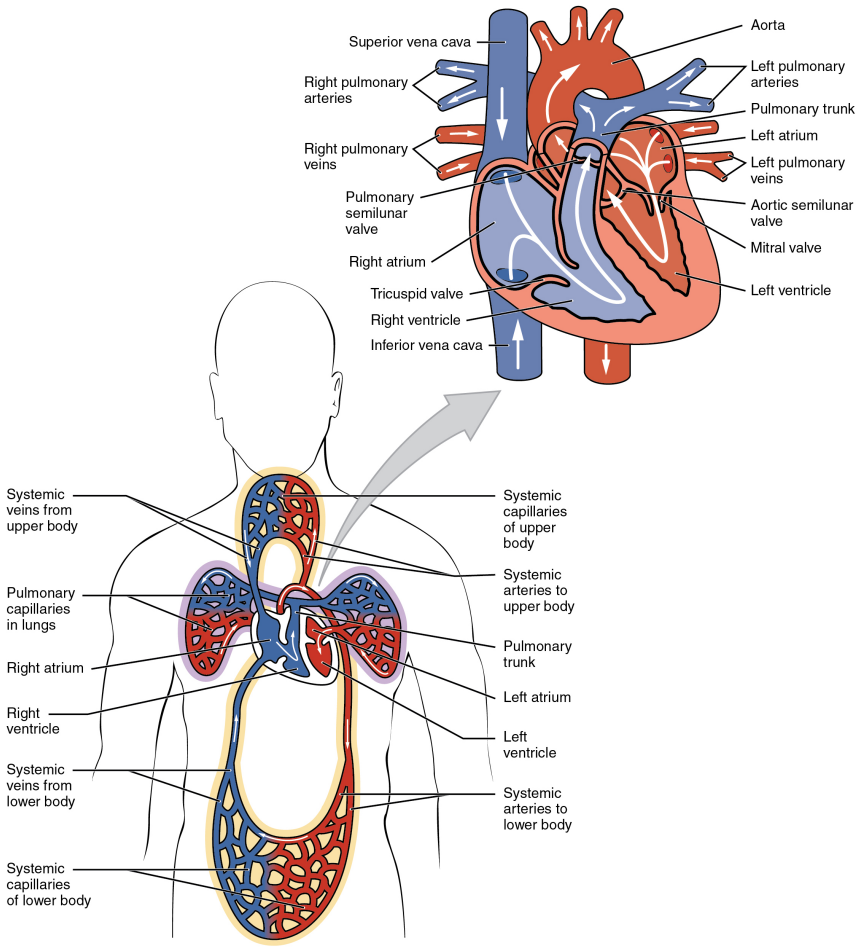

Figure 1.3: Schematic representation of the human heart and of the circulatoty system.

The period of time that begins with contraction of the atria and ends with ventricular relaxation is known as **cardiac cycle**. One cardiac cycle lasts about 0.8 seconds and it consists of two periods: **systole** is the period of contraction that the heart undergoes while it pumps blood into circulation, **diastole** instead is the period when the heart muscle is relaxed and the chambers fill with blood. In each cardiac cycle both atria and ventricles undergo systole and diastole.

We would like to give a description about the events that occur during a cardiac cicle, considering the left side of the heart. Recalling that blood flows according to pressure gradients, that is it moves from regions that are higher in pressure to regions that are lower in pressure, we can distinguish four different phases:

(1) *Ventricular filling.* At the beginning, both the atria and ventricles are relaxed (diastole). Blood flows into the left atrium from the pulmonary veins. Due to the continuos inflation of blood, when the pressure of the atrium exceeds the ventricular pressure, the mitral valve opens. In this way blood flows unimpeded from the atrium into the ventricle. Next up an active phase takes place, the so-called *atrial systole*, where the atrium contracts actively pumping extra blood in the ventricle.

(2) *Isovolumic contraction.* After atrial systole, the muscle in the ventricle contracts and

the pressure of the blood within the chamber rises, but it is not high enough to open the aortic valve. The increase in pressure quickly rises above that of the atria. This fact causes blood to flow back toward the atrium, closing the mitral valve. This initial phase of *ventricular systole* is known as *isovolumic contraction*, because during this time there is continuos and fast increase of ventricular pressure without any change of blood volume.

(3) *Ventricular ejection.* As soon as the ventricular pressure is greater than the aortic pressure (about 70 $mmHg$) the aortic valve opens and ejection begins. In addition to this, the ventricular pressure continues to increase, because the ventricular contraction carries on after the valve opens. The aortic pressure increases too due to the adaptation of the vessel wall. However, there is still a pressure difference that allows blood to accelerate. When the ventricle stops its active contraction, this pressure difference reduces and after a short period becomes zero. In this moment blood flow rate reaches its maximum. Then the pressure difference start to become negative, the blood decelarates but continues to enter the aorta. When the flow rate becomes negative the aortic valve closes and blood ejection stops.

(4) *Isovolumic relaxation.* The release of energy of the ventricle continues despite of the closure of the valve, even when the aortic valve closes. So there is no changes in ventricular volume, resulting in a fast decrease of the ventricular pressure.

The cardiac cycle could be well described by the Wiggers diagram (Figure 1.4) which shows a temporal relationship between left ventricular pressure, left ventricular volume, left atrial pressure and aortic pressure.

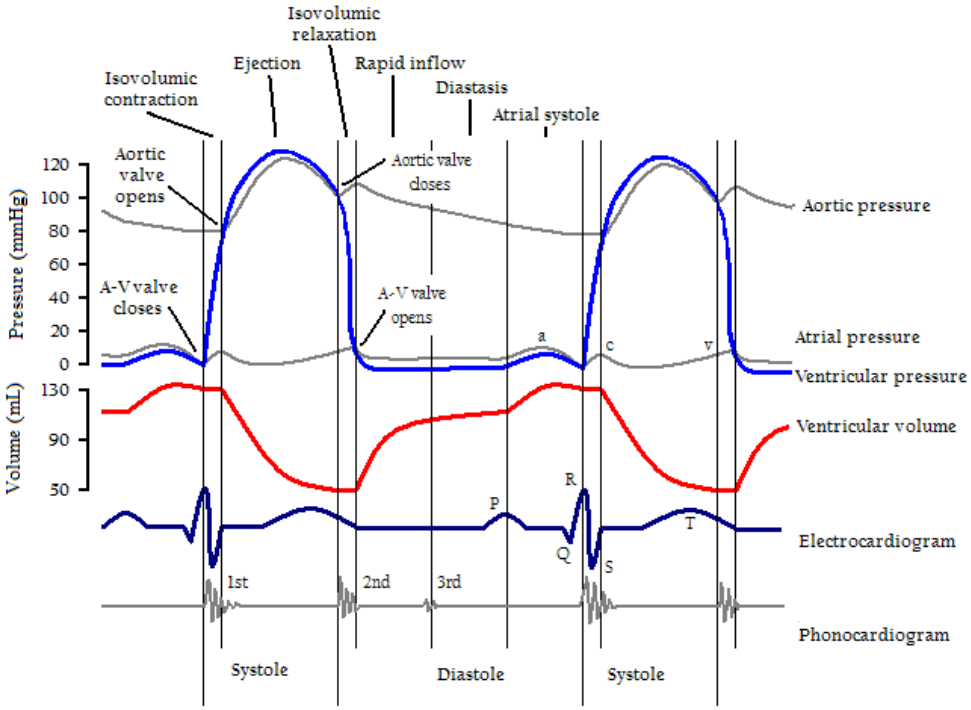

Figure 1.4: Wiggers diagram.

1.1.3 The blood vessels

Blood is carried through the human body via blood vessels. There are five types of blood vessels, which are **arteries**, **arterioles**, **capillaries**, **venules** and **veins**.

Arteries carry blood away from heart to other regions. They branch into ever-smaller vessels, the arterioles, which further branch into tiny capillaries where nutrients and wastes are exchanged. Then, groups of capillaries reunite to form small veins called venules. Then venules merge to form progressively larger blood vessels, the veins, which returns blood to the heart. Capillaries are the smallest blood vessels with a diameter of approximately $5\mu m$. In the capillaries takes place an important function of the circulation, that is the exchange of material between circulation and cells. In fact these microvessels are the sites of the transfer of oxygen and other nutrients from the bloodstream to other tissues in the body.

Altough different types of blood vessels differ structurally and functionally, they share the same general features. First of all, each type of blood vessel has a **lumen**, a hollow passageway through which blood flows. To maintain the pressure of blood moving through the system, in general, the lumen of arteries is smaller than that of veins. Moreover all blood vessels have the same wall's structure. It consists of three distinct tissue layers, called *tunics*. From the most interior layer to the outer there are: the **tunica intima**, which is in direct contact with blood and is made mainly of endothelial cells, the **tunica media**, a middle layer consisting of smooth muscle and elastic fiber and the **tunica adventitia**, the covering layer mainly made of connective tissue, see Figure 1.5.

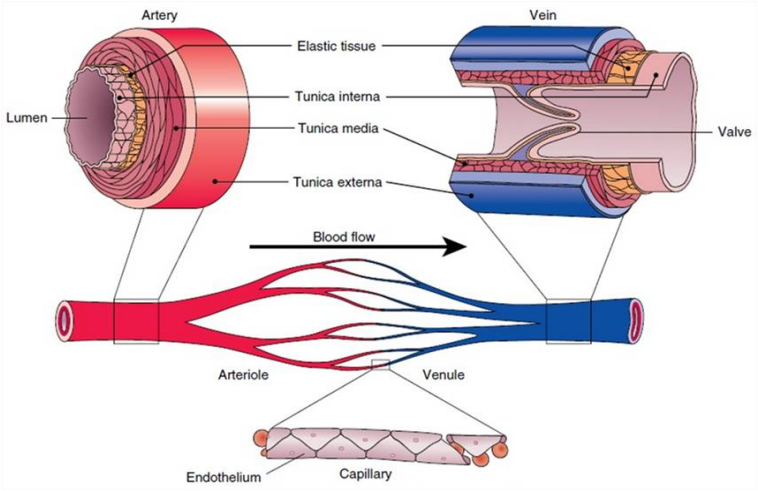

Figure 1.5: Structure of capillary, vein and artery.

1.2 The coronary circulation

Our field of study is on the coronary arteries. We know that the myocardium is a working muscle that needs a continuous supply of oxygen and nutrients to function efficiently. In fact it is the contraction of this muscle that pumps blood through the heart and into the major arteries. For this reason, the myocardium has its own network of blood vessels: the *coronary circulation*. This set of vessels provides to bring oxygen to the contracting cells and to remove waste products.

As we can see in Figure 1.6, the coronary arteries depart from the aorta and encircle

the heart. There are two main arteries which are the **right coronary artery** and the **left coronary artery**. The right coronary artery proceeds along the coronary sulcus and supplies blood to the right atrium. It divides into the *posterior interventricular artery* and other marginal branches. The left coronary artery distributes blood to the left side of the heart. It divides into the **left anterior descending** (LAD) **artery** and the **circumflex artery** (LCX). The LCX follows the coronary sulcus to the left, whereas the LAD follows the anterior interventricular sulcus around the pulmonary trunk. The LAD gives rise to numerous smaller branches that interconnect with other vessels forming *anastomosis*, which is a connection between two blood vessels that are normally diverging. This new structure allows blood to circulate to a region even if there may be a partial blockage in another branch [1].

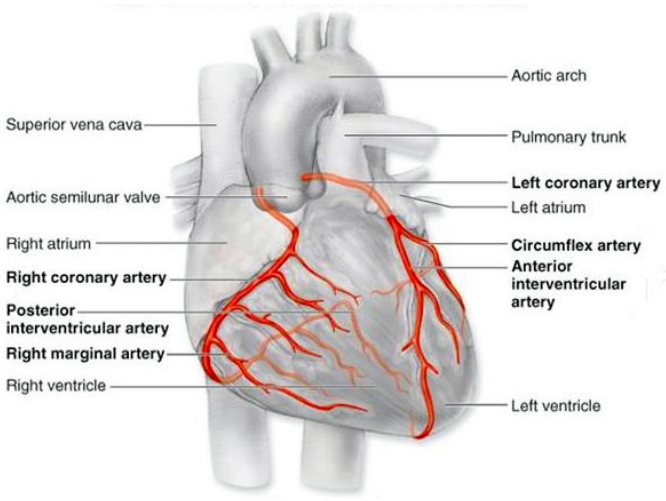

Figure 1.6: Coronary circulation.

We would like to remark that about two-thirds of the coronary arterial system is intramural, that is, inside the myocardium, and so, intramural vessels are compressed during systole. In particular, when coronary blood pressure is minimal, coronary artery flow stops briefly or even reverses and full flow is only restored during diastole. For this reason we find that about 80% of coronary blood flow occurs in diastole, contrary to what happens in other arteries where the peak is reached during systole.

1.3 Coronary artery disease

Coronary artery disease (CAD) is the number one cause of death in the world. CAD is due to changes in the coronary physiology, in fact it is caused by the formation of atherosclerotic plaques in the coronary vessel wall, due to the accumulation of lipids within the arterial intima. These plaques form a decrease in the vessel lumen which is called *stenosis* (Figure 1.7).

This pathology has two main consequences: the blood tends to descrease, resulting in a reduction of oxygen supply to the heart, and the pressure in the arteries gets higher. To face this new situation, the system reacts trying to dilate in order to assure the same amount of blood flowing before developing the stenosis. This is done by the so-called *microcirculation*, that is the vessels of the coronary tree with a diameter smaller than $0.5\,mm$. But this

mechanism of autoregolation is limited and it is possible that, at a certain point, the coronary flow is not sufficient anymore to irrorate the myocardial cells with blood. The result is an imbalance perfusion between supply and demand of oxygen and for this reason the myocardial cells die, leading to *myocardial ischemia*.

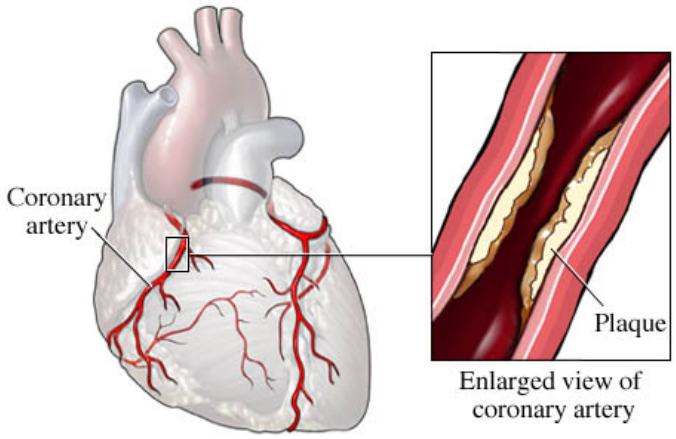

Figure 1.7: Detail of a coronary stenosis.

Coronary artery diseases can be seen as an "injury" of the inner layer of coronary artery. This damage may be caused by various factors. Some of these factors, including smoking, obesity, diabet and a sedentary lifestyle, are modificable, others not and in this case we refer to age, genetic factors [9] and personality. As for symptoms, we could have chest pain, usually refer to *angina* and also felt in the neck, arm or back, shortness of breath and heart attack.

Of sure, an healty lifestyle is a good way in order to try to prevent CAD.

1.4 Diagnosis

There are several different tools that aid in the treatment of coronary artery disease. The traditional procedures include coronary angiography, intravascular ultrasound (IVUS) and Magnetic Resonance Imaging (MRI). In the last thirty years another advanced tool was developed. We refer to a next-generation imaging technology called Optical Coherence Tomography (OCT).

Coronary angiography

Coronary angiography is a minimally invasive medical test that uses a special dye and x-rays to see how blood flows through coronaries. This test shows the extent and severity of any heart disease (it is possible to recognize occlusion, stenosis and thrombosis of coronary artery lumens) and can help doctors to figure out how well the heart is working.

The procedure is done using a catheter, a thin, flexible tube which reaches the desired artery from an access point, usually located in the arm or in the groin. The catheter is inserted using a sheath and a guide wire, a special guide which has a small sensor at its tip which measures blood pressure. Once the catheter is guided into the area being examined, the contrast material is injected through the tube and images are captured using x-rays (see Figure 1.8). Then, in order to perform the pressure wire test, an infusion of special drug (the *adenosine*) is given in order to increase blood flow and to ensure a minimal resistance by the

microcirculation. This is a very important factor involved in this procedure, we explain it better in the next subsection. The pressure across the artery is then recorded by positioning the pressure wire beyond the stenosis.

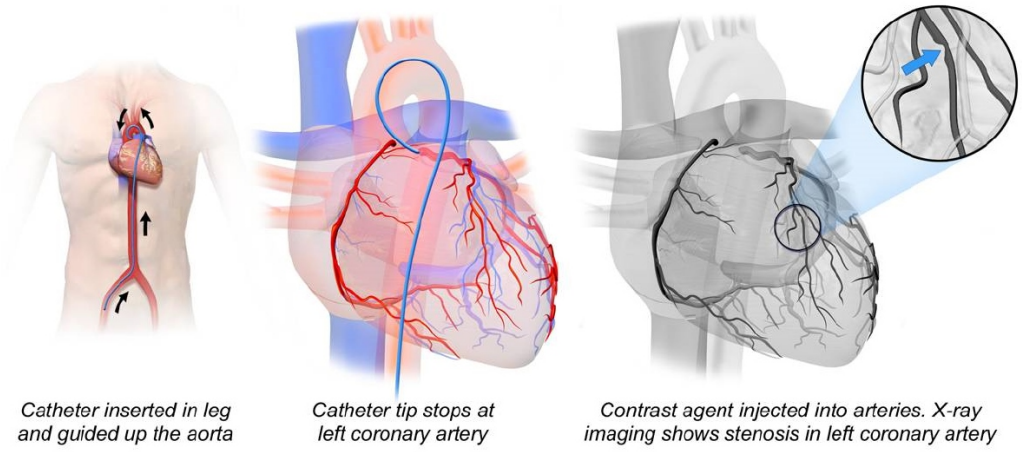

Figure 1.8: Coronary angiography.

From the information collected through this procedure, doctors determine which is the best treatment for the case analyzed. One possible treatment is the *coronary angioplasty*, a non surgical tecnique used to open clogged heart arteries, which involves the insertion and inflation of a tiny balloon-tipped catheter where the artery is clogged. This stent allows blood to flow more freely. In the most severe cases a surgical procedure is necessary, the *coronary bypass* surgery. It is a procedure that diverts flow of blood around a section of blocked artery creating a new pathway to the heart.

It is important to say that, in order to understand the severity of the case analysed, doctors base the decision for medical treating of a coronary stenosis on two important hemodynamic diagnostic indices: the fractional flow reserve (FFR) and the coronary flow reserve (CFR). We present these two important indices in the next subsections.

Optical Coherence Tomography (OCT)

Intracoronary Optical Coherence Tomography is a light-based imaging modality able to visualize with high resolution ($\sim 10\mu m$) the vascular morphology. It is a tecnique similar to Intravascular Ultrasound (IVUS), but it uses light rather than ultrasound and has 10-fold higher resolution than IVUS. The infrared light (wavelength of about 1300) is absorbed by blood cells, water, lipids and protein, and high-resolution in vivo images of coronary arteries are produced. In this way OCT can differentiate the internal and external elastic laminae, as well as distinguish the different layers of the vessel, a thing that was impossible to do with the low resolution of IVUS [6].

The clinical exam is done in an invasive way, by inserting a catheter. During the procedure, the OCT data are projected in real time on a screen. From these images it is possible to see the lumen profile, which is generated after automated lumen detenction in all OCT cross-sectional images. This view provides a lot of information such as minimal lumen diameter and also degree of area or diameter of a stenosis. These information are simoultaneously

projected on the screen, providing a fast assessment of the severity of luminal stenosis. Moreover, OCT information is also reconstructed in 3D and can be displayed in parallel to view the shape of a vessel. In Figure 1.9 we can see a typical OCT image.

OCT is a new important tecnique that can provide detailed information about the vessel that can not be obtained with other procedure and is still a field of research for better improvement.

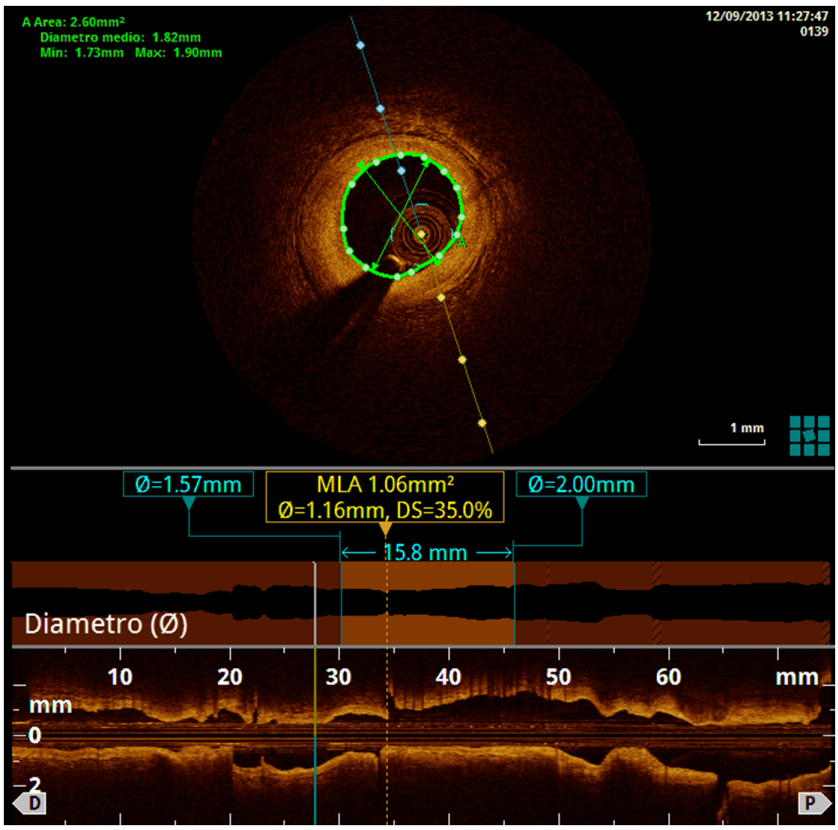

Figure 1.9: Typical OCT image provided by Doctor Roberto Bonmassari, "Santa Chiara Hospital, Trento".

1.4.1 The FFR - Fractional Flow Reserve

The Fractional Flow Reserve (FFR) is an index which provides a quantification of a stenosis severity. It is independent of hemodynamic loading conditions [12] (such as blood pressure and heart rate) and it is obtained by coronary pressure measurements during coronary catheterization.

FFR is defined as the ratio of maximum blood flow in a stenotic artery to normal maximum blood flow in the same artery, assuming that these measurements are obtained in the state of maximal hyperemia when the microvasculature resistance is minimal and constant. This is very important because the system must be studied at maximum vasodilation, corresponding to myocardial hyperemia when myocardial resistance is minimal (and therefore constant) and blood flow is proportional to driving pressure. If maximal vasodilation is not achieved, the pressure gradient across the lesion will be smaller and FFR will be overstimated. In order to reach this condition, a potent vasodilator, the *adenosine*, is administrated.

To sum up,

$$FFR = \frac{\text{Maximum myocardial flow in presence of a stenosis}}{\text{Normal maximum flow}} = \frac{Q_S^{max}}{Q_N^{max}}. \tag{1.1}$$

In other words FFR shows how far maximal myocardial flow is limited when a stenosis is present, representing that fraction of maximum flow which can still be maintained despite the presence of the stenosis. For example, an FFR of 0.60 means that, due to the presence of the stenosis, maximum achievable blood flow to the myocardium is only 60% of what it would be if the coronary artery was completely normal.

In particular, we can write

$$Q_N^{max} = \frac{P_a - P_v}{R} \tag{1.2}$$

and

$$Q_S^{max} = \frac{P_d - P_v}{R}, \tag{1.3}$$

where R is the myocardial resistance at maximum vasodilation, P_a is the mean aortic pressure, P_v the mean central venous pressure and P_d the hyperemic distal coronary pressure.

Now, because we are in condition of maximal hyperemia, the myocardial vascular bed is maximally vasodilated and its resistance is minimal and constant, we obtain

$$FFR = \frac{Q_S^{max}}{Q_N^{max}} = \frac{P_d - P_v}{P_a - P_v}. \tag{1.4}$$

Moreover, the central venous pressure P_v is generally closed to zero, so the equation simplified in

$$FFR = \frac{P_d}{P_a}. \tag{1.5}$$

The ratio of the two pressure can be easily measured by a pressure wire for the P_d and by a guiding catheter for the P_a [10].

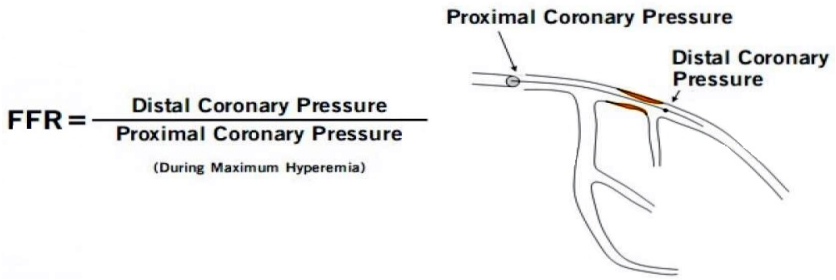

Figure 1.10: FFR measurement.

In a normal coronary artery there is no decrease in pressure, so the theoretical normal value of FFR is 1. In general, an FFR > 0.80 predicts non significant stenosis, whereas FFR < 0.75 indicates lesions and interventions are needed. FFR values between 0.75 and 0.80 are referred to as the FFR gray zone, an area which could affect decisions about clinical procedure because there is uncertainty regarding the actual degree of ischemia.

1.4.2 The CFR - Coronary Flow Reserve

The coronary circulation has an intrinsic mechanism of autoregulation, which can be describe as "the ability of an organ to maintain a constant blood flow despite changes in perfusion pressure". This is achieved by dilatation, mainly in the microvascular coronary arterial bed.

Coronary Flow Reserve (CFR) is an index which describes the myocardial blood supply, specifically the ability of the coronaries to increase blood flow when metabolic requirements demand it. It is defined as maximal hyperemic flow divided by resting flow

$$CFR = \frac{Q_h^S}{Q_{rest}^S}, \tag{1.6}$$

where Q_h^S is the hyperemic flow in presence of stenosis, while Q_{rest}^S is the basal stenotic flow. In other words CFR can be thought of as the capacity of the coronary circulation to dilate and increase flow following an increase in myocardial metabolic demand.

Even this index is measured in an invasive way in the catheterization laboratory and in patients with normal artery it usually exceeds the value of 3.0. It is important to say that, differently from the FFR, CFR depens on hemodynamic conditions, like blood pressure and heart rate, and for this reason it is not so used for medical predictions.

1.5 The use of computational methods

Computational models are models which try to understand and solve complex problem by means of computer simulations. They can be considered one of the best currently-available tools that allows researchers to make predictions of system's behaviour under different conditions, often for cases in which the analytical solutions are not available.

In this context, a primary role is played by computers. In fact, researchers always have to deal with a large number of equations that have to be constructed and solved and this is very impratical to do by hand. With the use of computers, specific codes could be implemented to approximate and solve these equations which often evolve in time, thus requiring the solution at several discrete time steps.

The first thing to do for the construction of a computational model is the analysis of the physical problem, that is the formulation of a set of ideas about the basic operations of the system of interest and the possible assumptions that can simplify the model. The second step involves translating the ideas into mathematical form. Each kind of interaction must be expressed as a mathematical relationship and the result is a mathematical model which includes all the variables useful for the investigations. Since often the analytical solution of the mathematical equations is not known, the third step involves the development of appropriate numerical methods in order to find an approximate solution of the problem. The final step is converting the mathematical relationships into computer code. This process involves the choice of suitable computer framework and algorithms for the implementation.

Computational methods and tecniques came to play an increasing central role in various field such as engineering, medical research and biology. In particular we are interested in the mathematical approach for the modeling of cardiovascular system. In this field mathematical models and numerical simulations are very useful for understanding the mechanisms influencing cardiovascular system's physiological and pathological processes. This modeling research can be used by doctors for decisions about therapy selection and intervention planning, collecting informations without the necessity of invasive procedures. We provide a panoramic

view of the state-of-art on this argument in Section 1.6.

However, mathematical modeling presents challenging problems due to the complexity of the cardiovascular system. A lot of assumptions should be considered and each of these assumptions introduce a possible reason that the model will not match the physical system it tries to mimic.

Computational science is at the heart of modern material research and is a field which holds much future potential.

1.6 State of the art of computational studies on coronaries

One of the main interests in cardiovascular mathematics is modeling blood flow. Reaserchers can in fact obtain useful data in a non-invasive way by constructing blood vessels geometries and by solving blood flow simulations in them. Accurate modeling of the circulatory system is still a challenging objective, however, in the last few years big steps have been taken in this direction, see [15], [19], [24], [50] and [51].

There are many technical difficulties in simulating blood flow. The first one is the reconstruction of the model from clinical radiological images which requires advanced mathematical and numerical tools. In fact, sometimes, if the resolution of the imaging device is too small, it may be difficult to identify some components of the model or it may be hard to detect the vessel wall. In a second step, a lot of attention may be put in the creation of the mesh for the geometrical model. Mesh generation is the starting point of any finite element method and this task must be carefully done as the mesh is responsible for the accuracy of the solution. It means that the characteritics of the mesh, in terms of shape, size and density of its elements, must be adeguate in order to capture the hemodynamics of the problem as accurately as possible. Finally, the prescription of suitable and physically consistent boundary conditions is a crucial issue. We have to consider that the computational domains always results from an artificial truncation and it is only a part of the entire cardiovascular system. In this way, suitable data (such as fluid velocity and pressure) must be provided at those numerical boundaries that does not correspond to physical boundaries. This could be done for example by using measures or by coupling the 3D system with geometrically reduced models.

The literature on the mathematical and numerical modeling of the cardiovascular system is huge, in fact this is a research topic that has attracted remarkable interest from the mathematical communities.

In primis, over the last years much effort has been made to reconstruct image-based models of coronary arteries to be used in computational studies, see [36] and [37]. In [34] the authors propose a semi-automatic method to reconstruct the actual configuration of coronary arteries after stent implantation from OCT images.

In the context of fluid dynamics instead, we cite [15], [19], [23], [39], and [50] that review the methods and challenges associated with the adoption of computational fluid dynamics (CFD) modeling within cardiovascular medicine. Furthermore, the authors of [35] suggest a 3D fluid-structure interaction model based on patient specific data in order to predict coronary plaque progression considering both morphological and biomedical factors, whereas in [38] they explore the tecniques for simulating intracoronary flows on a real coronary geometry. In [40] instead, the study highlights the value of numerical simulations applied in 3D models for assessing hemodynamic factors such as coronary artery pressure.

Another field of reasearch, in the context of fluid dynamics and blood flow, is about the diagnostic index FFR for coronary stenosis. As we have already said in Chapter 1, image-

based non-invasive fractional flow reserve (FFR) is an emergent approach to determine the functional relevance of coronary stenosis. The literature on this argument is huge. Some articles report the development of computational methods that accurately predict myocardial fractional flow reserve from angiographic images in patients with coronary artery disease, see [42], [43] and [44]. Moreover, in [41] the authors try to determine the feasibility of using a method based on coronary tomography angiography and reduced-order models for the evaluation of coronary stenosis.

Other studies aim to investigate the influence of the pressure guide wire on the velocity and pressure values, factors which modify the FFR value. On this argument we can find some studies of the effect of the pressure guide wire in the work provided by Stella [21] and Zerbini [22], but which do not consider a real geometry.

In addition to this, another field of research is about investigating the effects of medical operations, such as coronary stenting and bypasses. For example, the authors of [47] make a study to determine the effect of coronary stent on in-hospital mortality, whereas Guerciotti et al. [18] try to find a possible relationship between coronary stenosis degree and the risk of graft failure.

1.7 The aim of our work

In the previous sections we have introduced the FFR index and we have highlighted its importance in clinical decisions. We have said that this index is obtained in an invasive way through pressure measurements with a guide wire. Since from the value of this index can depend patients' life, it is important to understand the possible factors that can influence its measure.

For example, in Figure 1.11 we report a graph that shows the correlation between some FFR measurements and the stenosis diameter. These data are collects from about 200 patients [1]. The dispersion and variability of the data suggest that there are several variables that can influence measurements such as the shape and position of the stenosis along the stenotic branch, the presence of the guide wire and even the position where the pressures' measure is taken.

In particular, cardiologists think that the influence of the pressure guide wire can be negligible due to the small dimensions of the instrument they use. We would like to study the reliability of this assumption developing a computational study to investigate if and how much a pressure guide wire influences the pressure of the blood on a real stenotic coronary artery. Our computer simulations try to simulate the guide wire effect in pressure measurements, making a comparison between results obtained with and without the presence of the guide.

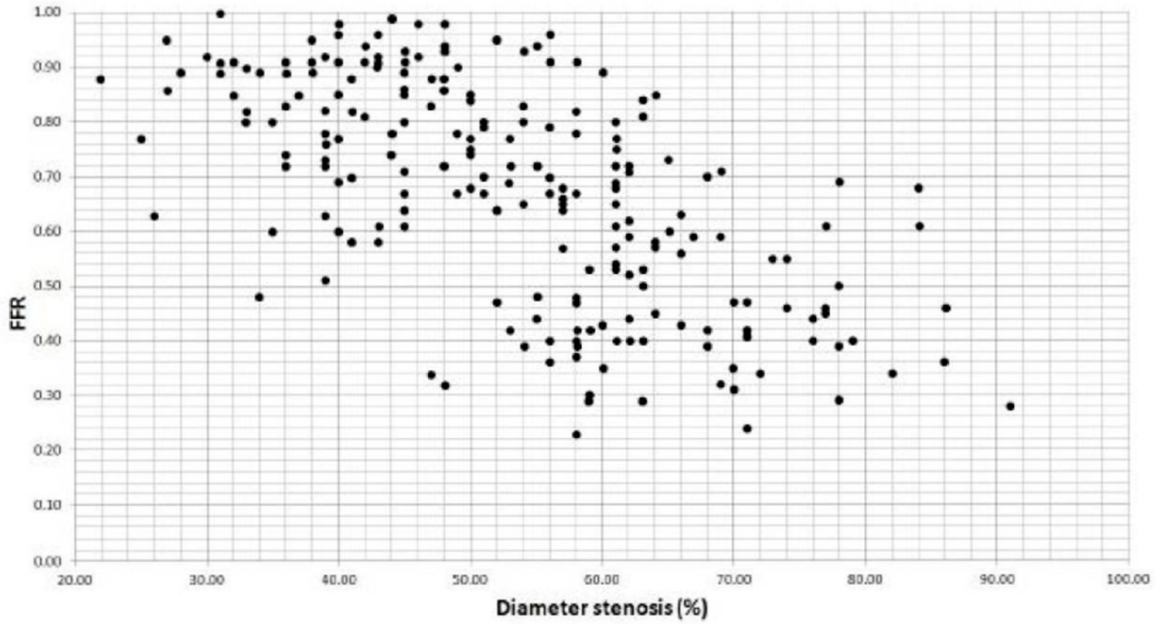

Figure 1.11: Real FFR values as a function of the degree of stenosis [1].

Of course we make a lot of assumptions to simplify the model and there are also a lot of limitations that will be discussed later on, but our results can be promising for future researches in FFR accuracy.

Chapter 2

Mathematical and numerical modeling

Mathematical and numerical modeling of the cardiovascular system is a research topic that has attracted interest from the mathematical communities over the last years. The driving motivation is the increasing impact of cardiovascular diseases in our lives which are the major cause of death worldwide. In this chapter we will focus our attention on the mathematical modeling of blood flow and its corresponding numerical approximation.

2.1 Mathematical aspects

2.1.1 Models for blood

In this section we consider the main physical features of the blood as a fluid. We are interesting in the so called *constitutive relations* (also known as *rheological relations*), which describe the response of the material to external forces and assess the dependence of the stress tensor from the strain rate tensor.

According to the different form of the rheological relation we can distinguish different kinds of fluid [23], in particular:

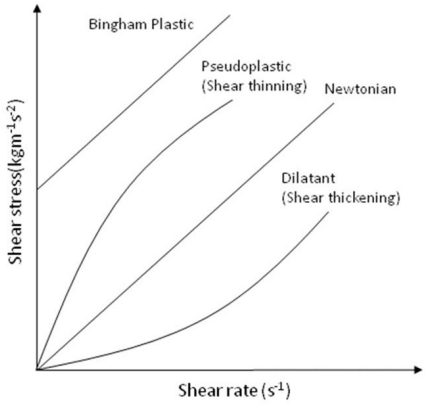

Figure 2.1: Different fluid rheological behaviours.

- *Newtonian fluid*: the shear stress is related linearly to the shear rate.
- *Dilatant fluid*: the apparent viscosity (i.e. the ratio between the shear stress and the strain rate) increases when the strain rate increases. The strain rate-stress curve is convex.
- *Pseudoplastic fluid*: the apparent viscosity decreases as the strain rate increases. The strain rate-stress curve is concave.
- *Bingham plastic*: the relationship between stress and strain rate is linear. Despite this fact there is a threshold value of the stress beyond which there is deformation.

As we seen in Chapter 1, blood is a heterogeneous mixture of solid corpuscles (red blood cells, white blood cells and platelets) suspended in a liquid plasma which is a solution of proteins, organic molecules and minerals. The properties of these components and their interaction with each other determines the rheological characteristics of blood. While the plasma is essentially a Newtonian fluid, the blood as a whole behaves as a non-Newtonian fluid. Most non-Newtonian effects originate from the red blood cells due to their high concentration and their ability to aggregate forming three-dimensional structures at low deformation rates, which are known as "*rouleaux*".

Nevertheless, in order to simplify the flow models and their computational implementation, blood is generally assumed Newtonian and its non Newtonian effects are ignored (see, for example, [26]). This approximation is well accepted for medium and large vessels, for small vessels such as capillaries instead, cells dimensions could not be ignored and so blood should be considered as non Newtonian (see [18], [19] and [27]). In literature we can find several studies which try to compare Newtonian and non-Newtonian modeling research. For example, Gijsen et al. [25] showed that applying non-Newtonian fluid flow in arteries with bifurcations greatly affects the flow features compared to Newtonian fluid flow.

In our work we have to make some assumptions in order to simplify the model and the formulation of the equations governing the blood flow. In particular:

- we are going to consider blood as a Newtonian fluid, aware that this is not entirely correct from a physical point of view;
- we consider blood an *incompressible*, that is the density ρ is constant, and an *homogeneous* fluid, despite the presence of its solid components whose dimension could be negligible.

We now introduce the dimensionless parameter called *Reynolds number*, defined in this way [8]:

$$Re = \frac{\text{inertial forces}}{\text{viscous forces}} = \frac{\rho U d}{\mu} = \frac{U d}{\nu},$$

where d is a characteristic dimension of the vessel (such as the diameter), U is the characteristic velocity of the fluid, μ is the viscosity and ρ the density of the fluid. Moreover, ν is the kinematic viscosity of the fluid (defined as μ/ρ). The Reynolds number helps to predict flow patterns in different fluid flow situations. In fact when Re is less than 2300 the flow is everywhere laminar, but when Re is greater than 2500 the flow shows continuous turbulence. In the region between 2300 and 2500, transition occurs and it is possible to observe intermittent turbulence [8].

We add other two important assumptions:

- for semplicity, in the mathematical modeling, we will constantly assume a laminar flow. The value of the Reynolds number in the coronaries is about 400, so we are in this condition. Despite this fact, we are aware that we are dealing with stenotic coronaries and so it is possible that flow undergoes transition to turbolence;
- the wall of the coronaries will be considered rigid and not elastic. This is a significant approximation because it is known that the vessels' walls in our body are elastic, but this choice is justified by noticing that the coronary vessel wall displacements are quite small.

Now we are ready to write the mathematical formulation of our work, i.e. the Navier-Stokes equations for an incompressible, homogeneous and Newtonian fluid.

2.1.2 Derivation of the Navier-Stokes equations

The Navier-Stokes equations are at the heart of fluid flow modeling. These equations govern the motion of fluids and their resolution for a particular set of boundary conditions can be used to predict the fluid velocity and its pressure in a given geometry.

In order to write the Navier-Stokes equations with the hypothesis of the previous section, it is necessary to introduce the continuity and momentum equations, which put together composed the equations we are waiting for. We are going to describe the procedure, mainly following the approach we find in [24] and for more details we refer the reader to this article.

First of all we recall **the Reynolds transport theorem**, that will be often used in our computations. The Reynolds transport theorem is a three-dimensional generalization of the Liebniz integral rule and it is used in the formulation of the basic conservation laws of continuum mechanics, particularly fluid dynamics. In fact, it is often more convenient to work with a control volume, as it is difficult to identify and follow a system of fluid particles. Thus, there is the need to relate the system equations and the corresponding control volume equations and the link between the two is given by the Reynolds transport theorem.

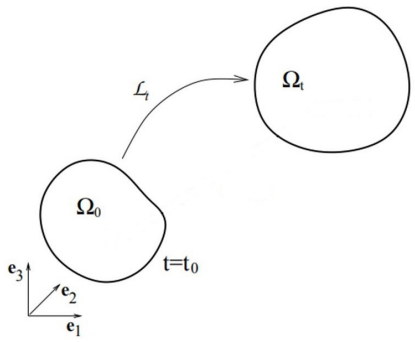

Figure 2.2: Domains at different times linked by the Lagrangian map $\mathcal{L}$ [24].

Since now on we will use this notation (see Figure 2.2): Ω_t is the domain occupied by the fluid at time t and $V_t \subset \Omega_t$ is the material volume at time t, that is $V_t = \mathcal{L}_t(V_0)$ where $V_0 \subset \Omega_0$ and $\mathcal{L}_t$ is a Lagrangian map. Σ_t is the surface of V_t.

The Reynolds theorem states that for any differentiable function $\mathbf{f}$, the following relation holds true

$$\frac{d}{dt}\int_{V_t}\mathbf{f}\,dV = \int_{V_t}\left(\frac{D\mathbf{f}}{Dt} + \mathbf{f}\,div\mathbf{u}\right)dV = \int_{V_t}\left(\frac{\partial\mathbf{f}}{\partial t} + div\,(\mathbf{fu})\right)dV, \tag{2.1}$$

where $\mathbf{u}$ is the velocity of the area element and

$$\frac{D\mathbf{f}}{Dt} = \frac{\partial\mathbf{f}}{\partial t} + \mathbf{u}\cdot\nabla\mathbf{f}$$

is the material (or lagrangian) derivative.

Equivalently, by using the divergence theorem, equation (2.1) becomes

$$\frac{d}{dt}\int_{V_t}\mathbf{f}\,dV = \int_{V_t}\frac{\partial\mathbf{f}}{\partial t}\,dV + \int_{\Sigma_t}\mathbf{f}\,(\mathbf{u}\cdot\mathbf{n})\,d\Sigma, \tag{2.2}$$

where $\mathbf{n}$ is the outward-pointing unit normal.

The continuity equation

The continuity equation is the principle of mass conservation. Conservation of mass states that matter can neither be created or destroyed, so any increase or decrease in mass must be due to the flux of matter through the surface bounding the volume V that moves with the fluid. Mathematically:

$$\frac{dm}{dt} = \frac{d}{dt}\int_{V_t}\rho\,dV = 0, \tag{2.3}$$

where m is the mass of the fluid in the volume V and ρ its density.

Applying the Reynolds transport theorem

$$\frac{d}{dt}\int_{V_t}\rho\,dV = \int_{V_t}\left(\frac{\partial\rho}{\partial t} + (div\,(\rho\mathbf{u}))\right)dV, \tag{2.4}$$

equation (2.3) becomes

$$\int_{V_t}\left(\frac{\partial\rho}{\partial t} + (div\,(\rho\mathbf{u}))\right)dV = 0. \tag{2.5}$$

Assuming that the terms under the integral are continuous and since the equation (2.5) should be true for any arbitrary volume of integration, the integrand must be zero. So the continuity equation results

$$\frac{\partial\rho}{\partial t} + (div\,(\rho\mathbf{u})) = 0. \tag{2.6}$$

Recalling that we are considering an incompressible fluid, the density does not vary (it remains constant) and equation (2.6) becomes

$$div\,\mathbf{u} = 0. \tag{2.7}$$

The momentum equation

The momentum equation relates the sum of the forces acting on an element of fluid to its rate of change of momentum. One will probably recognise the equation $\mathbf{F} = m\mathbf{a}$, conservation of momentum is actually an extension of the Newton's second law to continuous medium. This principle can be riformulated as follows:

"The rate of change of momentum of a body is equal to the resultant force acting on the body and takes place in the direction of the force".

We are going to use this notation:

- $\mathbf{Q}$ is the momentum, defined as $\mathbf{Q} = \int_{V_t} \rho\,\mathbf{u}\,dV$;
- $\mathbf{F}_V$ is the sum of the external forces $\mathbf{f}_V$ applied on volume V, $\mathbf{F}_V = \int_{V_t} \rho\,\mathbf{f}_V\,dV$;
- $\mathbf{F}_\Sigma$ is the sum of the surface forces $\mathbf{f}_\Sigma$ acting on surface Σ, $\mathbf{F}_\Sigma = \int_{\Sigma_t} \mathbf{f}_\Sigma\,d\Sigma$.

So, in mathematical form, the conservation of momentum reads as follows:

$$\frac{d\mathbf{Q}}{dt} = \mathbf{F}_V + \mathbf{F}_\Sigma. \tag{2.8}$$

In words, we can say that the time variation of momentum of a system coincides with the resultant of the sum of volume and surface forces to the system.

In integral form we have

$$\frac{d}{dt}\int_{V_t} \rho\,\mathbf{u}\,dV = \int_{V_t} \rho\,\mathbf{f}_V\,dV + \int_{\Sigma_t} \mathbf{f}_\Sigma\,d\Sigma. \tag{2.9}$$

We assume now that the surface forces $\mathbf{f}_\Sigma$ may be represented through a vector field

$$t^e : I \times \Gamma_t^n \to \mathbb{R}^3$$

called *applied stresses*, where $I = (t_0, t_1)$ is a time interval and $\Gamma_t^n \subset \partial\Omega_t$ is a measurable subset of the domain boundary.

Principle 2.1 (Cauchy principle) *There exists a vector field* $\boldsymbol{t}$*, called Cauchy stress*

$$\boldsymbol{t} : I \times \Omega_t \times \boldsymbol{S}^1 \to \mathbb{R}^3, \tag{2.10}$$

with

$$\boldsymbol{S}^1 = \{\boldsymbol{n} \in \mathbb{R}^3 : |\boldsymbol{n}| = 1\},$$

such that its integral on the surface of any domain $V_t \subset \Omega_t$ *given by*

$$\int_{\Sigma_t} \boldsymbol{t}(t, \boldsymbol{x}, \boldsymbol{n})\,d\Sigma \tag{2.11}$$

is equivalent to the resultant of the continuity forces acting on V_t*. In (2.11),* $\boldsymbol{n}$ *is the outward normal of* Σ_t*. Moreover, we have that*

$$\boldsymbol{t} = \boldsymbol{t}^e \qquad on \quad \partial V_t \cap \Gamma_t^n. \tag{2.12}$$

In this way, formula (2.9) will be

$$\frac{d}{dt}\int_{V_t} \rho(t,\mathbf{x})\,\mathbf{u}(t,\mathbf{x})\,dV = \int_{V_t} \rho(t,\mathbf{x})\,\mathbf{f}_V(t,\mathbf{x})\,dV + \int_{\Sigma_t} \mathbf{t}\,(t,\mathbf{x},\mathbf{n})\,d\Sigma, \tag{2.13}$$

where $\mathbf{n}$ is the outward normal to $d\Sigma$.

Now, using the Cauchy stress tensor theorem (see [24] for more details), we can relate the

continuity forces to tensor field. This theorem states that under some appropriate assumptions, there exists a continuously differentiable symmetric tensor field, called *Cauchy stress tensor*

$$\mathbf{T} : I \times \bar{\Omega}_t \to \mathbb{R}^{3\times 3},$$

such that

$$\mathbf{t}(t, \mathbf{x}, \mathbf{n}) = \mathbf{T}(t, \mathbf{x}) \cdot \mathbf{n} \qquad \forall t \in I, \quad \forall \mathbf{x} \in \Omega_t, \quad \forall \mathbf{n} \in \mathbf{S}^1. \tag{2.14}$$

In this way we have

$$\int_{\Sigma_t} \mathbf{t}\, d\Sigma = \int_{\Sigma_t} \mathbf{T} \cdot \mathbf{n}\, d\Sigma \tag{2.15}$$

and the princicle of momentum (2.13) becomes

$$\frac{d}{dt} \int_{V_t} \rho\, \mathbf{u}\, dV = \int_{V_t} \rho\, \mathbf{f}_V\, dV + \int_{\Sigma_t} \mathbf{T} \cdot \mathbf{n}\, d\Sigma. \tag{2.16}$$

Applying Reynolds transport theorem to the left hand side of (2.16), recalling that in our case ρ is constant and $div\, \mathbf{u} = 0$, we get

$$\frac{d}{dt} \int_{V_t} \rho\, \mathbf{u}\, dV = \int_{V_t} \left(\frac{D(\rho \mathbf{u})}{Dt} + \rho\, \mathbf{u}\, div \mathbf{u} \right) dV = \int_{V_t} \rho \frac{D\mathbf{u}}{Dt}\, dV. \tag{2.17}$$

In this way, formula (2.16) results

$$\int_{V_t} \rho \frac{D\mathbf{u}}{Dt}\, dV = \int_{V_t} \rho\, \mathbf{f}_V\, dV + \int_{\Sigma_t} \mathbf{T} \cdot \mathbf{n}\, d\Sigma. \tag{2.18}$$

Now, by using the divergence theorem and assuming that $div\, \mathbf{T}$ is integrable, we obtain

$$\int_{V_t} \left(\rho \frac{D\mathbf{u}}{Dt} - \rho\, \mathbf{f}_V - div\, \mathbf{T} \right) dV = 0. \tag{2.19}$$

Recalling that V_t is an arbitrary volume, we finally get the following differential equation

$$\rho \frac{D\mathbf{u}}{Dt} - div\, \mathbf{T} = \rho\, \mathbf{f}_V. \tag{2.20}$$

Cosidering the following relation

$$\frac{D\mathbf{u}}{Dt} = \frac{\partial \mathbf{u}}{\partial t} + (\mathbf{u} \cdot \nabla)\mathbf{u} \tag{2.21}$$

we get

$$\rho \frac{\partial \mathbf{u}}{\partial t} + \rho\, (\mathbf{u} \cdot \nabla)\mathbf{u} - div\, \mathbf{T} = \rho\, \mathbf{f}, \tag{2.22}$$

where the non linear term $\rho\, (\mathbf{u} \cdot \nabla)\mathbf{u}$ is called *the convective term* and, for sake of simplicity, we omitt the subscript V for the volume forces.

The last step to obtain our momentum equation is find a relation between the Cauchy stress tensor and the velocity field making use of the *rheological relation*. Since we considered the fluid as Newtonian, the Cauchy stress tensor can be written as a linear function of the velocity derivaties

$$\mathbf{T} = -P\mathbf{I} + \mu\, (\nabla \mathbf{u} + \nabla \mathbf{u}^T), \tag{2.23}$$

where P is a scalar function called *pressure*, I is the identity matrix and μ is the *dynamic viscosity* of the fluid.

Introducing the *strain rate* tensor of this form

$$\mathbf{D}(\mathbf{u}) = \frac{(\nabla\mathbf{u} + \nabla\mathbf{u}^T)}{2} \tag{2.24}$$

we obtain

$$\mathbf{T} = -P\,\mathbf{I} + 2\mu\,\mathbf{D}(\mathbf{u}), \tag{2.25}$$

where the term $2\mu\,\mathbf{D}(\mathbf{u})$ is the *viscous stress* component of the stress tensor.

Now, with some mathematical steps,

$$div\,\mathbf{T} = -div\,(P\,\mathbf{I}) + 2\,div\,(\mu\,\mathbf{D}(\mathbf{u})) \tag{2.26}$$

but, recalling that P is a scalar and $\mathbf{I}$ is a vector field,

$$div\,(P\,\mathbf{I}) = \nabla P\,\mathbf{I} + P\,div\,\mathbf{I} = \nabla P \tag{2.27}$$

and so we obtain

$$div\,\mathbf{T} = -\nabla\,P + 2\,div\,(\mu\,\mathbf{D}(\mathbf{u})). \tag{2.28}$$

At the end, substituting in (2.22) we obtain

$$\rho\,\frac{\partial\mathbf{u}}{\partial t} + \rho\,(\mathbf{u}\cdot\nabla)\mathbf{u} + \nabla\,P - 2\,div\,(\mu\,\mathbf{D}(\mathbf{u})) = \rho\,\mathbf{f}. \tag{2.29}$$

Since ρ is constant we can divide everything by ρ. In addition to this, by introducing $\nu = \mu/\rho$ the *kinematic viscosity* and $p = P/\rho$ a scaled pressure, we obtain

$$\frac{\partial\mathbf{u}}{\partial t} + (\mathbf{u}\cdot\nabla)\mathbf{u} + \nabla\,p - 2\,div\,(\nu\,\mathbf{D}(\mathbf{u})) = \mathbf{f}. \tag{2.30}$$

The last thing we can do is observe that

$$div\,(\nu\,\mathbf{D}(\mathbf{u})) = \frac{\nu}{2}\,(div\nabla\mathbf{u} + div\nabla\mathbf{u}^T) = \frac{\nu}{2}\,(div\nabla\mathbf{u} + \nabla(div\mathbf{u})) = \frac{\nu}{2}\,div\nabla\mathbf{u} = \frac{\nu}{2}\Delta\mathbf{u}. \tag{2.31}$$

Finally, the final equation of the conservation of momentum reads:

$$\frac{\partial\mathbf{u}}{\partial t} + (\mathbf{u}\cdot\nabla)\mathbf{u} + \nabla\,p - \nu\,\Delta\mathbf{u} = \mathbf{f}. \tag{2.32}$$

2.1.3 The Navier-Stokes equation

In the previous section we explain how to get the continuity and momentum equations in details. These two equations together compose the famous Navier-Stokes equations and they are valid on any fixed spatial domain Ω which is for all times of interest inside the portion of space filled by the fluid, that is $\Omega \subset \Omega_t$.

The Navier-Stokes equations for an incompressible fluid with constant viscosity μ in a domain $\Omega \in \mathbb{R}^d$ (with $d = 3$ in our case) read as follows:

$$\begin{cases} \dfrac{\partial\mathbf{u}}{\partial t} - \nu\Delta\mathbf{u} + (\mathbf{u}\cdot\nabla)\mathbf{u} + \nabla p = \mathbf{0}, & \text{for} \quad \mathbf{x} \in \Omega, t > 0, \\ div\,\mathbf{u} = 0, & \text{for} \quad \mathbf{x} \in \Omega, t > 0, \end{cases} \tag{2.33}$$

where $\mathbf{u} = \mathbf{u}(\mathbf{x}, t)$ is the unknown fluid velocity, p the unknown pressure, ρ the density, $\nu = \mu/\rho$ the kinematic viscosity and μ the dynamic viscosity. We assume that $\mathbf{f} = 0$ because the gravity is negligible in the context of coronary arteries.

We would like that if all the data are smooth enough, then the solution is continuous together with its derivatives and does not develop singularities in time. In this case we say that the problem is well posed.

In order to ensure the well posedness of problem (2.33), it is necessary to assign an initial condition and properly boundary conditions:

$$\mathbf{u}(\mathbf{x}, 0) = \mathbf{u}_0(\mathbf{x}) \qquad \forall \mathbf{x} \in \Omega, \tag{2.34}$$

$$\begin{cases} \mathbf{u}(\mathbf{x}, t) = \boldsymbol{\varphi}(\mathbf{x}) & \forall \mathbf{x} \in \Gamma_D, \\ (\nu \dfrac{\partial \mathbf{u}}{\partial \mathbf{n}} - p\,\mathbf{n})(\mathbf{x}, t) = \boldsymbol{\psi}(\mathbf{x}, t) & \forall \mathbf{x} \in \Gamma_N, \end{cases} \tag{2.35}$$

where

- $\mathbf{u}_0(\mathbf{x})$, $\boldsymbol{\varphi}(\mathbf{x}, t)$, $\boldsymbol{\psi}(\mathbf{x}, t)$ are prescribed functions;
- Γ_D and Γ_N are partition of the boundary $\partial\Omega$ of Ω such that their union is the boundary of Ω and their intersection is empty;
- $\mathbf{n}$ is normal vector outgoing to Ω boundary.

In the two dimensional case, Navier-Stokes equations of this type yield well-posed problems in the sense that the solution of the problem exists, is unique and depends with continuity from the data. The situation is quite different in the 3D case, where existence and uniqueness of classical solution have been proven only locally in time. For this reason it is necessary to introduce the *weak formulation* of the Navier-Stokes equations which guarantee global results in time. In fact, the weak formulation allows us to switch from a differential problem of the second order to an integral problem of the first order, reducing, in this way, the order of derivation required to the unknowns. Moreover, the weak formulation is the necessary step towards Finite Element approximation [5].

2.1.4 The weak formulation

In general, the procedure to obtain the weak formulation of a differential problem is based on multipling the equation considered by a test function that belongs to an appropriate space and then integrate all over the domain. So we proceed in this way to obtain the weak formulation of the Navier-Stokes equations (2.33).

Firstly we multiply the first equation of (2.33) by a test function $\mathbf{v}$ belonging to a suitable space V and integrate it on the domain Ω

$$\int_\Omega \frac{\partial \mathbf{u}}{\partial t} \cdot \mathbf{v}\, d\Omega - \int_\Omega \nu\, \Delta \mathbf{u} \cdot \mathbf{v}\, d\Omega + \int_\Omega [(\mathbf{u} \cdot \nabla)\, \mathbf{u}] \cdot \mathbf{v}\, d\Omega + \int_\Omega \nabla p \cdot \mathbf{v}\, d\Omega = \mathbf{0}. \tag{2.36}$$

Now, recalling that, given two tensor A and B, their product is

$$A : B = \sum_{i,j=1}^{3} A_{ij} B_{ij} \tag{2.37}$$

and by applying the Green formulas, we obtain the following relations

$$-\int_\Omega \nu\,\Delta\mathbf{u}\cdot\mathbf{v}\,d\Omega = \int_\Omega \nu\,\nabla\mathbf{u}:\nabla\mathbf{v}\,d\Omega - \int_{\partial\Omega}\nu\,\frac{\partial\mathbf{u}}{\partial\mathbf{n}}\cdot\mathbf{v}\,d\gamma, \tag{2.38}$$

$$\int_\Omega \nabla p\cdot\mathbf{v}\,d\Omega = -\int_\Omega p\,div\mathbf{v}\,d\Omega + \int_{\partial\Omega} p\,\mathbf{v}\cdot\mathbf{n}\,d\gamma. \tag{2.39}$$

Inserting them in (2.36) we obtain

$$\int_\Omega \frac{\partial\mathbf{u}}{\partial t}\cdot\mathbf{v}\,d\Omega + \int_\Omega \nu\nabla\mathbf{u}:\nabla\mathbf{v}\,d\Omega + \int_\Omega[(\mathbf{u}\cdot\nabla)\mathbf{u}]\cdot\mathbf{v}\,d\Omega - \int_\Omega p\,div\mathbf{v}\,d\Omega = \int_{\partial\Omega}\left(\nu\frac{\partial\mathbf{u}}{\partial\mathbf{n}} - p\,\mathbf{n}\right)\cdot\mathbf{v}\,d\gamma \qquad \forall\,\mathbf{v}\in V. \tag{2.40}$$

Proceeding in the same way, we multiply the second equation of (2.33) by a test function $q\in Q$, for a suitable Q, and integrate it on the whole domain Ω, obtaining

$$\int_\Omega q\,div\mathbf{u}\,d\Omega = 0 \qquad \forall\,q\in Q. \tag{2.41}$$

Now it is necessary to make some considerations about the two spaces V and Q to which the test functions $\mathbf{v}$ and q belong respectively. The choice of these spaces is very important because it determines if equations (2.40) and (2.41) have a solution and whether this solution is unique. We recall that:

- L^2 is the Hibert space defined in this way

$$L^2(\Omega) = \left\{v:\Omega\to\mathbb{R} : \int_\Omega v(x)^2\,dx < +\infty\right\}.$$

- H^1 is the space of Hilbert such that

$$[H^1(\Omega)]^3 = \{\mathbf{v}\in[L^2(\Omega)]^3 : \nabla\mathbf{v}\in[L^2(\Omega)]^{3\times 3}\}.$$

  In particular,

$$[H^1_{\Gamma_D}(\Omega)]^3 = \{\mathbf{v}\in[H^1(\Omega)]^3 : \mathbf{v}|_{\Gamma_D} = \mathbf{0}\}.$$

Now we can describe the choice of V and Q in our case:

- V is chosen in such a way that the test functions vanish on that boundary portion where the solution is known, so it is defined as follows

$$V = [H^1_{\Gamma_D}(\Omega)]^3. \tag{2.42}$$

  Note that if $\Gamma_D = \partial\Omega$, then $V = [H^1_0(\Omega)]^3$.

- Q is chosen in such a way that, if $\Gamma_N \neq 0$

$$Q = L^2(\Omega). \tag{2.43}$$

Finally, we have to choose the space of the unknowns. On this purpose, for each $t > 0$, we will search a pressure $p(t) \in Q$ and a velocity $\mathbf{u}(t) \in [H^1(\Omega)]^3$ with $\mathbf{u} = \boldsymbol{\varphi}(t)$ on Γ_D and $\mathbf{u}(0) = \mathbf{u}_0$.

After these considerations about spaces V and Q we can observe that, since $\mathbf{v} \in V$, $\mathbf{v}$ is such that $\mathbf{v}|_{\Gamma_D} = 0$ and making use of the boundary condition on Γ_N (see 2.35), we have, $\forall \mathbf{v} \in V$

$$\int_{\partial\Omega} \left(\nu \frac{\partial \mathbf{u}}{\partial t} - p\,\mathbf{n} \right) \cdot \mathbf{v}\; d\gamma = \int_{\Gamma_D} \left(\nu \frac{\partial \mathbf{u}}{\partial t} - p\,\mathbf{n} \right) \cdot \mathbf{v}\; d\gamma + \int_{\Gamma_N} \left(\nu \frac{\partial \mathbf{u}}{\partial t} - p\,\mathbf{n} \right) \cdot \mathbf{v}\; d\gamma = \int_{\Gamma_N} \boldsymbol{\psi} \cdot \mathbf{v}\; d\gamma. \tag{2.44}$$

Finally, the weak formulation of the Navier-Stokes equations (2.33) with initial conditions (2.34) and boundary conditions (2.35) has the following form:

given $\boldsymbol{\psi} \in L^2(\Gamma_N)$, find $\mathbf{u} \in L^2\left(\mathbb{R}^3;\ [H^1(\Omega)]^3\right) \cap C^0\left(\mathbb{R}^+;\ [L^2(\Omega)]^3\right)$ and $p \in L^2\left(\mathbb{R}^+;\ Q\right)$ such that

$$\begin{cases} \displaystyle\int_\Omega \frac{\partial \mathbf{u}}{\partial t} \cdot \mathbf{v} d\Omega + \int_\Omega \nu \nabla \mathbf{u} : \nabla \mathbf{v} d\Omega + \int_\Omega [(\mathbf{u} \cdot \nabla)\mathbf{u}] \cdot \mathbf{v} d\Omega - \int_\Omega p\, div \mathbf{v} d\Omega = \int_{\Gamma_N} \boldsymbol{\psi} \cdot \mathbf{v} d\gamma & \forall \mathbf{v} \in V \\ \displaystyle\int_\Omega q\, div \mathbf{u}\; d\Omega = 0 & \forall q \in Q \end{cases} \tag{2.45}$$

with $\mathbf{u}|_{\Gamma_D} = \boldsymbol{\varphi}$ and $\mathbf{u}|_{t=0} = \mathbf{u}_0$.

We can simplify the notation with the help of bilinear and trilinear forms. On this purpose we introduce:

- the bilinear form $a : V \times V \to \mathbb{R}$ defined as
$$a(\mathbf{u}, \mathbf{v}) = \nu \int_\Omega \nabla \mathbf{u} : \nabla \mathbf{v}\; d\Omega;$$
- the bilinear form $b : V \times Q \to \mathbb{R}$ defined as
$$b(\mathbf{u}, q) = -\int_\Omega q\, div \mathbf{u}\; d\Omega;$$
- the trilinear form $c : V \times V \times V \to \mathbb{R}$ defined as
$$c(\mathbf{w}, \mathbf{z}, \mathbf{v}) = \int_\Omega [(\mathbf{w} \cdot \nabla)\,\mathbf{z}] \cdot \mathbf{v}\; d\Omega.$$

Considering the notation

$$\int_\Omega \mathbf{u} \cdot \mathbf{v}\; d\Omega = (\mathbf{u}, \mathbf{v})$$

and assuming $\boldsymbol{\psi} = \mathbf{0}$ on Γ_N, we could rewrite the weak formulation (2.45) of the Navier-Stokes equations in this way:

find $\mathbf{u} \in L^2\left(\mathbb{R}^3;\ [H^1(\Omega)]^3\right) \cap C^0\left(\mathbb{R}^+;\ [L^2(\Omega)]^3\right)$ and $p \in L^2\left(\mathbb{R}^+;\ Q\right)$ such that

$$\begin{cases} \left(\dfrac{\partial \mathbf{u}}{\partial t}, \mathbf{v} \right) + a(\mathbf{u}, \mathbf{v}) + c(\mathbf{u}, \mathbf{u}, \mathbf{v}) + b(\mathbf{v}, p) = \mathbf{0}, & \forall \mathbf{v} \in V \\ b(\mathbf{u}, q) = 0, & \forall q \in Q \end{cases} \tag{2.46}$$

with $\mathbf{u}|_{\Gamma_D} = \boldsymbol{\varphi}$ and $\mathbf{u}|_{t=0} = \mathbf{u}_0$.

2.2 Numerical approximation

In this section we would like to look after the approximate solution of the problem (2.46). First of all it is necessary to provide a suitable discretization of the equations in space and time. We start from system of equations (2.46).

2.2.1 Space discretization by means of Finite Element Method

The starting point of space discretization is the so-called *Galerkin approximation* obtained by substituting the Hilbert spaces $V = [H^1_{\Gamma_D}(\Omega)]^3$ and $Q = L^2(\Omega)$ with appropriate finite dimensional subspaces.

On this purpose, let V_h and Q_h two families of spaces such that

$$V_h \subset V, \quad \dim V_h = N_h \quad \forall h > 0, \tag{2.47}$$

$$Q_h \subset Q, \quad \dim Q_h = M_h \quad \forall h > 0. \tag{2.48}$$

In this way we obtain a semi-discrete problem, since it involves a discretization only in space and not in time, the so-called *Galerkin problem*:

for each $t > 0$, find $(\ \mathbf{u}_h(t),\ p_h(t)\ ) \in V_h \times Q_h$ such that

$$\begin{cases} \left(\dfrac{\partial \mathbf{u}_h(t)}{\partial t}, \mathbf{v}\right) + a\left(\mathbf{u}_h(t), \mathbf{v}_h\right) + c\left(\mathbf{u}_h(t), \mathbf{u}_h(t), \mathbf{v}_h\right) + b\left(\mathbf{v}_h, p_h(t)\right) = 0, & \forall \mathbf{v}_h \in V_h \\ b\left(\mathbf{u}_h(t), q_h\right) = 0, & \forall q_h \in Q_h \end{cases} \tag{2.49}$$

with $\mathbf{u}_h|_{\Gamma_D} = \boldsymbol{\varphi}_h$ and $\mathbf{u}_h|_{t=0} = \mathbf{u}_{0h}$, where $\boldsymbol{\varphi}_h$ and $\mathbf{u}_{0h}$ are appropriate approximations respectively of $\boldsymbol{\varphi}$ and $\mathbf{u}_0$ in V_h.

The problem now is how to construct in practice the two spaces V_h and Q_h. This is done following the method of the *finite element approximation*.

The Finite Element Method

The Finite Element Method (FEM) is a numerical method for solving problems of mathematical physics such as fluid flow and mass transport. The FEM formulation of the problem results in a system of ordinary differential equations that will be properly discretized in time.

A finite element consists of a triple $(K, \mathbb{P}_r, \Sigma)$ such that

- K is the domain of definition of the element (for example, in the one-dimensional case it is an interval, in 2D is a polygon, in 3D a polyhedron);
- $\mathbb{P}_r$ is the space defined on K of polynomials of global degree less than or equal to r. In addition $\dim \mathbb{P}_r = N_r$ and we consider $\{\varphi_j\}_{j=1}^{N_r}$ a basisi on $\mathbb{P}_r$;

- Σ is a set of functional on $\mathbb{P}_r$,

$$\Sigma = \{\gamma_i : \mathbb{P}_r \to \mathbb{R}\}_{i=1}^{N_r} \quad \text{satisfying} \quad \gamma_i(\varphi_j) = \delta_{ij} = \begin{cases} 1 & \text{if} \quad i \neq j \\ 0 & \text{if} \quad i = j \end{cases}.$$

  The set Σ define the so-called *degrees of freedom*, that is N_r geometrical nodes $\{a_i\}_{i=1}^{N_r}$ such that $\gamma_i(\varphi_j) = \varphi_j(a_i)$.

In our case, $\Omega \subset \mathbb{R}^3$, so we consider a finite decomposition T_h of $\bar{\Omega}$ made of K tetrahedra

$$\bar{\Omega} = \bigcup_{K \in T_h} K. \tag{2.50}$$

In order the mesh T_h is considered admissible, three conditions have to be required:

- $\text{int}(K) \neq \emptyset \quad \forall K \in T_h$;
- $\text{int}(K_1) \cup \text{int}(K_2) = \emptyset \quad \forall K_1, K_2 \in T_h \quad \text{with} \quad K_1 \neq K_2$;
- $\forall K_1, K_2 \in T_h$ with $K_1 \neq K_2$, if $F = K_1 \cup K_2$ then F is a vertex, an edge or a face.

In other words, the tetrahedra must have not empty interior and they are such that the intersection of two of them must be empty or reduced to a common entity, such as a vertex or edge or face.

The mesh T_h is dependent on a parameter h related to the spacing of the grid and defined as

$$h = \max_{K \in T_h} h_K, \tag{2.51}$$

where h_K is the diameter of the element K defined in this way

$$h_K = \text{diam}(K) = \max_{x,y \in K} |x - y| \qquad \forall K \in T_h. \tag{2.52}$$

In addition to this, we say that a family of grids $\{T_h, h > 0\}$ is *regular* if there exists a constant $\delta > 0$ such that

$$\frac{h_K}{\rho_K} \leq \delta \qquad \forall K \in T_h, \tag{2.53}$$

where h_K the largest length in the element edge and ρ_K the diameter of the largest inscribed sphere.

Our aim is to choose appropriately the spaces V_h and Q_h introduced previously. On this purpose we focus our attention on the space $\mathbb{P}_r$, which identifies the set of polynomials whose degree is less or equal than r,

$$\mathbb{P}_r = \left\{ p(x,y,z) = \sum_{0 \leq i+j+l+ \leq r} a_{ijl} x^i y^j z^l, \; a_{ijl} \in \mathbb{R} \right\}. \tag{2.54}$$

In this way, the space of finite element can be defined as

$$X_h^r = \{v_h \in C^0(\bar{\Omega}) : v_h|_K \in \mathbb{P}_r \quad \forall K \in T_h\}, \tag{2.55}$$

that is, the space of globally continuous functions on $\bar{\Omega}$ that are polynomials of degree r on the single elements of the grid T_h.

In our case we define

$$V_h^r = \{v_h \in C^0(\bar{\Omega}) : v_h|_K \in \mathbb{P}_r \quad \forall K \in T_h\} \cap V, \tag{2.56}$$

$$Q_h^s = \{q_h \in C^0(\bar{\Omega}) : q_h|_K \in \mathbb{P}_s \quad \forall K \in T_h\}. \tag{2.57}$$

These are the spaces of finite elements we will use for the numerical solution of our problem. In particular, the test function $\mathbf{v}_h$ will be chosen in $[V_h^r]^3$, whereas the test function q for the pressure in Q_h^s. To sum up, we choose

$$V_h = [V_h^r]^3 \quad \text{and} \quad Q_h = Q_h^s.$$

We note that the problem (2.49) is well posed only if the spaces V_h and Q_h satisfy the *discrete inf-sup condition*, that is there exists a positive constant β, even dependent on h, such that

$$\inf_{q_h \in Q_h} \sup_{\mathbf{v}_h \in V_h} \frac{b(q_h, \mathbf{v}_h)}{||\mathbf{v}_h||_{[H^1(\Omega)]^3} ||q_h||_{L^2(\Omega)}} \geq \beta. \tag{2.58}$$

Considering this important condition, when looking for a compatible couple of spaces, we note that the velocity space V_h should be larger than the pressure space Q_h [5]. Considering $\mathbb{P}_k$ the piecewise finite elements of degree k ($k = 0, 1, \cdots$), examples of finite element spaces that fulfill the *inf-sup* condition are $\mathbb{P}_2 - \mathbb{P}_1$ or $\mathbb{P}_{1\text{bubble}} - \mathbb{P}_1$. Couples like $\mathbb{P}_2 - \mathbb{P}_2$ or $\mathbb{P}_1 - \mathbb{P}_1$ do not satisfy the condition (2.58) and lead to instabilities, but they can still be used adding a suitable stabilization.

Before proceeding with the time discretization, we want to provide an algebraic interpretation of the semi-discrete problem and this is done finding an equivalent matrix formulation of system (2.49). We introduce:

- $\{\beta_j\}_{j=1}^{M_h}$ a basis of Q_h;
- $\{\alpha_j\}_{j=1}^{L_h}$ a basis of V_h^r;
- $\{\boldsymbol{\alpha}_j\}_{j=1}^{N_h}$ a basis of V_h with $\boldsymbol{\alpha}_j = \begin{cases} (\alpha_j, 0, 0) & \text{for} \quad j = 1, ..., L_h \\ (0, \alpha_j, 0) & \text{for} \quad j = L_h + 1, ..., 2L_h \\ (0, 0, \alpha_j) & \text{for} \quad j = 2L_h + 1, ..., 3L_h \end{cases}$,

  where $3L_h = N_h = \dim V_h$.

We observe that, since the problem (2.49) is valid for all elements of the spaces V_h and Q_h, then it is valid also for the elements of the basis.

We decompose the unknowns $\mathbf{u}_h(t)$ and $p_h(t)$ on their respective basis

$$\mathbf{u}_h(\mathbf{x}, t) = \sum_{j=1}^{N_h} u_j(t)\, \boldsymbol{\alpha}_j(\mathbf{x}), \tag{2.59}$$

$$p_h(\mathbf{x}, t) = \sum_{J=1}^{M_h} p_j(t)\, \beta_j(\mathbf{x}), \tag{2.60}$$

where $u_j(t)$ and $p_j(t)$ are the unknowns of our problem.

In this way we can rewrite the semi-discrete problem (2.49) as a system of ordinary differential equations:

$$\begin{cases} M\dfrac{d\,\mathbf{U}(t)}{dt} + A\,\mathbf{U}(t) + C(\mathbf{U}(t))\,\mathbf{U}(t) + B^T\,\mathbf{P}(t) = \mathbf{0} \\ B\,\mathbf{U}(t) = \mathbf{0} \end{cases}, \tag{2.61}$$

where $[\mathbf{U}(t)]_j = u_j(t)$, $[\mathbf{P}(t)]_j = p_j(t)$ and M, A, C and B are the finite element matrices defined in this way

- M is the mass matrix with $m_j = \int_\Omega \boldsymbol{\alpha}_i \cdot \boldsymbol{\alpha}_j \, d\Omega$;
- A is the stiffness matrix with $a_{ij} = a(\boldsymbol{\alpha}_j, \boldsymbol{\alpha}_i)$;
- C is a matrix dependent on $\mathbf{U}(t)$ with $c_{ij} = c(\mathbf{U}(t), \boldsymbol{\alpha}_j, \boldsymbol{\alpha}_i)$;
- B is a matrix with $b_{ij} = b(\boldsymbol{\alpha}_j, \beta_i)$.

2.2.2 Time discretization

We consider a finite domain $[0, T]$ and we divide it in N intervals of length Δt, which is called *time step*. In this way $T = N\Delta t$ and $t_n = n\Delta t$ for $n = 1, \cdots, N$. We denote by $\mathbf{U}^n$ an approximation of $\mathbf{U}(t_n)$ and by $\mathbf{P}^n$ an approximation of $\mathbf{P}(t_n)$.

We notice that, by considering a first order backward Euler discretization, we would have a non-linear algebraic system that requires a too high computational cost. For this reason, the choice is to use the *explicit* Euler method with a *semi-implicit* treatment of the non linear term. In other words we treat implicitly the linear part of the problem and explicitly the non linear convective term.

In this way we obtain

$$\begin{cases} M\,\dfrac{\mathbf{U}^{n+1} - \mathbf{U}^n}{\Delta t} + A\,\mathbf{U}^{n+1} + C(\mathbf{U}^n)\,\mathbf{U}^{n+1} + B^T\,\mathbf{P}^{n+1} = \mathbf{0} \\ B\,\mathbf{U}^{n+1} = \mathbf{0} \end{cases}, \tag{2.62}$$

That is, in matricial form

$$\begin{bmatrix} \frac{M}{\Delta t} + A + C(\mathbf{U}^n) & B^T \\ B & 0 \end{bmatrix} \begin{bmatrix} \mathbf{U}^{n+1} \\ \mathbf{P}^{n+1} \end{bmatrix} = \begin{bmatrix} \frac{M}{\Delta t}\mathbf{U}^n \\ 0 \end{bmatrix} \tag{2.63}$$

or, more easily

$$\begin{bmatrix} \tilde{A} & B^T \\ B & 0 \end{bmatrix} \begin{bmatrix} \mathbf{U}^{n+1} \\ \mathbf{P}^{n+1} \end{bmatrix} = \begin{bmatrix} \mathbf{G} \\ 0 \end{bmatrix}, \tag{2.64}$$

where $\tilde{A} = \frac{M}{\Delta t} + A + C(\mathbf{U}^n)$ and $\mathbf{G} = \frac{M}{\Delta t}\mathbf{U}^n$.

In addition to this, we can observe that the semi-implicit scheme leads to the following stability condition

$$\Delta t \;\leq k\, \frac{h}{\max\limits_{x \in \Omega} |\mathbf{U}^n|}, \tag{2.65}$$

for a suitable k. This condition is not roo much restrictive.

2.2.3 Solution of the linear system

The system (2.62) is a non symmetric linear system which is undefined, that is its eigenvalues are positive and negative. This leads to slow convergence of iterative methods and for this reason suitable preconditioners are required. In our case we use the iterative method called Generalized Minimal Residual method (GMRes) and to speed up convergence we apply the Additive Schwarz Preconditioner. In this section we are going to describe the resolving procedure adopted.

First of all for sake of simplicity, since now on we refer to system (2.63) as the system $A\mathbf{x} = \mathbf{b}$, where $A = (a_{ij}) \in \mathbb{R}^{m\times n}$ is the coefficient matrix, $\mathbf{b} = (b_i) \in \mathbb{R}^m$ is the right side vector and $\mathbf{x} = (x_i) \in \mathbb{R}^n$ is the unknown vector.

One of the main ingredients in our procedure are *Krylov subspaces*. Given $A \in \mathbb{R}^{m\times m}$ and $\mathbf{b} \in \mathbb{R}^m$ we consider the *Krylov sequence*

$$\{\mathbf{b}, A\mathbf{b}, A^2\mathbf{b}, A^3\mathbf{b}, \cdots\}.$$

The *n-th* order *Krylov subspace* is obtained starting from the Krylov sequence in this way

$$\mathcal{K}_n = span\{\mathbf{b}, A\mathbf{b}, A^2\mathbf{b}, \cdots, A^{n-1}\mathbf{b}\}. \tag{2.66}$$

The GMRes method is an iterative method with the property of minimizing at every step the norm of the residual vector over a Krylov space. In order to find step by step this vector we use the Arnoldi iteration, an iterative procedure to obtain an orthonormal basis of a Krylov subspace.

The GMRes method

The method of Generalizes Minimal Residuals (GMRes) was introduced in 1986 by Saad and Schultz [28]. The GMRes method can be used for linear systems $Ax = b$ with non singular square matrix.

The GMRes method starts from the idea of solving a *least square problem* at each step of the iteration, that is at step n we approximate the exact solution $\mathbf{x}^* = A^{-1}\mathbf{b}$ by a vector $\mathbf{x}_n \in \mathcal{K}_n = span\{\mathbf{b}, A\mathbf{b}, \cdots, A^{n-1}\mathbf{b}\}$ such that the residual is minimized, that is

$$||r_n||_2 = ||A\mathbf{x}_n - \mathbf{b}||_2 \to \min. \tag{2.67}$$

The vectors $\mathbf{b}, A\mathbf{b}, \cdots, A^{n-1}\mathbf{b}$ could be almost linearly dependent, so instead of this basis we use the Arnoldi iteration to find $\{\mathbf{q}_1, \mathbf{q}_2, \cdots, \mathbf{q}_n\}$ an orthogonal basis for $\mathcal{K}_n$.

With this new basis the approximate solution $\mathbf{x}_n \in \mathcal{K}_n$ can be written as

$$\mathbf{x}_n = Q_n\mathbf{y}, \tag{2.68}$$

where $Q_n = [\mathbf{q}_1, \cdots, \mathbf{q}_n] \in \mathbb{R}^{m\times n}$ and $\mathbf{y}$ is an appropriate vector of $\mathbb{R}^n$.

In this way, equation (2.67) becomes

$$||r_n||_2 = ||A\mathbf{x}_n - \mathbf{b}||_2 = ||AQ_n\mathbf{y} - \mathbf{b}||_2 \to \min. \tag{2.69}$$

Through the Arnoldi process we find a matrix $\tilde{H}_n \in \mathbb{R}^{(n+1)\times n}$ such that

$$AQ_n = Q_{n+1}\tilde{H}_n. \tag{2.70}$$

Now, inserting relation (2.70) in (2.69) we obtain

$$||r_n||_2 = ||AQ_n\mathbf{y} - \mathbf{b}||_2 = ||Q_{n+1}\tilde{H}_n\mathbf{y} - \mathbf{b}||_2 \to \min. \tag{2.71}$$

Because columns of Q_n are orthogonal, we get

$$||Q_{n+1}\tilde{H}_n\mathbf{y} - \mathbf{b}||_2 = ||\tilde{H}_n\mathbf{y} - Q^*_{n+1}\mathbf{b}||_2. \tag{2.72}$$

The final simplification is for the vector

$$Q^*_{n+1}\mathbf{b} = \begin{bmatrix} \mathbf{q}_1^*\mathbf{b} \\ \mathbf{q}_2^*\mathbf{b} \\ \vdots \\ \mathbf{q}_n^*\mathbf{b} \\ \mathbf{q}_{n+1}^*\mathbf{b} \end{bmatrix}.$$

Recalling the definition of Krylov subspaces and that the columns $\mathbf{q}_j$ of Q_n form an orthogonal basis for $\mathcal{K}_n$ we have

$$\mathbf{q}_1 = \frac{\mathbf{b}}{||\mathbf{b}||_2} \quad \text{and} \quad \mathbf{q}_j^*\mathbf{b} = 0 \ \text{ for } \ j > i.$$

Therefore we have

$$Q^*_{n+1}\mathbf{b} = ||\mathbf{b}||_2\, \mathbf{e}_1 \quad \text{where} \quad \mathbf{e}_1 \in \mathbb{R}^{n+1},\ \mathbf{e}_1 = (1, 0, \cdots, 0)^*. \tag{2.73}$$

At the end, $\mathbf{x}_n$ can be found by minimizing

$$||r_n||_2 = ||\tilde{H}_n\mathbf{y} - ||\mathbf{b}||_2\, \mathbf{e}_1||. \tag{2.74}$$

Algorithm 1 GMRes algorithm

1: Let $\mathbf{q}_1 = \mathbf{b}/||\mathbf{b}||_2$
2: **for** $n = 1, 2, 3, \cdots$ **do**
3: Perform step n of Arnoldi iteration, i.e. compute new entries for $\tilde{H}_n$ and Q_n
4: Find $\mathbf{y}$ that minimizes $||\tilde{H}_n\mathbf{y} - ||\mathbf{b}||_2\, \mathbf{e}_1||$
5: Set $\mathbf{x}_n = Q_n\mathbf{y}$
6: Repeat if the residual is not yet small enough with respect to a suitable tolerance
7: **end for**

Additive Schwarz Preconditioner

The convergence of the GMRes method depends on the spectral properties of the matrix A of the linear system, which is often very ill-conditioned. In order to improve things, the original system $A\mathbf{x} = \mathbf{b}$ is replaced by

$$P^{-1}A\mathbf{x} = P^{-1}\mathbf{b} \qquad \text{(left precontioning)},$$

or

$$AP^{-1}P\mathbf{x} = \mathbf{b} \qquad \text{(right precontioning)}.$$

The linear operator P, called *preconditioner*, is used to make easier to solve the linear system in terms of iterations and CPU time. P is an efficient preconditioner if has the following properties:

- P **is a good approximation of** $\boldsymbol{A}$. This means that P has to act so that $P^{-1}A$ is closed to be the identity matrix.
- P **is efficient**, in the sense that the iteration method converges much faster, in term of CPU time, for the preconditioned system.
- P **or** P^{-1} **can be constructed in parallel**.

The problem is how to construct such an operator P useful for our problem. In our case we use the method of the Additive Schwarz Preconditioner. The following information are taken from [29]. The basic idea is to decompose the computational domain Ω in this way:

$$\bar{\Omega} = \bigcup_{i=1}^{M} \bar{\Omega_i}.$$

This means that Ω is decomposed into M smaller parts Ω_i, called subdomains.

In this way, the original problem can be reformulated within each subdomain Ω_i of smaller size. This family of subproblems is coupled one to another through the values of the unknown solution at subdomain interface. This coupling is then removed at the expense of introducing an iterative process which involves, at each step, solutions on the Ω_i with additional interface conditions $\partial\Omega_i \setminus \partial\Omega$.

Using the Schwarz preconditioner, the computational domain is subdivided into overlapping subdomains. Local Dirichlet-type problems are then solved on each subdomain and the communication between the solutions on the different subdomains is guaranteed by the overlapping region. The additive Schwarz preconditioner can be written as

$$P^{-1} = \sum_{i=1}^{M} P_i A_i^{-1} R_i, \tag{2.75}$$

where M is the number of subdomains which identifies the number of processors in the computation, R_i is an operator that restricts the global vector to the vector lying on subdomain $\partial\Omega_i$, P_i is an operator that prolongate from subdomain Ω_i to Ω and

$$A_i = R_i A P_i. \tag{2.76}$$

Once matrices (2.76) have been formed, the inverse in (2.75) can be computed.

Chapter 3

Generation of geometries

In the following chapter we are going to describe the steps necessary to obtain our volumes and our meshes for the computer simulations presented in Chapter 4. We give some details about the procedure we adopted for the volume extraction from medical images and for the mesh generation in the two cases analyzed: the case of the stenotic branch of a coronary artery with and without guide wire. We recall that our aim is to measure the effect of the guide wire on the pressure drop in coronary stenosis.

3.1 Volume extraction

Clinical radiological images are commonly used to reconstruct the computational domain. In this work, we use Computer Tomography (CT) scans, performed by the Radiology Division of "*Distretto EST dell'APSS di Trento*". An AS CT 28 slice system was employed and the main parameters of the acquisition were the following: slice thickness $0.6\,mm$, slice spacing $0.3\,mm$ and reconstruction matrix 512×512 pixels.

The procedure of reconstruction requires advanced mathematical and numerical tools. In our case, we use the Vascular Modeling Toolkit (VMTK, version 1.3, [31]). VMTK is a collection of scripts and tools which provides segmentation of vascular segments from medical images, geometric analysis and surface data processing of 3D models of blood vessels.

One fundamental problem in medical images analysis is image segmentation, which identifies the boundaries of the analyzed objects and extracts a surface from the image. This procedure allows us to obtain an accurate reproduction of the geometry of the blood vessels. The advantage of using a level-set method is given by the possibility of reconstructing the curves given in the image without the need of parametrizing them. For more technical information about the procedure see [32] and [33].

The patient selected for our study is a male of age 60. On his medical report we become aware that the right coronary and the left circumflex coronary are healthy, the left anterior descending, instead, has a substantial stenosis. In particular we read:

"Left Anterior Descending (LAD): widely ill in the proximal and intermediate tract. Downstream of the eccentric calcific plaque recognizable immediately, after the emergence of the first diagonal branch, a circumferenzial stenosis sustained by circumferential fibrolipid plaque. Other thin fibrolipid plaques also upstream of the stenotic tract, but without significant stenosis".

For this reason, the left anterior descending coronary (LAD) will be the stenotic branch that we are going to reconstruct. In Figure 3.1 the initial DICOM image acquired is reported. We could detect the aorta (1), the left anterior descending coronary (2) with the calcification and the left circumflex coronary (3).

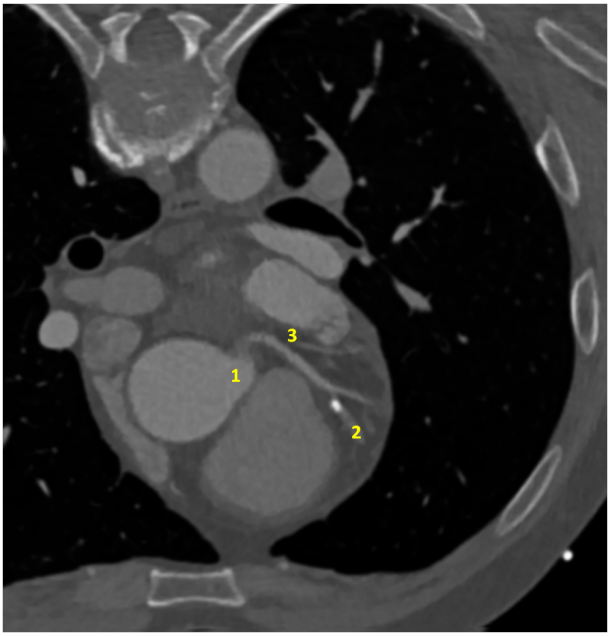

Figure 3.1: CT scan.

We want to extract the surface model of the LAD from the CT scan at our disposal. On this purpose, we follow the instructions of the VMTK Level Set Segmentation procedure. The interactive method substantially consists of placing two seeds on the image and automathically the region between the seeds will be selected. It is possible to proceed by steps, reconstructing the vessel in separate chunks and then merge the results of the different chunks into a single final model. In this process some parameters, which control the deformation of the level set, have to be chosen. For more technical informations see [31], in the *Tutorials* section. In Figure 3.2 we can see some steps of our reconstruction:

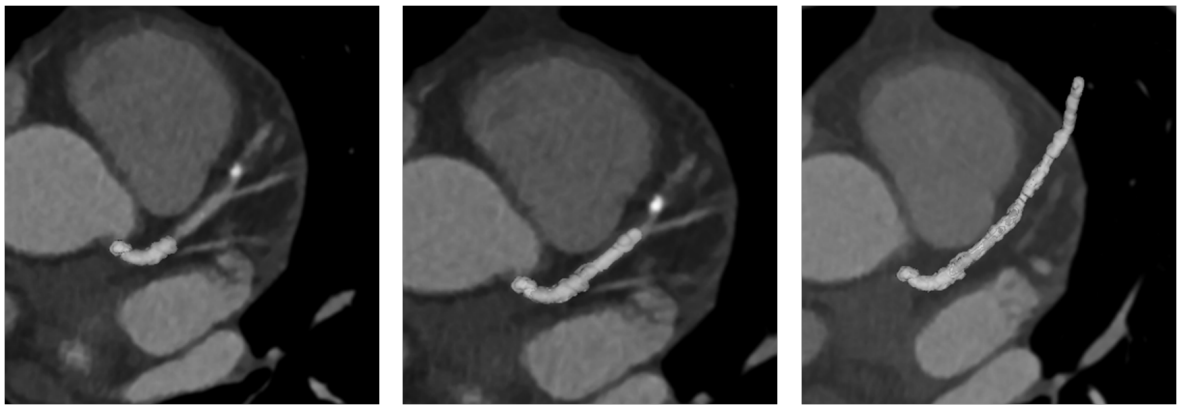

(a) (b) (c)

Figure 3.2: Stenotic branch extraction.

Image segmentation can result in bumpy surfaces. These bumps can affect some results of the hemodynamic simulations (such as wall shear stress distributions) and, for this reason, there is the possibility to increase surface smoothness to improve the surface result.

Another thing to do in order to be able to perform numerical simulations, is to open the model in correspondence of the boundaries through which blood flows. In fact, from the reconstruction procedure, these boundaries are closed. We proceed by opening the surface by clipping the blobby endcaps.

The final *.vtp* file of the stenotic branch is reported in Figure 3.3.

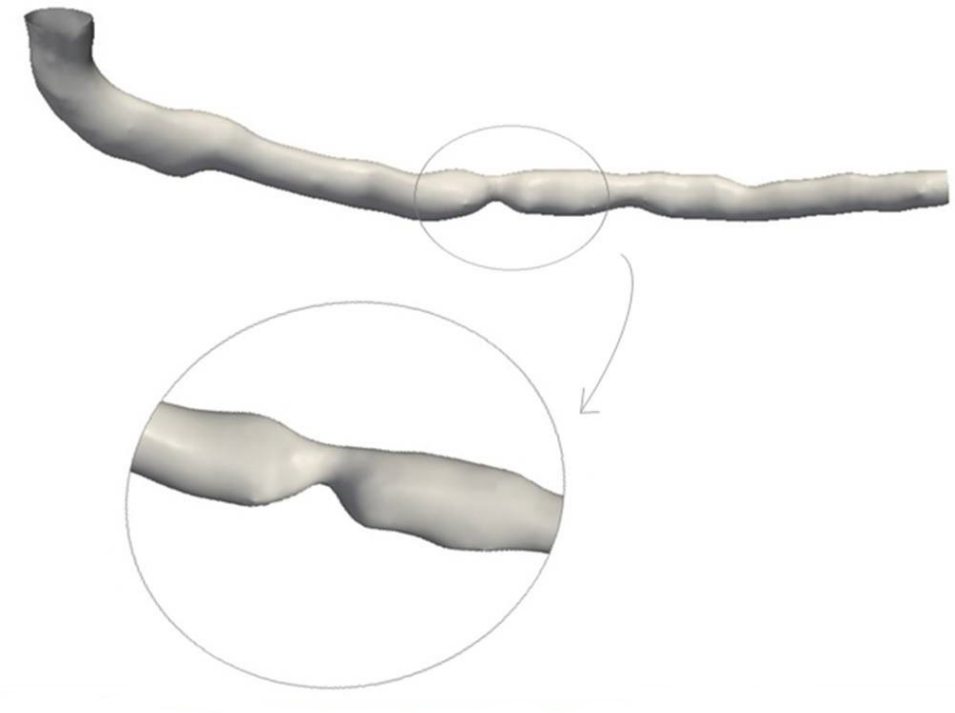

Figure 3.3: Final reconstruction of the stenotic branch with an enlargement of the stenotic tract.

3.2 The guide wire and its insertion in the model

Once the stenotic branch model is obtained, we want to virtually insert the guide wire. In order to simulate at best the medical practice in the FFR detection, we firstly have to learn some physical properties of the instrument used for the pressure measurements in hospitals. Dr. Roberto Bonmassari of the "Santa Chiara Hospital" in Trento makes use of the Verrata Pressure Guidewire. This pressure guide wire is a steerable guide wire with a pressure transducer mounted 3 cm proximal to the tip and has a diameter of 0.014 inch, that is 0.36 mm. It is a device indicated for use to measure pressure in blood vessels during diagnostic angiography and any interventional procedures. As we seen in Chapter 1, these blood pressure measurements provide hemodynamic informations for the diagnosis and treatment of blood vessel disease. We can see the structure of this instrument in Figure 3.4.

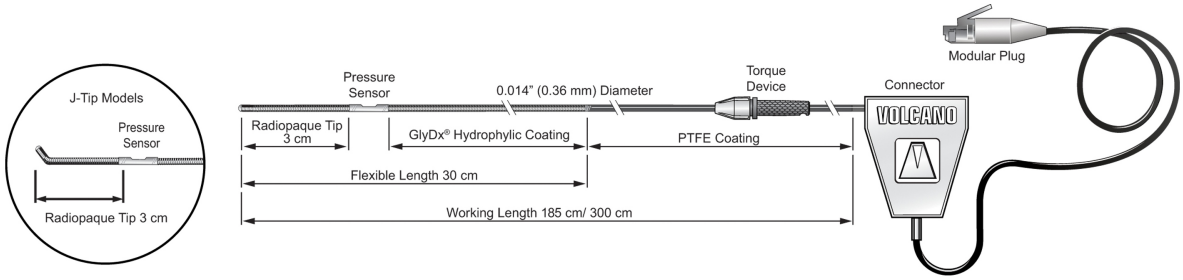

Figure 3.4: The Verrata Pressure Guidewire.

So, the guide could be described by a tube of radius 0.18 mm. The position of the catheter inside the vessel is arbitrary, in the sense that the coronary arteries are curved and tortuous and it is impossible for the transducer to be always located at the center of the vessel.

So, our aim is to create a curvilinear tube of radius 0.18 mm and insert it in our stenotic vessel model. On this purpose, we use **Paraview**, an open-source, multi-platform data analysis and visualization application. This software is principally used for the analysis and the visualization of scientific data sets, but it is also a useful tool to create various geometries, such as cylinders, spheres, cones, etc. The procedure is quite simple: it is sufficient to set some points in the internal model (Figure 3.5) and the radius of the desired tube (0.18 mm in our case). With these elements Paraview returns the tube.

We could see the final result in Figure 3.6.

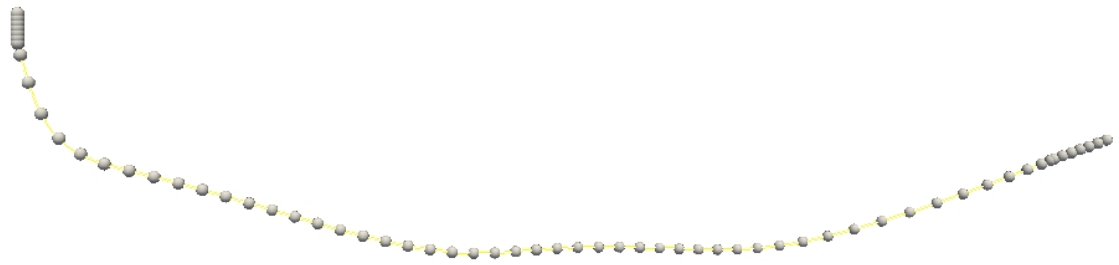

Figure 3.5: Points for the guide creation.

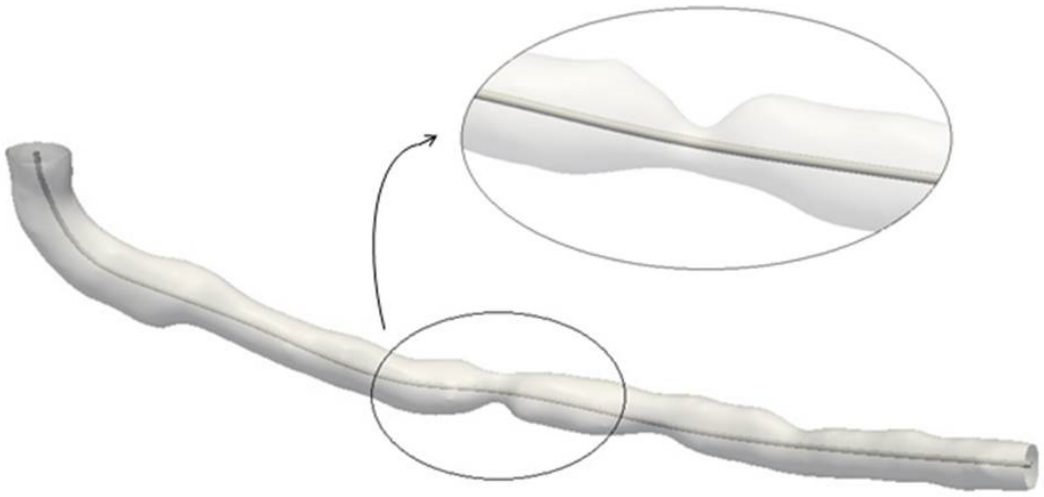

Figure 3.6: Stenotic branch with the guide wire.

3.3 Mesh generation

Once the lumen surface model has been recontructed, the next step consists obtaining the mesh for the computer simulations we will present in Chapter 4. We recall that we want to simulate the presence of the pressure guide wire and its effects on pressure results. We would like also to make a comparison between results with and without guide wire, in order to see if and how FFR is affected by its presence. For this reason we have to construct two meshes, one with and one without the pressure wire.

The meshes were obtained through the use of the code *fsimeshgenerator.py*, a Python code developed in the MOX laboratory at Politecnico di Milano. This code takes as input the *.vtp* file of the geometry and returns two types of meshes: the first one, that we call "**fluid mesh**", is the mesh of the internal vessel and the second one, the "**structure mesh**", is instead the mesh of the vessel's wall. In order to obtain the structure mesh, the code starts from the fluid mesh and proceeds extruding this one.

The guided procedure to obtain the *.mesh* file is quite simple. The code is linked to VMTK, which provides a clear interface. For this reason it is sufficient to follow the instructions which appear on the screen. During the procedure, we are asked to insert some parameters, that define principally the length of the tetrahedra's edges, and the mesh is created in automatically.

So, the output of the code are two *.mesh* files, one for the fluid mesh and one for the structure mesh, which contain all the informations of the grids, in particular the coordinates of the nodes and all the connections between points and tetrahedras edges.

After this panoramic view of the tool at our disposal, in the next subsections, we explain in details the creation of the mesh in the two cases analyzed: the stenotic branch without and with the guide wire. As we will see, the principal problem for our work is to obtain the mesh in the case which considers the presence of the guide. In fact, the *fsimeshgenerator.py* code does not accept the geometry of Figure 3.6 as *.vtp* input file. For this reason, our idea is to start from the pre-existing structure mesh and move the coordinates of the nodes through a MATLAB code. We explain better this procedure in subsection 3.3.2.

3.3.1 Mesh of the stenotic branch without guide wire

In this case the procedure is quite simple. The stenotic branch is turned into a volumetric mesh of linear tetrahedra following the instructions of the *fsimeshgenerator.py* code. During the procedure, we are asked to choose two different parameters α and β which define the mesh elements' dimensions. The two parameters are linked by the following relation:

$$h(R) = \alpha R^{\beta}, \tag{3.1}$$

where R is the radius of the vessel at the level of the considered mesh element. So the element's dimension is dependent on the vessel's radius, allowing us to have smaller mesh elements if the radius of the vessel decreases. This is important because, in this way, high velocity gradients due to the presence of the stenosis can be better caught. In our case we choose

$$\alpha = 0.21,$$

$$\beta = 0.3,$$

obtaining a mesh of about 1.2M tetrahedra.

In Figure 3.7 we show our final result. We name *inlet* the boundary through which the blood flow enters (see A in figure (a)) and *outlet* the one through which the blood goes out (see B in figure (a)).

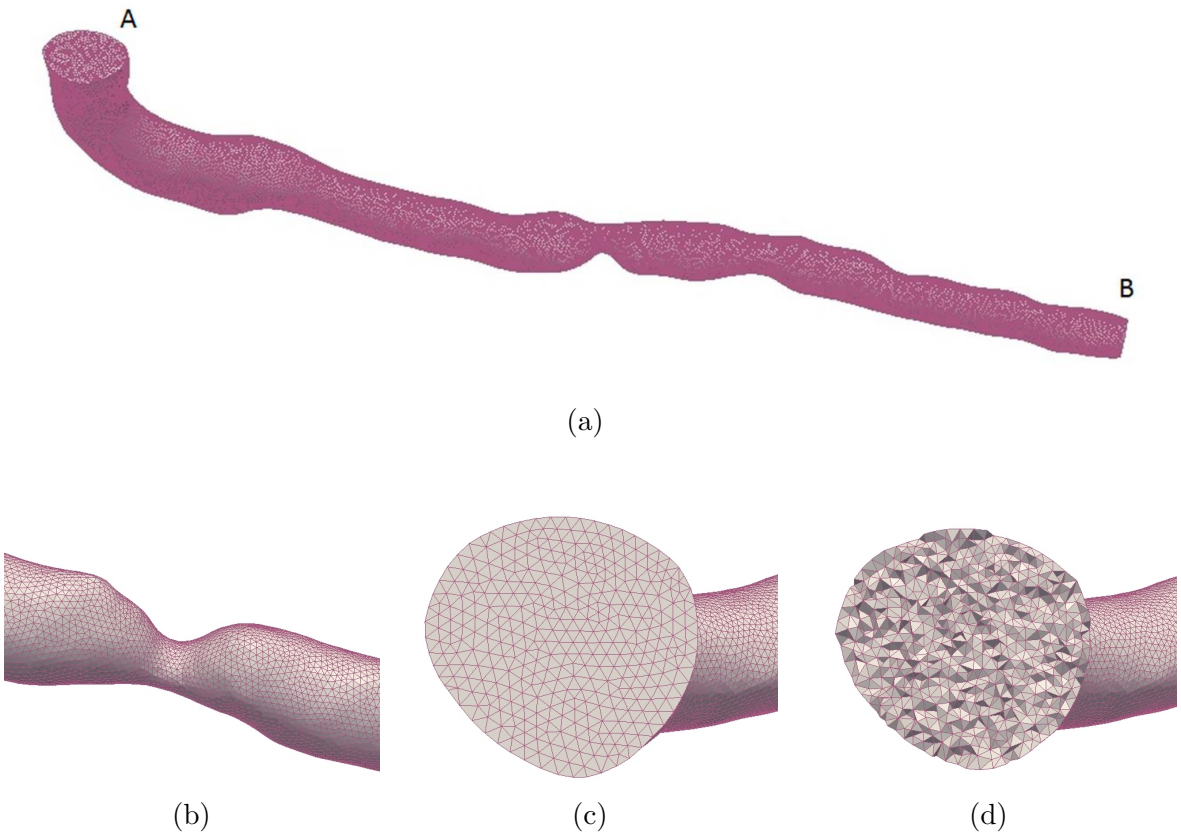

(a)

(b) (c) (d)

Figure 3.7: Final mesh result of the entire stenotic branch (a) and some particulars: (b) mesh elements at the level of the stenosis, (c) the inlet face and (d) the internal mesh.

3.3.2 Mesh of the stenotic branch with guide wire

As we already said, the *fsimeshgenerator.py* code does not generate the mesh with a hole for the guide in automatic, because it does not accept the *.vtp* geometry of Figure 3.6 as input. Our idea is to use the structure mesh generated automatically by the code and change the coordinates of the nodes by means of a MATLAB code. In fact, the *.mesh* file which results from the use of the code, cointains all the informations about the mesh, in particular the coordinates of the nodes and their position in the grid. The aim is to create the guide inside the volume.

For better understanding this procedure, we are now going to explain it on a cylinder. In fact, we firstly test our idea on a cylinder which is more regular than our geometry (every slice has the same diameter and the guide is not curved).

Figure 3.8 shows the final result of the structure mesh obtained through the use of the code. During the procedure, we can choose the number of sublayers and the thickness of the wall layer.

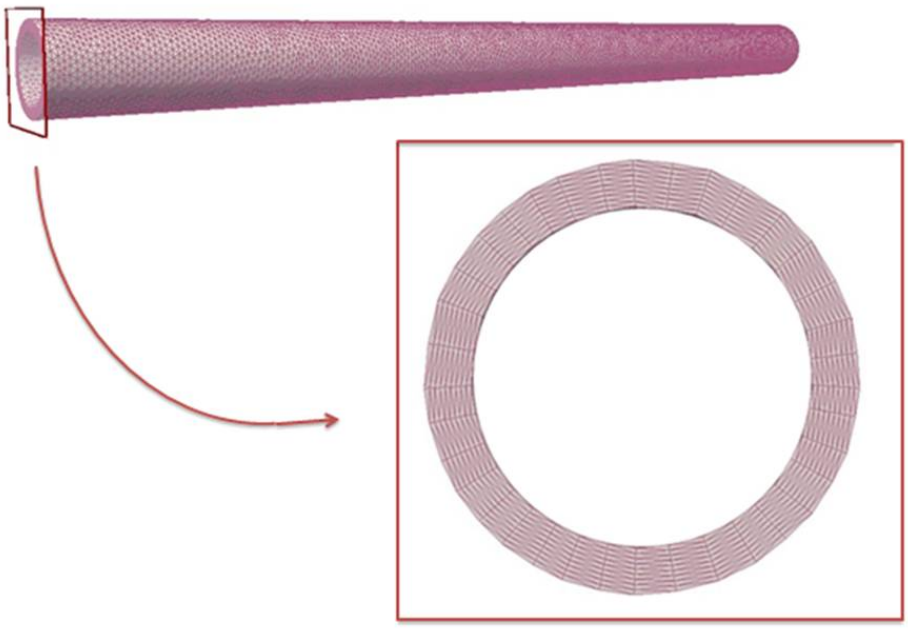

Figure 3.8: Final structure mesh with 9 sublayers on a cylinder.

In Figure 3.9, instead, we give a scheme of what we have (in black) and what we want to obtain (in orange). The black circular crown is our structure mesh, whereas the orange internal part is the part of the volume on which we want to create our mesh.

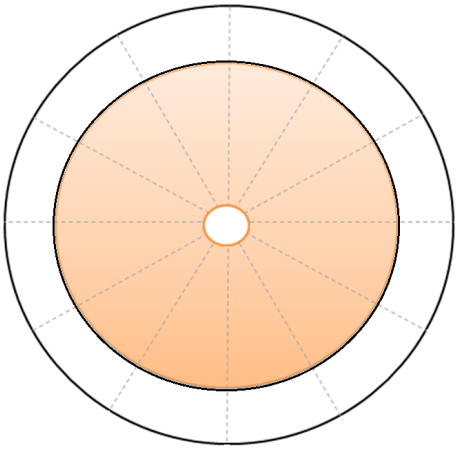

Figure 3.9: Schematic representation of the situation.

So, our aim is to fill the orange volume using and shifting the pre-existing nodes of the structure mesh like in Figure 3.10. We color in blue the points on the external layer, in orange the intermedial points and in yellow the points which lay on the intenal layer. We report the position of these points in the structure mesh (on the left) and in the new configuration (on the right). Of course, the number of the intermedial points depends on how many sublayers we set. In this description we consider only two sublayers, in order to simplify things.

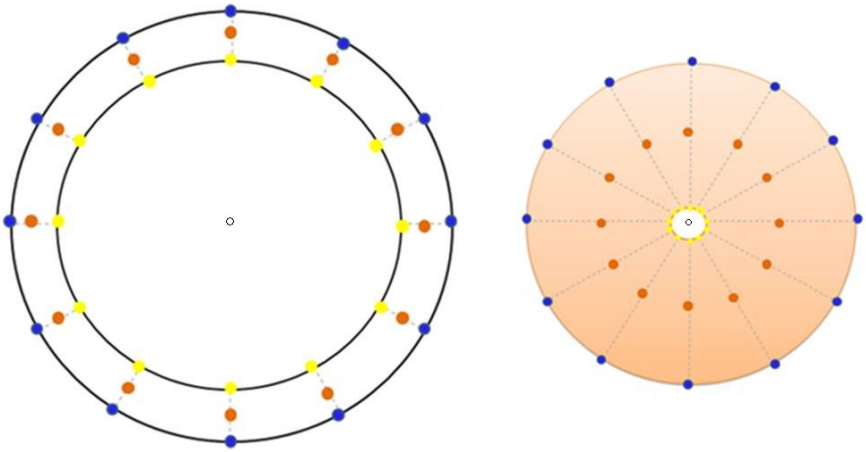

Figure 3.10: Points shift.

Once we have clear in mind what we want to do, we are ready to describe the main idea we use for the implementation of the MATLAB code. Firstly, we have to find a sort of "line of reference" from which calculate the distances of the mesh nodes. This "reference line" is provided by the centerline of the cylinder we are going to consider and it is represented in black in Figure 3.11.

Figure 3.11: Centerline of the cylinder.

We describe the procedure with the help of Figure 3.12:

- in picture (a) we represent the point in the structure mesh. We denote by R_i, R_o and R_e the distances between the centerline and the internal, the intermedial and the external points respectively. In addition to this, we name $a = R_e - R_o$ the distance between intermedial and external points and $b = R_e - R_i$ is instead the distance between the internal and the external points (which corresponds to the thickness of the structure mesh);
- in picture (b) we show our final configuration with the new position of the points. R_i, R_o and R_e are replaced by r_i, r_o and r_e, which are the new distances from the centerline. Moreover, we have $a' = r_e - r_o$ and $b' = r_e - r_i$ instead of a and b.

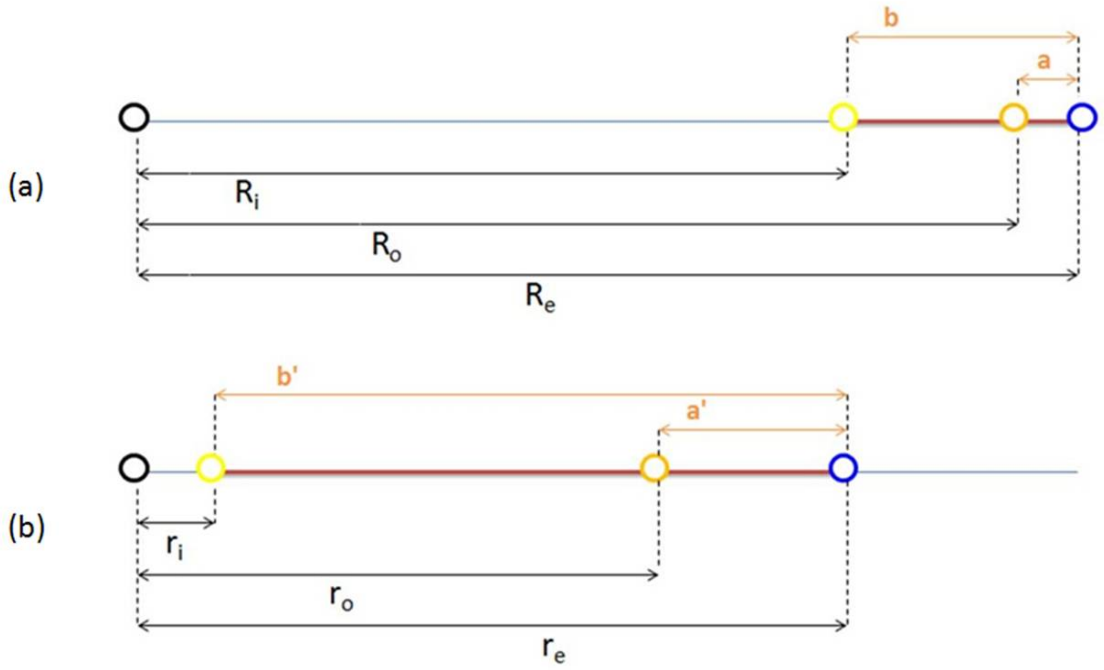

Figure 3.12: Linear representation of the shift.

So, we proceed moving the nodes in this way:

- **internal points** (yellow points). These points are the points that have to form the guide. We shift them in order that the radius R_i becomes

$$r_i = 0.18\ mm,$$

that is, the length of the radius of the guide.

- **external points** (blue points). Also these points have to be shifted because the structure mesh create a thickness with respect to the fluid mesh. We know that

$$thickness = b = \alpha R,$$

where α is a parameter which value is set during the interactive procedure of the mesh generation. So we move external points in such a way that

$$r_e = R_e - b.$$

- **intermedial points** (orange points). The basic idea in shifting these points is to maintain constant the proportion between the distance of the intermedial points from the external and internal ones. Mathematically, we want that

$$\frac{a}{b} = \frac{a'}{b'}. \tag{3.2}$$

We can rewrite equation (3.2) in this way:

$$\frac{R_e - R_o}{R_e - R_i} = \frac{r_e - r_o}{r_e - r_i}, \tag{3.3}$$

from which

$$r_o = -\frac{R_e - R_o}{R_e - R_i}(r_e - r_i) + r_e. \tag{3.4}$$

Implementing a MATLAB code in this way and by running it, we obtain the new coordinates of the nodes which have to replace the original ones in the *.mesh* file. In this way, opening the new *.mesh* file we obtain the "hollow mesh" we were searching for.

The final result for our cylinder for which we create a structure mesh with 9 sublayers, is reported in Figure 3.14. In Figure 3.13 we show the result of the MATLAB code.

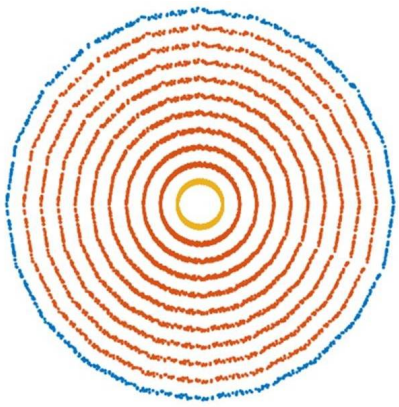

Figure 3.13: Matlab shift.

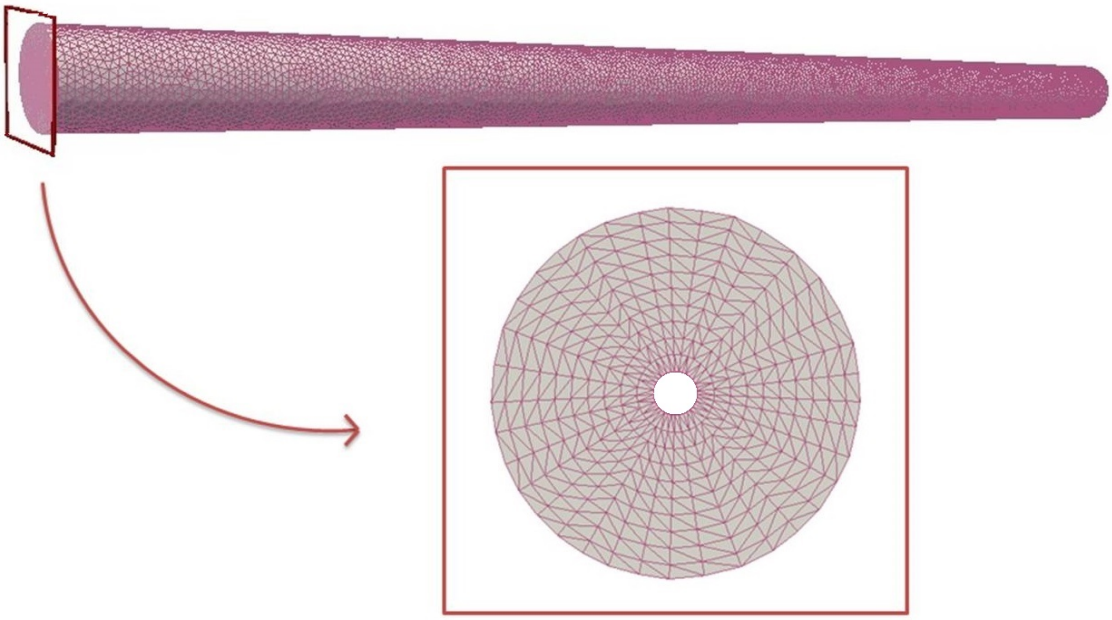

Figure 3.14: Final result for the mesh with the guide wire on a cylinder.

Once the procedure has been successfully applied to the cylinder case, we apply it on our stenotic branch. In this case, the "reference line" is provided by the centerline of the tube we create in section 3.2, that is our guide reconstruction (see the black line of Figure 3.15).

Figure 3.15: Centerline of the guide.

In particular, the structure mesh is obtained extruding a fluid mesh for which we choose

$$\alpha = 0.25,$$

$$\beta = 0.3,$$

we set 12 sublayers and the final mesh is composed by about 1.2M tetrahedra.

After applying the MATLAB code, we obtain our final mesh. As in Subsection 3.3.1, in correspondence of A there is the inlet slice, where is B is instead the outlet slice. We can see it in Figure 3.16.

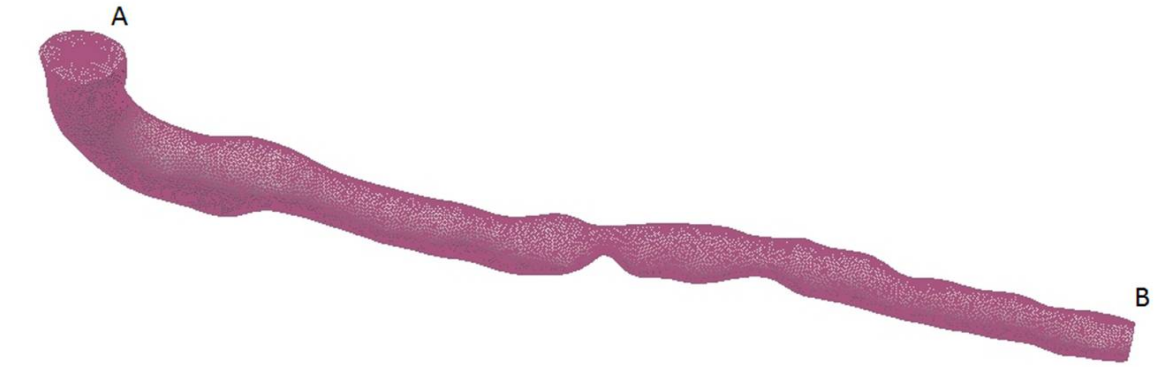

(a)

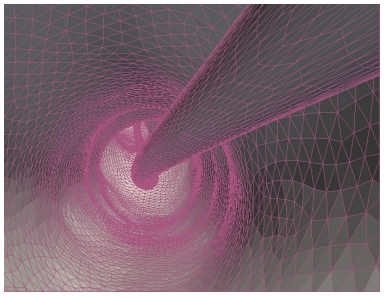

(b)

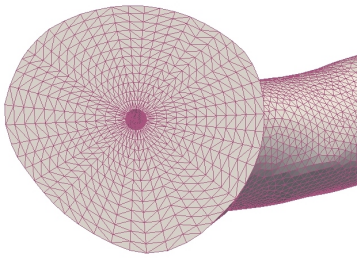

(c)

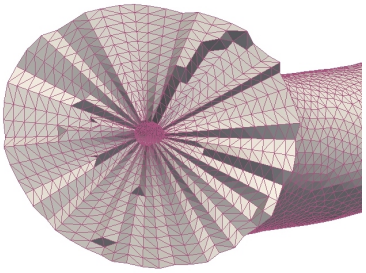

(d)

Figure 3.16: Final mesh result of the entire stenotic branch with guide wire (a) and some particulars: (b) a view of the internal vessel, (c) the inlet face (A) and (d) the internal mesh.

To complete successfully the procedure described above, we needed to perform several tests in order to find an appropriate mesh for our work.

In primis, we pay a lot of attention in setting the points for the creation of the guide in Figure 3.5. After some tests, we understand that the guide has to start and finish in such a way that it is perpendicular to the inlet and the outlet. If this condition is not satisfy, the shift causes points overlays and irregular boundary slice.

Another key problem was about the dimensions of the mesh elements. These elements had to be not too big, because in this way the mesh results very poorly refined, but also not too little, because this situation brings to points overlay after the shift. So, from one test to another, we change the parameter linked to element's dimensions until we find a good mesh. Another thing we change was the number of sublayers of the structure mesh in order to obtain a well-refined mesh.

At the end, with the two meshes at our disposal, we are ready to run the computer simulations for our work. In Chapter 4 we will describe the tools involved in the study and our numerical results.

Chapter 4

Results

In this chapter we give an application of the theoretical aspects previously discussed in Chapter 2. Using the geometry and the meshes obtained in Chapter 3, we describe in details how our numerical simulations have been performed and the results of our study.

4.1 Computational aspects

This section gives some preliminary informations about the tools through which the numerical simulations have been performed and about the choices regarding boundary conditions and velocity profiles. Moreover, in the last subsection we give some details about the physical and computational settings.

4.1.1 The Finite Element Library "LifeV"

The numerical simulations were performed making use of the open source library *LifeV*, a software written in *C++* for the finite element solution of partial differential equations in one, two and three dimensions. *LifeV* was developed by a joint collaboration between the MOX laboratory of the Department of Mathematics of the Politecnico in Milano, the École Polytechnique Fédérale of Lausanne in Switzerland, the INRIA, Paris in France and the Emory University in the U.S.A..

The library includes solvers for incompressible fluid dynamics, linear structural problems, transport in porous media, fluid-structure interaction and electrical conduction in the heart. One of the main field of application is cardiovascular mathematics. There are two versions of LifeV, see [52]; in our thesis we will use the parallel version in order to give the numerical solution of the Navier-Stokes equations in three dimensions.

We mainly work on two files, the file **data** and the file **cylinder.cpp**. The features of these files can be summarized as follows:

- in the file **data** we have the possibility to set the time discretization, the space discretization and all the physical parameters related to the fluid (such as the density ρ or the viscosity μ). Later on we will discuss our choices. The *.mesh* file is considered here, *LifeV* reads the mesh and partitions it using the Parmetis library. It is possible to choose the solver and the preconditioner, in our case we solve the algebraic system with GMRes method combined with an Additive Schwarz preconditioner, as we have already explained in Chapter 2. We select a tolerance of $\tau = 10^{-6}$ for the solver and 100 maximum iterations.

- the file **cylinder.cpp** uses the informations contained in the file **data** for the simulations. It is in this file that is possible to define the appropriate boundary conditions for the problem of interest. Each part of the mesh boundary is marked with a label (such as Inlet = 2, Outlet = 3, ...) and this is used to impose different kinds of boundary conditions for the different pieces of the domain. It is possible to choose principally between Dirichlet (related to the velocity) or Neumann boundary conditions (related instead to the pressure). This file cointains also the velocity profiles. All our choices in this context will be explained in details in the next subsections.

The results of the numerical simulations are then visualized using **Paraview**, a tool useful to visualize and postprocess the results of the numerical experiments, with or without computed quantities (which could be the pressure or the velocity field) displayed on it. Thus, with the help of this application, it is possible to analyze the data using qualitative and quantitative techniques and to produce 3D figures and graphs.

4.1.2 Computational domains, boundary conditions and velocity profiles

In our work we consider two different scenarios. Firsly, we make a brief study on a simple cylinder considering both the *cylindrical case* and the *cylindrical perforated case*. This kind of study is useful to become familiar with the codes at our disposal. Then, we focus our attention on our reconstruction of the stenotic vessel, considering the two configurations with and without guide wire. We refer to the first model as *coronary stenotic case* and to the second model as *coronary stenotic pwg case* (pwg stands for Pressure Guide Wire).

The aim of this section is to describe the four computational domains, specifying the boundary conditions imposed in each part. In addition, we make some considerations about the velocity profiles prescribed at the inlet.

(a) The cylindrical case.

In Figure 4.1 we can see the configuration of the cylindrical case.

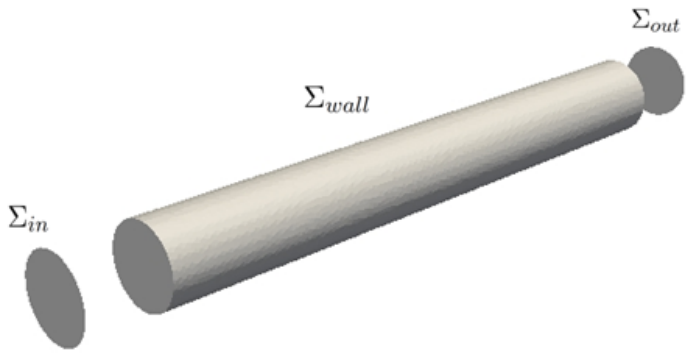

Figure 4.1: Computational domain for the cylindrical case.

The domain is composed by a plane inlet surface Σ_{in}, a plane outlet surface Σ_{out} and by a surface defined by the external wall Σ_{wall}.

Regarding boundary conditions we impose a velocity profile at the inlet Σ_{in}, a no-slip boundary condition on Σ_{wall} and a zero-traction condition at the outlet Σ_{out}. To sum up, the boundary conditions will be:

$$\mathbf{u} = \mathbf{u}_{in} \quad \text{on} \quad \Sigma_{in}, \tag{4.1}$$

$$\mathbf{u} = \mathbf{0} \quad \text{on} \quad \Sigma_{wall}, \tag{4.2}$$

$$\left(\nu \frac{\partial \mathbf{u}}{\partial \mathbf{n}} - p\,\mathbf{n}\right) = \mathbf{0} \quad \text{on} \quad \Sigma_{out}, \tag{4.3}$$

where $\mathbf{u}$ is the fluid velocity and p is the pressure.

At the inlet we impose a velocity distribution given by $\mathbf{u}_{in}$. The inlet slice of our cylinder is oriented in such a way that it has the normal in the y-direction. We have assumed a parabolic profile, also known as *Poiseuille profile*, in order that:

$$\mathbf{u}_{in}(\mathbf{x}, t) = \begin{pmatrix} 0 \\ 2u_z(t)\left(1 - \frac{r^2}{R^2}\right) \\ 0 \end{pmatrix}, \tag{4.4}$$

where t is the time, R is the radius of the inlet surface and $r = \sqrt{x^2 + z^2}$ is the radial coordinate. We denote by u_z the average spatial velocity on the inlet cross sectional area $A = \pi R^2$, defined as:

$$u_z(t) = \frac{Q(t)}{A}, \tag{4.5}$$

where Q is the flow rate which, in general, is a function of time.

In Figure 4.2 we show representative adimensional images of the velocity field prescribed at the inlet section. These profiles are qualitatively independent of the choice of $Q(t)$, which will be described later on.

Figure 4.2: Adimensional images of the velocity field (left) and of the shape of the parabolic velocity profile (right) at the inlet for the cylindrical case.

(b) The cylindrical perforated case.

The geometrical configuration of the cylindrical perforated case is shown in Figure 4.3:

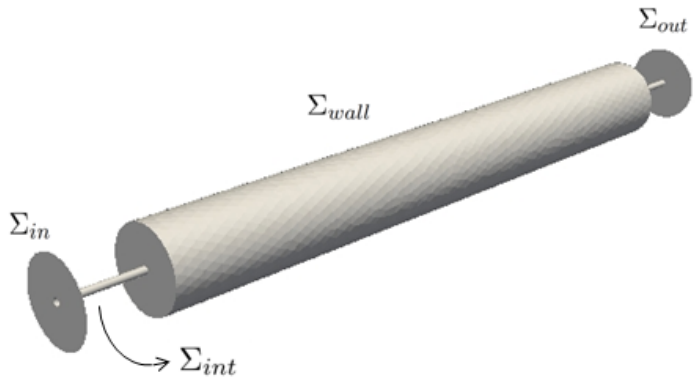

Figure 4.3: Computational domain for the cylindrical perforated case.

The parts of the domain are the same considered in the cylindrical case, apart from Σ_{int} which is the internal wall of the perforated cylinder.

Considering the boundary conditions, they are the same than in the cylindrical case and we have only to add a requirement on the new part of the domain. In particular, on Σ_{int} we impose a no-slip condition. We have:

$$\begin{aligned}
\mathbf{u} &= \mathbf{u}_{in} \quad \text{on} \quad \Sigma_{in}, \\
\mathbf{u} &= \mathbf{0} \quad \text{on} \quad \Sigma_{wall}, \\
\left(\nu \frac{\partial \mathbf{u}}{\partial \mathbf{n}} - p\,\mathbf{n}\right) &= \mathbf{0} \quad \text{on} \quad \Sigma_{out}, \\
\mathbf{u} &= \mathbf{0} \quad \text{on} \quad \Sigma_{int}.
\end{aligned}$$

As in the previous case, at the inlet we impose a Poiseuille velocity profile, which, in this case, considers fluid flow through two concentric cylinders. We set:

$$\mathbf{u}_{in}(\mathbf{x},t) = \begin{pmatrix} 0 \\ 2u_z^g(t)\dfrac{1}{\left(\frac{1-k^4}{1-k^2} - \frac{1-k^2}{ln(\frac{1}{k})}\right)}\left(1 - (\frac{r}{R})^2 - \frac{1-k^2}{ln(\frac{1}{k})} ln(\frac{R}{r})\right) \\ 0 \end{pmatrix}. \tag{4.6}$$

In (4.6), k is a scaling factor defined in this way:

$$k = \frac{R_{int}}{R}, \tag{4.7}$$

where R_{int} is the radius of the internal cylinder, whereas R is the radius of the inlet slice.

In this case we have that, in formula (4.6),

$$u_z^g(t) = \frac{Q(t)}{A_{per}}, \tag{4.8}$$

where

$$A_{per} = \pi(R^2 - R_{int}^2)$$

is the area of the inlet section which considers the presence of the internal cylinder.

In Figure 4.4 we show again representative adimensional images of the velocity field prescribed at the inlet section of the perforated cylindrical case.

Figure 4.4: Adimensional images of the velocity field (left) and the shape of the parabolic profile for the velocity (right) at the inlet for the cylindrical perforated case.

The following (c) and (d) cases consider the model with and without guide wire of the real coronary stenotic vessel from clinical radiological images (the reconstruction has been described in Chapter 3).

(c) The coronary stenotic case.

From now on we refer to this case as *Stenotic case*.

In Figure 4.5 we can see its configuration. See also the corresponding mesh in Figure 3.7 (Chapter 3).

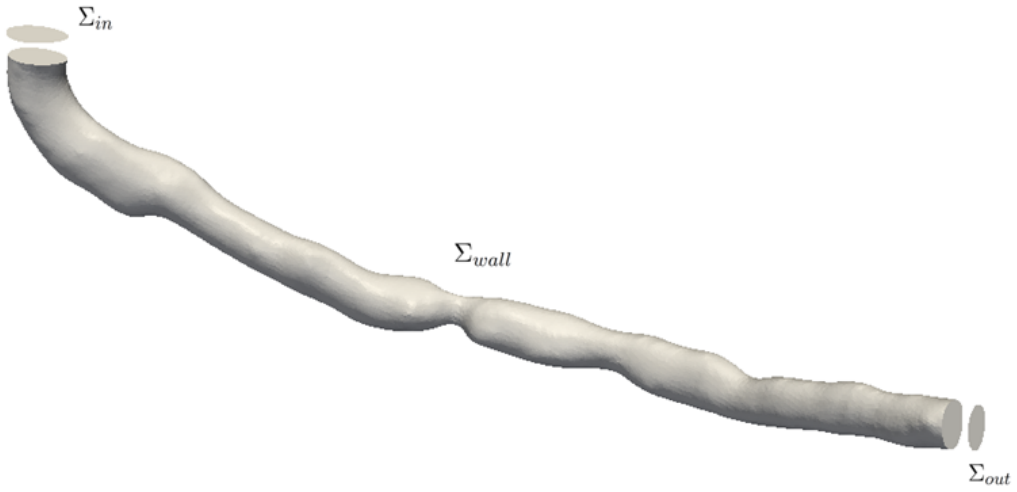

Figure 4.5: Computational domain for the Stenotic case.

As in the cylindrical case, the domain is composed by a plane inlet surface Σ_{in} (through

which blood enters), a plane outlet surface Σ_{out} (through which blood goes out) and by a surface defined by the external wall of the vessel Σ_{wall}.

The boundary conditions are the same as in (4.1), (4.2) and (4.3), that is we impose a velocity profile at the inlet Σ_{in}, a no-slip boundary condition on Σ_{wall} because, since we assume to have rigid walls, the velocity on this layer has to be zero, and a zero-traction condition at the outlet Σ_{out}.

We now make some considerations about the velocity distribution imposed at the inlet. To make our study physically reliable, it is important to impose that this distribution gives rise to physiological flow rates. The inlet slice of our geometry is oriented in such a way that it has the normal in the z-direction. Since in our model the inlet section is not perfectly circular, we have assumed a parabolic velocity profile in order that:

$$\mathbf{u}_{in}(\mathbf{x},t) = \begin{cases} \begin{pmatrix} 0 \\ 0 \\ 2u_z(t)\left(1-\frac{r^2}{R^2}\right) \end{pmatrix} & \text{if} \quad r \leq R \\ \mathbf{0} & \text{elsewhere} \end{cases}, \tag{4.9}$$

where t is the time, R is the radius of the inlet surface and $r = \sqrt{(x-x_0)^2+(y-y_0)^2}$ is the radial coordinate with respect to an origin $O = (x_0, y_0, z_0)$ fixed at the center of the slice. In order to fix the coordinate of this origin, we find the centerline of our model using VMTK and we take as origin O the point of the centerline which lays on the inlet surface.

We have to make some considerations about the choice of the radius R, which in this case is the approximate radius of the inlet slice (it is not perfectly circular). We set R = 2.2 mm, as a mean value of different distances from the origin O and points located on the inlet external ring. In this way, we impose the velocity profile of system (4.9), i.e. the parabolic profile where $r \leq R$ and velocity equal to zero in the other points. Moreover, on the external ring of the inlet slice we impose velocity equal to zero, satisfying the no-slip condition imposed on Σ_{wall}.

In this way, in formula (4.9), u_z is the average spatial velocity on the approximate inlet cross sectional area $A = \pi R^2$, defined as:

$$u_z(t) = \frac{Q(t)}{A}. \tag{4.10}$$

The choice of $Q(t)$ will be descibed later on.

In Figure 4.6 we show representative adimensional images of the velocity field prescribed at the inlet section of the Stenotic case.

Figure 4.6: Adimensional images of the velocity field (left) and the shape of the parabolic profile for the velocity (right) at the inlet for the Stenotic case.

(d) The coronary stenotic pwg case

From now on we refer to this case as *Stenotic pwg case*.

The geometrical configuration of this case with guide wire is shown in Figure 4.7. See also the corresponding mesh in Figure 3.16 (Chapter 3).

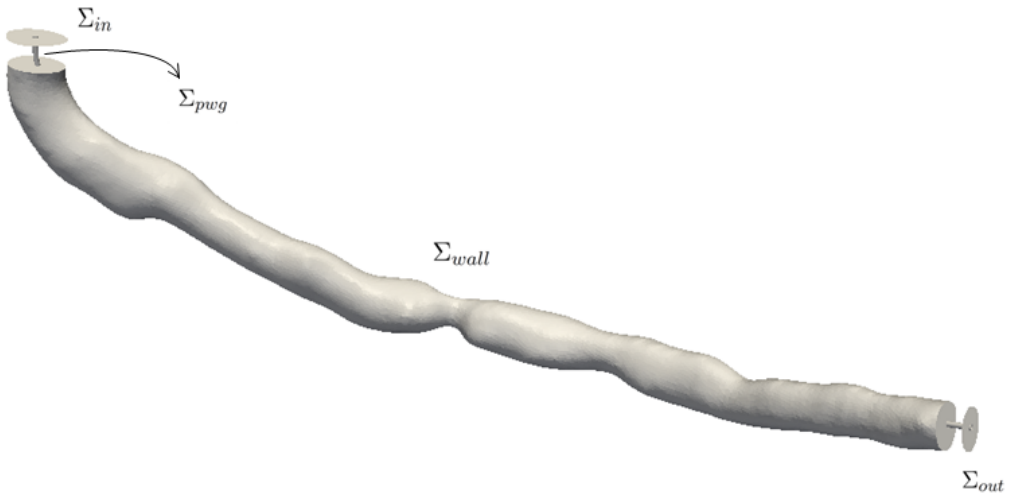

Figure 4.7: Computational domain for the Stenotic pwg case.

The parts of the domain are the same considered in the Stenotic case, apart from Σ_{pwg} which identifies the external wall of the guide.

Considering the boundary conditions, we have to add a requirement on this new part of the domain. Since Σ_{pwg} is, from a physical point of view, the wall of the guide, we impose a no-slip condition. The mathematical equations will be as (4.1), (4.3) and (4.2), with in addition

$$\mathbf{u} = \mathbf{0} \quad \text{on} \quad \Sigma_{pwg}. \tag{4.11}$$

As in the Stenotic case, at the inlet we impose a Poiseuille velocity profile, but its formulation

is different because we have to consider the presence of the guide. We set:

$$\mathbf{u}_{in}(\mathbf{x},t) = \begin{cases} \begin{pmatrix} 0 \\ 0 \\ 2u_z^g(t)\frac{1}{\left(\frac{1-k^4}{1-k^2}-\frac{1-k^2}{ln(\frac{1}{k})}\right)}\left(1-(\frac{r}{R})^2-\frac{1-k^2}{ln(\frac{1}{k})}ln(\frac{R}{r})\right) \end{pmatrix} & \text{if} \quad r \le R \\ \mathbf{0} & \text{elsewhere} \end{cases}, \tag{4.12}$$

We set:

$$k = \frac{R_{pwg}}{R} = \frac{0.18\ mm}{2.2\ mm} = 0.082, \tag{4.13}$$

where R_{pwg} is the radius of the guide, whereas R is the approximate radius of the inlet slice (the same considerations as before are valid).

In formula (4.12),

$$u_z^g(t) = \frac{Q(t)}{A_g}, \tag{4.14}$$

where

$$A_g = \pi(R^2 - R_{pwg}^2)$$

is the approximate area of the inlet section with the presence of the guide.

In Figure 4.8 we show again representative images of the velocity field prescribed at the inlet section.

Figure 4.8: Adimensional images of the velocity field (left) and of the shape of the parabolic profile (right) for the velocity at the inlet for the Stenotic pwg case.

For more details we refer to the work of Stella [21], which reports the mathematical steps to obtain the velocity profiles (4.4) and (4.6).

4.1.3 Physical and computational settings

As for the physical parameters, in the file **data** we have to impose the density ρ and the viscosity μ. The coordinates of our meshes nodes are expressed in millimeters, so these parameters are related to millimeters too. We set:

- density (ρ) : 0.001056 $\frac{g}{mm^3}$,
- viscosity (μ) : 0.0035 $\frac{g}{mm\ s}$.

We now make some considerations about the computational settings.

Regarding the space discretization, in our simulations we always use $\mathbb{P}_{1\text{bubble}}$ Finite Elements for the velocity and $\mathbb{P}_1$ Finite Elements for the pressure. This is a choice that guarantees the stability of the discrete problem (it is a couple of spaces which functions satisfy the *inf-sup condition* (2.58)) and permits reasonable calculation times, but we have to take in account that it is only first order in space. Surely, more accurate results could be obtained using second order numerical simulations.

As for time discretization, we use the BDF 1 scheme. We consider a time step of $\Delta t = 0.01\ s$ for all the simulations.

In our study we consider two types of numerical experiments depending on the value in time of the flow rate Q, which we have to impose. We consider:

- **Steady simulations**: the flow rate Q assumes a constant value k at each time step

  $$Q = k,$$

  and, in this way, it does not depend on time. For these kind of simulations we fix $T_{end} = 0.2\ s$.

- **Unsteady simulations**: the flow rate $Q = Q(t)$ is a function of time. We consider a physiological flow rate taken from literature [18]. In Figure 4.9 we show the flow waveform.

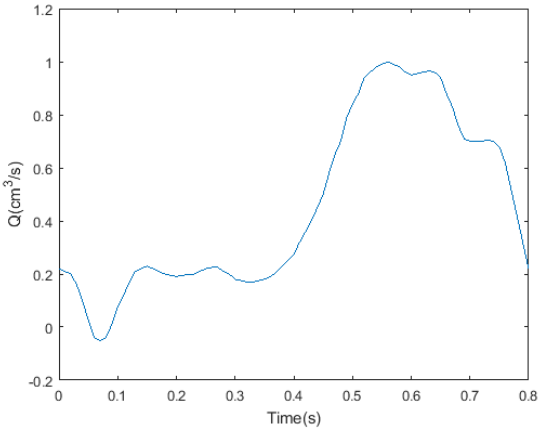

Figure 4.9: Physiological flow rate.

So, in this case we prescribe at the inlet section a flow rate $Q(t)$ which depends on time assuming a parabolic profile.

4.2 Numerical results in the cylinder

As we already said, we firstly make a preliminary study on a cylinder for which we know the analytical value of the solution for the pressure drop in the case of steady flow (see [21]).

We consider a geometry of a cylinder with diameter $D = 4\ mm$, so with radius $R = 2\ mm$, and length $L = 40\ mm$. The radius of the internal cylinder in the cylindrical perforated case is set as $R_{int} = kR = 0.18\ mm$.

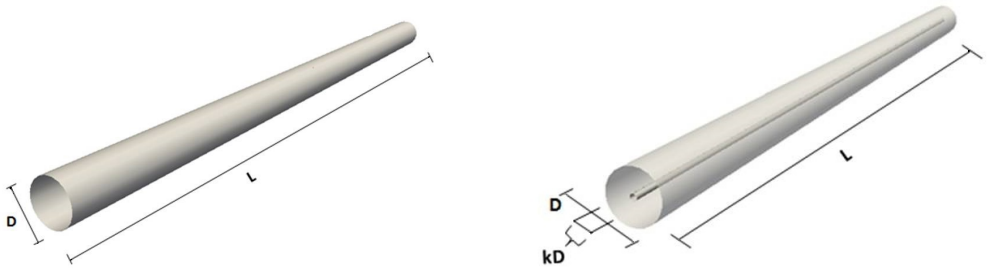

Figure 4.10: Geometries of the cylinder (left) and perforated cylinder (right).

We consider the two domains of the cylindrical case and the cylindrical perforated case. We obtain the mesh for these models using the code *fsimeshgenerator.py* and following the procedure described in Chapter 3.

We run steady simulations using *LifeV* codes and imposing $Q = 2000\frac{mm^3}{s}$ for both cases. As for boundary conditions, we consider those introduced in Subsection 4.1.2. All the results are collected at the end time.

We know the analytical solution of the pressure drop:

- for the cylindrical case:

$$\Delta P^a = \frac{8\,\mu\,L\,Q}{\pi\,R^4}, \tag{4.15}$$

- for the cylindrical perforated case:

$$\Delta P^a = \frac{8\,\mu\,L\,Q}{\pi\,R^4\,(1-k^2)} \frac{1}{\left(\frac{1-k^4}{1-k^2} - \frac{1-k^2}{ln(\frac{1}{k})}\right)}, \tag{4.16}$$

where we denote by ΔP^a the pressure gradient between the pressure at a distance L from the outlet and the pressure at the outlet.

We can compute in this way the relative error as follows

$$\mathbf{e} = \frac{||\Delta P^a - \Delta P^n||_{L^2}}{||\Delta P^a||_{L^2}}, \tag{4.17}$$

where ΔP^a denotes the analytical solution whereas ΔP^n the numerical one.

We perform our simulations and we compare our numerical results of the mean gradient pressure with the analytical solution of the pressure drop (see Figure 4.11 and Figure 4.12).

(a) The cylindrical case - Steady

We consider a mesh of 449592 tetrahedra and in Figure 4.11 we show the comparison between results from the numerical simulations and the analytical solution of the pressure drop.

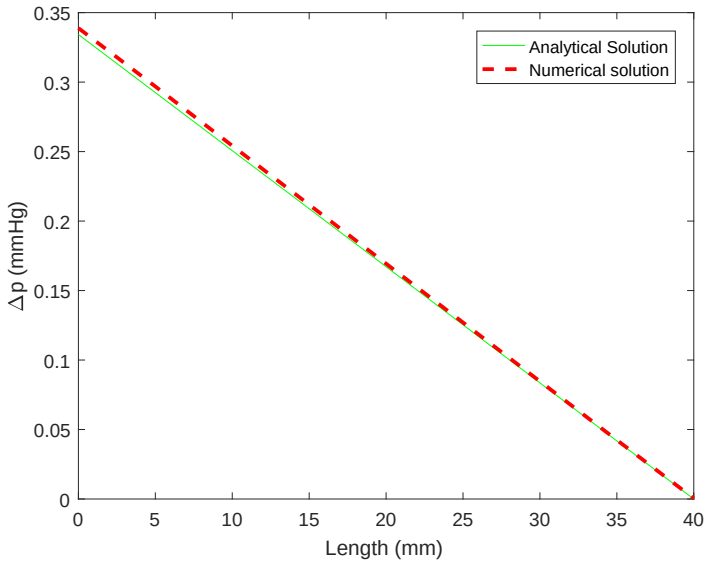

Figure 4.11: Numerical and analytical solution for the cylindrical case.

We obtain an accurate result with an error $\mathbf{e} = 0.0141$.

(b) The cylindrical perforated case - Steady

We consider in this case two different meshes, which differ for number of tetrahedra, in order to evaluate the possible changes in the error. In Table 4.1 we show the number of tetrahedra of the two meshes and the error obtained for each case using (4.17).

Mesh	**# Tetrahedra**	$\boldsymbol{L_2}$**-error**
Mesh1	286065	0.0219
Mesh2	381420	0.0181

Table 4.1: Relative errors for the perforated case computed.

We note that by refining the mesh, the relative error decreases. This fact underline the importance of the mesh in computational studies, because, as we already said in Section (1.6), the mesh is one of the main responsible for the accuracy of the solution.

In Figure 4.12 we show the numerical results of the pressure drop compared with the analytical solution for Mesh2.

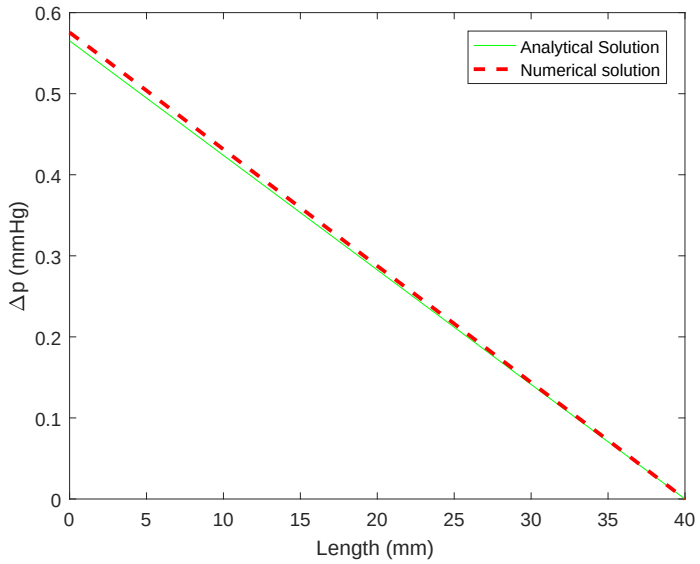

Figure 4.12: Numerical and analytical solution for the perforated case. Mesh2.

4.3 Estimation of the hyperemic flow

We recall that the aim of our work is to investigate the effect of the guide wire on the pressure drop in coronary stenosis by comparing results obtained from simulations in configurations with and without guide wire.

Let g be a function. Its average value $\tilde{g}$ over a space region Γ and a finite time T is

$$\tilde{g} = \frac{1}{T}\frac{1}{A_\Gamma}\int_0^T \int_\Gamma g(t', x')\, dt' dx',$$

where A_Γ is the area of the section considered.

In our case, the temporal average is made on a cardiac cycle, whereas the spatial average is considered on a section Γ orthogonal to the axis. So we will denote with $\Delta\tilde{p}$ the temporal and spatial averaged pressure drop across the stenosis, with $\tilde{p}_a$ and $\tilde{p}_d$ the temporal and spatial aortic and distal pressure respectively. $\tilde{Q}$ is instead the temporal averaged flow rate.

Our numerical results allow us to obtain the value of the mean pressure $\tilde{p}_{a\_num}$ at the inlet slice, and thus, since the pressure at the outlet $\tilde{p}_{d\_num}$ is prescribed, we obtain also the value of $\Delta\tilde{p} = \tilde{p}_{a\_num} - \tilde{p}_{d\_num}$. We use these informations to calculate the FFR. In fact, since the mean aortic pressure $\tilde{p}_a$ is supposed to be known (we find its value in literature):

$$FFR = \frac{\tilde{p}_d}{\tilde{p}_a} = \frac{\tilde{p}_a - \Delta\tilde{p}}{\tilde{p}_a}.$$

In Figure 4.13 we give a schematic representation of $\Delta\tilde{p}$.

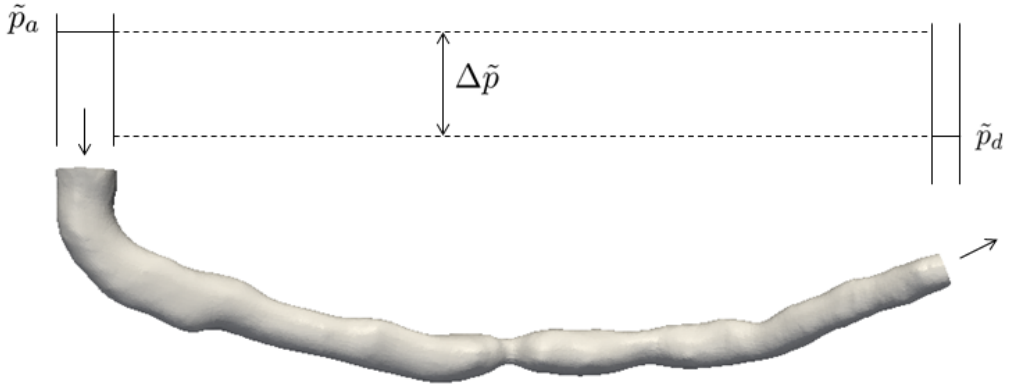

Figure 4.13: Schematic representation of $\Delta\tilde{p}$.

We know that FFR is an important hemodynamic index that has to be considered in hyperemic conditions. In fact, it is only during myocardial hyperemia that the myocardial resistance could be considered constant and blood flow is proportional to driving pressure.

For this reason, the fundamental problem for our work is to find a suitable boundary condition at the inlet which simulates the state of hyperemia. In fact, we do not have any medical measurement about blood flow rate at the inlet section and so the problem is to find a reasonable value for it.

On this purpose, we firstly have to do some considerations about how pressure drop changes in the presence of a stenosis. A normal healthy coronary artery is normally able to accomodate large increases in coronary flow without producing any significant pressure drop. But with the presence of an atherosclerotic plaque, resistance across a stenosis can influence the coronary flow and can limit maximal myocardial perfusion. In particular, the relationship between mean pressure drop and mean flow rate in an epicardial stenosis may be described by the following relation [46]:

$$\Delta\tilde{p} = b\tilde{Q}^2 + a\tilde{Q}, \tag{4.18}$$

where b and a are two coefficients that derive from stenosis geometry and rheological properties of blood. So we understand that the pressure drop across a stenosis not only contains a linear term, but also a quadratic component with respect to flow rate: the linear term $a\tilde{Q}$ is the outcome of the Poiseuille equation in straight conduits, whereas $b\tilde{Q}^2$ is caused by the area reduction through the stenosis.

For the estimation of suitable hyperemic boundary conditions, we decide to follow the procedure suggested by Banerjee et al. [46], in which we find a description of an in vitro experimental and computational study. We are now going to describe the steps of this methodology; for more details we refer the reader to [46], see also [22].

This procedure starts noting that the flow rate imposed at the inlet section influences the pressure drop, and consequently the FFR. In fact, increasing the flow rate $\tilde{Q}$ it is expected that there is also an increase in the pressure drop $\Delta\tilde{p}$. The critical issue is now how to estimate the hyperemic flow rate $\tilde{Q}_h$, where subscript h stands for hyperemic.

To reach this aim, our starting point is what has been proposed in [46], where the authors introduced a methodology which involves the use of a fundamental tool, that is the so-called

$CFR - \tilde{p}_{d,h}$ straight line, where $CFR = \frac{\tilde{Q}_h}{\tilde{Q}_b}$ is the Coronary Flow Reserve defined as maximal hyperemic flow $\tilde{Q}_h$ divided by the basal flow $\tilde{Q}_b$ and $\tilde{p}_{d,h}$ is the mean distal hyperemic pressure. Starting from clinical measurements of a court of patients with different stenosis severity range, the authors find a relationship between the CFR and the corresponding $\tilde{p}_{d,h}$. The equation, found with a linear regression of the data, is:

$$CFR = 0.0645\, \tilde{p}_{d,h} - 1.2461. \tag{4.19}$$

We describe now the two steps of the methodology through which we will find an estimate of the hyperemic flow rate $\tilde{Q}_h$, explaining how the stright line (4.19) is used. This procedure requires some computational simulations, which in our case will be carried out through the use of LifeV codes. For both the cases of our interest, i.e. the Stenotic and the Stenotic pwg case, we proceed following these steps:

(1) **Plot of the $\Delta\tilde{p} - \tilde{Q}$ characteristic curves**.
This step consists in the determination of the coefficient a and b of (4.18). On this purpose, we perform different simulations, prescribing different flow rates $\tilde{Q}$ at the inlet. Then, we compute the pressure gradients $\Delta\tilde{p}$ for each case. We plot the values of $\tilde{Q}$ and the corresponding $\Delta\tilde{p}$ in a 2D plane and, using MATLAB, we make a quadratic regression in order to find the best second degree curve that fits the points:

$$\Delta\tilde{p} = b\tilde{Q}^2 + a\tilde{Q} \tag{4.20}$$

In this way, both for the Stenotic and the Stenotic pwg case, we will be able determine the coefficient a and b that we were looking for.

(2) **Estimation of the hyperemic flow $\tilde{Q}_h$**.
The idea of this second (and last) step is to plot the $\Delta\tilde{p} - \tilde{Q}$ curves found in step (1) and the $CFR - \tilde{p}_{d,h}$ straight line (4.19) in the same plane. For this reason, it is necessary to rewrite equation (4.20) in such a way to obtain a relation which expresses the mean distal pressure $\tilde{p}_d$ as a function of the coronary flow increase $\frac{\tilde{Q}}{\tilde{Q}_b}$. The basal flow $\tilde{Q}_b$ is supposed to be known, see later on for a discussion on this point. With some simply mathematical steps, we obtain:

$$\begin{aligned}
\Delta\tilde{p} &= b\tilde{Q}^2 + a\tilde{Q}, \\
\tilde{p}_a - \tilde{p}_d &= b\tilde{Q}^2 + a\tilde{Q}, \\
\tilde{p}_a - \tilde{p}_d &= {\tilde{Q}_b}^2 b\left(\frac{\tilde{Q}}{\tilde{Q}_b}\right)^2 + \tilde{Q}_b\, a\left(\frac{\tilde{Q}}{\tilde{Q}_b}\right), \\
\tilde{p}_d &= -{\tilde{Q}_b}^2 b\left(\frac{\tilde{Q}}{\tilde{Q}_b}\right)^2 - \tilde{Q}_b\, a\left(\frac{\tilde{Q}}{\tilde{Q}_b}\right) + \tilde{p}_a.
\end{aligned} \tag{4.21}$$

In this way, both for the Stenotic and the Stenotic pwg case, we can plot equation (4.21) and (4.19) in the same $\frac{\tilde{Q}}{\tilde{Q}_b} - \tilde{p}_d$ plane. The intersection of the straight line and the curve returns us:

- a value of $CFR = \frac{\tilde{Q}_h}{\tilde{Q}_b}$, from which we derive the value of $\tilde{Q}_h$ (we recall that $\tilde{Q}_b$ is supposed to be known), that is the hyperemic flow we are looking for. This will be an estimation of the hyperemic flow we have to impose as inlet boundary condition;

- a value of $\tilde{p}_{d,h}$, that is the distal pressure in the hyperemic state. Owing to this value, the procedure allows us to obtain also a theoretical value of the FFR, which we will denote by FFR_t. In fact, since the mean aortic pressure $\tilde{p}_a$ is known, we can compute

$$FFR_t = \frac{\tilde{p}_{d,h}}{\tilde{p}_a}.$$

In the next section we will report our numerical results. As we already said, we will apply the two steps of the procedure to both the cases of our interest. In this way, we will obtain two curves for the step (1) and two estimation of the hyperemic flow for the step (2), one for the Stenotic case and the other for the Stenotic pwg case. The procedure will return also two values of the FFR_t. We will check these values imposing at the inlet the hyperemic flow determined through the methodology and computing the FFR by means of the pressure drop obtained from the simulation.

Before going to analyze our numerical results, we would like to add some considerations about this procedure. Firsly, the $CFR - \tilde{p}_{d,h}$ straight line derives from clinical measurements which require the insertion of a guide wire. Then, the procedure depends on the value of the basal flow $\tilde{Q}_b$, which is supposed to be known and which, due to the autoregulation mechanism, does not depend on the degree of the stenosis. However, we consider this methodology to be a valid procedure to find an estimation of the hyperemic flow rate for our study.

4.4 Numerical results in real coronaries

In this section we report our numerical results and we specify the values of the flow rates prescribed at the inlet section. We proceed by following the two steps of the procedure described in the previous section in order to find the hyperemic flow to impose as inlet boundary condition. This is done for our two cases of interest, i.e. the coronary stenotic branch with and without guide wire. We use the meshes previously created in Chapter 3 reported in Figures 3.7 and 3.16. We perform two types of simulations by means of LifeV codes: firstly we prescribe a constant flow rate at each time step; second, we consider unsteady simulations with a pulsatile inlet blood flow. As for the other boundary conditions we refer to Subsection 4.1.2.

Before starting, we notice that we need to know two ingredients of the procedure for determining the hyperemic flow: the mean aortic pressure $\tilde{p}_a$ and the basal flow rate $\tilde{Q}_b$. We use a physiological value for the mean aortic pressure provided in [46]. For a stenotic branch with an intermediate stenosis, as in our case, an appropriate value is $\tilde{p}_a = 86\ mmHg$. Regarding the basal flow, from literature we find that a typical basal physiological value for a coronary vessel with a diameter of $3\ mm$ is $\tilde{Q}_b = 50\frac{ml}{min}$ [48]. In our case, the inlet slice has an approximate diameter of $4.4\ mm$ and we estimate a reasonable value of $\tilde{Q}_b = 110\ \frac{ml}{min}$ which guarentees the same mean velocity as in [48].

4.4.1 Steady case

We perform simulations with steady flow rate and we collect the pressure drop result Δp at the final time.

Following the step (1) of the procedure (see Section 4.3), we prescribe four different flow rates Q at the inlet, running in this way four simulations for each of the two configurations:

the Stenotic case and the Stenotic pwg case. In Table 4.2 we show our choices for the flow rate and, for each case, the corresponding pressure drop value computed by the numerical simulation.

Q (ml/min)	**Δp $(mmHg)$**	
	Stenotic case	**Stenotic pwg case**
110	3.81	4.74
150	6.50	7.73
270	18.54	20.61
330	26.65	29.11

Table 4.2: Steady flow numerical results.

We observe that, imposing the same flow rate in the two configurations, we register higher values of the pressure drop in the case with guide wire.

In Figure 4.14 we plot our results in a 2D plane; then in Table 4.3 we report the values of a and b in (4.20).

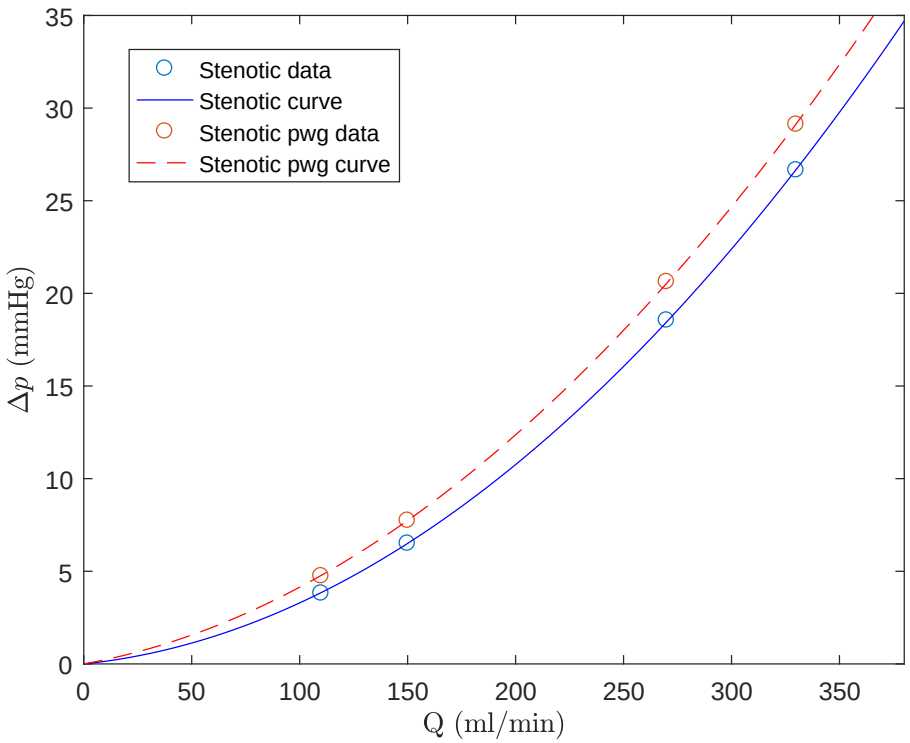

Figure 4.14: Steady flow curves.

Case	Δp - Q curve
Stenotic case	$\Delta p = 0.00021\ Q^2 + 0.012\ Q$
Stenotic pwg case	$\Delta p = 0.00021\ Q^2 + 0.021\ Q$

Table 4.3: Steady flow Δp - Q curves equations.

We observe that the quadratic term in the $\Delta p - Q$ relation is the same for the two cases analyzed. As for the linear term, we note that it increases by a factor of 1.75 (0.021/0.012) with the insertion of the guide wire. As expected, in fact, the insertion of the guide wire increases the resistance to flow by elevating the viscous loss expressed by the linear term aQ.

According to step (2) in the procedure (see Section 4.3), in Figure 4.15 we plot the $\Delta p - Q$ curves in the $\frac{Q}{Q_b} - p_d$ plane according to (4.21). Moreover, we draw the $CFR - p_{d,h}$ straight line reported in (4.19) and, finding the intersection between the curves and the line, we provide an estimation of the hyperemic flow Q_h. Then, in Table 4.4 we collect our results. Notice, as expected, the elevated values of the estimated hyperemic flow rates.

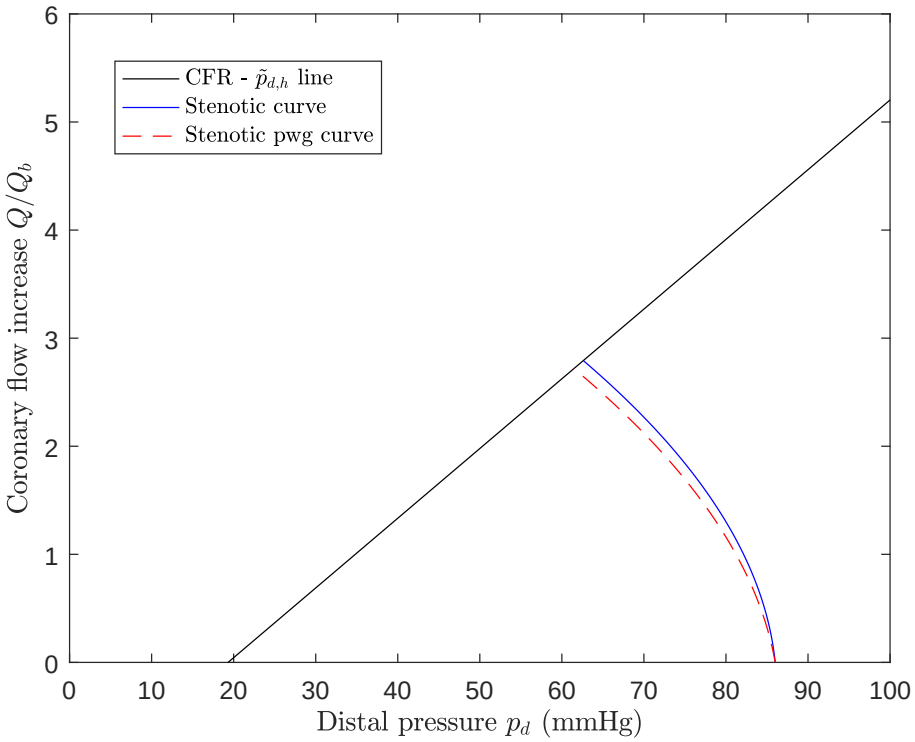

Figure 4.15: Steady flow intersection of the curves with the $CFR - p_{d,h}$ line.

Case	Q_h (ml/min)	CFR	$p_{d,h}$ (mmHg)	FFR_t
Stenotic case	307.17	2.79	62.61	0.728
Stenotic pwg case	299.04	2.72	61.47	0.715

Table 4.4: Steady numerical results: the hyperemic flow Q_h, the CFR value, the distal pressure p_d and the FFR_t.

Next, we performed two further numerical simulations (one for the Stenotic case and one for the Stenotic pwg case) where the estimated hyperemic flow rates are prescribed at the inlet sections. This will allow us to verify if the theoretical value FFR_t of FFR estimated by the procedure is in an accordance with the value computed owing to numerical experiments.

- Stenotic case.
  We impose $Q_h = 307.17 \frac{ml}{min}$, at the final time we measured $\Delta p = 23.34\ mmHg$. In this way
  $$FFR = \frac{p_d}{p_a} = \frac{p_a - \Delta p}{p_a} = \frac{86 - 23.34}{86} = 0.729. \tag{4.22}$$
- Stenotic pwg case.
  We impose $Q_h = 299.04 \frac{ml}{min}$, at the final time we measured $\Delta p = 24.51\ mmHg$. In this way
  $$FFR = \frac{86 - 24.51}{86} = 0.715. \tag{4.23}$$

These results minimally differ from values estimated and reported in Table 4.4.

4.4.2 Unsteady case

In this subsection we describe the results obtained with the analysis of a physiological unsteady flow prescribed at the inlet. The imposition of a physiological flow rate permits us to get closer to reality, because we know that coronary blood flow features significant changes along the cardiac cycle. As we already said in Subsection 4.1.3, we consider the flow rate waveform of Figure 4.9. The cardiac cycle lasts 0.8 s.

According to step (1) of the procedure for the estimation of the hyperemic flow reported in Section 4.3, we start finding the quadratic relationship between $\Delta\tilde{p}$ and $\tilde{Q}$ in both the cases of our interest (Stenotic and Stenotic pwg case). In Table 4.5 we collect our results. We consider three different flow rates and we report the corresponding pressure drop value computed by the numerical simulation.

$\tilde{Q}$ (ml/min)	$\Delta\tilde{p}$ $(mmHg)$	
	Stenotic case	Stenotic pwg case
110	5.21	6.09
150	9.15	10.28
293	32.27	32.85

Table 4.5: Unsteady flow numerical results.

We note that the values of the pressure drop are slightly higher in the Stenotic pwg case with respect to the Stenotic one.

In Figure 4.16, instead, we plot the $\Delta\tilde{p} - \tilde{Q}$ curves and we show the equations of these curves in Table 4.6, determining in this way coefficients a and b of (4.20).

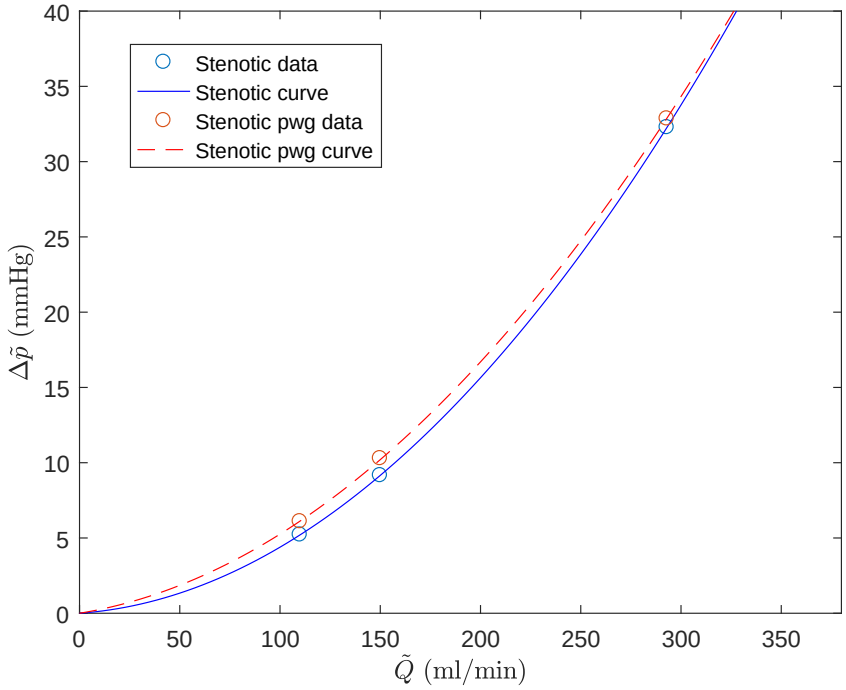

Figure 4.16: Unsteady flow curves.

Case	$\boldsymbol{\Delta p(mmHg)}$ **- Q curve**
Stenotic case	$\Delta p = 0.00034\ Q^2 + 0.0095\ Q$
Stenotic pwg case	$\Delta p = 0.00031\ Q^2 + 0.022\ Q$

Table 4.6: Unsteady flow $\Delta\tilde{p}$ - $\tilde{Q}$ curves equations.

We observe that the difference between the two curves is minimal. It seems that by increasing the flow rates, the value of the pressure drops, for the Stenotic and Stenotic pwg case, ends up to be the same. Also in this case, the b coefficient of the quadratic term is similar in both cases, the a coefficient instead increases by a factor of 2.3 (0.022/0.0095), as expected since the insertion of the guide wire increases the resistance to flow.

As described in step (2) of the procedure (Section 4.3), we finally report the graph through which we find the intersection between the $\Delta\tilde{p} - \tilde{Q}$ curve in the $\frac{\tilde{Q}}{\tilde{Q}_b} - \tilde{p}_d$ plane with the $CFR - \tilde{p}_{d,h}$ straight line (4.19), see Figure 4.17. In Table 4.7 we collect the results of the procedure.

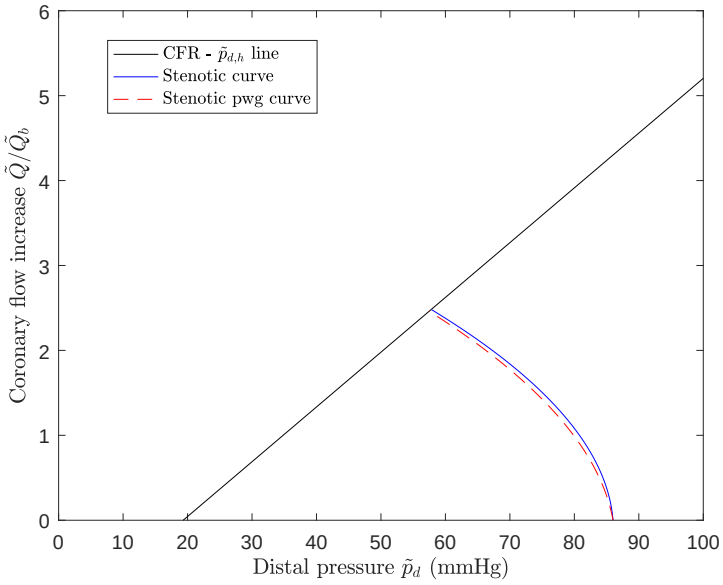

Figure 4.17: Unsteady flow intersection of the curves with the $CFR - p_{d,h}$ line.

Case	$\tilde{\boldsymbol{Q}}_{\boldsymbol{h}}$ **(ml/min)**	**CFR**	$\tilde{\boldsymbol{p}}_{\boldsymbol{d,h}}$ **(mmHg)**	$\boldsymbol{FFR_t}$
Stenotic case	273.02	2.48	57.80	0.672
Stenotic pwg case	270.72	2.46	57.46	0.668

Table 4.7: Unsteady numerical results: the hyperemic flow $\tilde{Q}_h$, the CFR value, the distal pressure $\tilde{p}_d$ and the FFR_t.

Next, as we made for the steady case, we performed two further numerical simulations (one for the Stenotic case and one for the Stenotic pwg case) where the estimated hyperemic flow rates are prescribed at the inlet sections. This allow us to verify the FFR_t values obtained with the procedure whit respect to the FFR computed owing to numerical experiments.

- Stenotic case.
  We impose $\tilde{Q}_h = 273.02 \frac{ml}{min}$, we measured $\Delta\tilde{p} = 28.23\ mmHg$. In this way

$$FFR = \frac{\tilde{p}_d}{\tilde{p}_a} = \frac{\tilde{p}_a - \Delta\tilde{p}}{\tilde{p}_a} = \frac{86 - 28.23}{86} = 0.672. \tag{4.24}$$

- Stenotic pwg case.
  We impose $\tilde{Q}_h = 270.72 \frac{ml}{min}$, we measured $\Delta\tilde{p} = 28.61\ mmHg$. In this way

$$FFR = \frac{86 - 28.61}{86} = 0.667. \tag{4.25}$$

We see that, also for the unsteady case, the FFR values do not differ from those estimated by the procedure (FFR_t in Table 4.7).

4.5 Discussion of the results

In this section we want to make some considerations about our numerical results. In the first subsection we make a sort of quantitative analysis of what we obtain. In the second subsection, instead, we would like to analyze the hemodynamic features of the model, in particular in the zone of the stenosis.

4.5.1 Discussion of the numerical results

In Table 4.8 we sum up the estimates of the hyperemic flows.

$\tilde{Q}_h$ **results (ml/min)**		
Case	Stenotic case	Stenotic pwg case
Steady case	307.17	299.04
Unsteady case	273.02	270.72

Table 4.8: Estimated values of the hyperemic flow $\tilde{Q}_h$.

We note that the hyperemic flow imposed at the inlet section is different for the two configurations, with and without guide wire. In particular, there is a reduction of $\tilde{Q}_h$ introducing the guide wire in both steady and unsteady case. This is correct from a theoretical point of view, because, since we are studying a system in hyperemic conditions, any resistance added to blood flow causes a flow decrease. The reduction is of 2.64% for the steady case, of 0.84% for the unsteady one.

Then, we observe that the flow rate we have to impose by means of a steady simulation is, in general, higher than the unsteady one. In particular, it increases of 11.1% for the Stenotic case and of 9.5% for the Stenotic pwg case.

Now we focus our attention on the FFR diagnostic index. We recall that our aim is to show the effects of the insertion of the guide wire on the pressure drop in our stenotic model. In Table 4.9 we sum up all our results: the measure of the FFR by means of steady and unsteady simulations and the FFR value provided by the clinicians involved in the study for the patient of our interest.

FFR final results		
Case	Stenotic case	Stenotic pwg case
Steady case	0.729	0.715
Unsteady case	0.672	0.667
Clinical measure	—	0.680

Table 4.9: Results about FFR measurements.

Firstly, we observe that the FFR results for the Stenotic pwg case are very closed to its clinical measure, in particular imposing at the inlet the physiological flow rate waveform 4.9 (we find 0.667 compared to the 0.680).

Then, we observe that the FFR values for the Stenotic case are slightly larger than in the Stenotic pwg case. If we consider the percentage variation of the FFR due to the introduction of the pressure guide wire, we note a reduction of 1.9% in the steady case, while a reduction of 0.7% through the use of the unsteady simulations.

We know that the unsteady simulations are surely more closed to reality from a physical point of view, but, at the same time, they require an higher computational cost with respect to the steady ones. This fact reduces the clinical application of the unsteady procedure. For this reason, we conclude our numerical work by performing an unsteady simulation with the value of $\tilde{Q}_h$ estimated by considering steady simulations in the procedure of Section 4.3 for the Stenotic pwg case. So we impose at the inlet a flow rate that follows the waveform reported in Figure 4.9, with $\tilde{Q}_h = 299.04 \, \frac{ml}{min}$. We obtain a pressure drop $\Delta p = 34.07 \, mmHg$ corresponding to an FFR of 0.604. This measure differs of 9.4% from the FFR value obtained by an unsteady simulation with the properly estimate of the hyperemic flow (0.604 versus 0.667). This means that the imposition of the steady hyperemic flow rate value in an unsteady simulation leads to an understimation of the FFR.

We conclude that, according to our approach, the effect of the insertion of the guide wire on the FFR measurements seems to be not so relevant in terms of FFR computation. Of course, our study is only a preliminary approach and it is affected by several assumptions. These results could be improved by relaxing some hypotheses, as we will show in Chapter 5.

In any case, we stress the excellent agreement found by the clinical measure of FFR and its estimates provided by the numerical simulations. This allows us to state that our approach based on computational simulations is accurate and suitable for this kind of analysis.

4.5.2 Discussion of blood dynamics

In this subsection we want to make an analysis of the hemodynamics in our two configurations of interest, with and without guide wire, paying particular attention to the possible formation of vortices and disturbed flow due to the presence of the stenosis. In this post-processing analysis, we consider the results of our simulations obtained imposing the unsteady flow waveform with the estimate of the hyperemic flow of Table 4.8, that is $\tilde{Q}_h = 273.02 \, \frac{ml}{min}$ for the Stenotic case and $\tilde{Q}_h = 270.72 \, \frac{ml}{min}$ for the Stenotic pwg case.

In Figure 4.18 we report the velocity field. We consider a longitudinal slice of our stenotic branch which highlight what happens near the stenosis. The figures are taken at different moments of the cardiac cycle, in particular at: pre-systolic point $t = 0.03 \, s$ (first row), systolic point $t = 0.07 \, s$ (second row), early diastole $t = 0.48 \, s$ (third row), diatolic peak $t = 0.55 \, s$ (fourth row) and post-diastolic phase $t = 0.67 \, s$ (fifth row). We recall that the systolic point is the moment of minimum velocity, at the diastolic point instead blood velocity reaches its maximum.

We observe that the asymmetrical shape of the stenosis influences the flow pattern of blood and consequently, the pressure drop. We can find several work which investigate the correlation between the shape of the stenosis and the overall pressure drop across the blockage region of artery, we cite for example [55].

In addition to this, we know that the presence of a stenosis, combined with high blood velocity, can generate high frequency velocity fluctuations whitin the blood flow, leading to

the formation of vortices. We analyze the stremlines in order to highlight the formation of vortices downstrem the stenosis. The streamline distribution uses lines to indicate the flow direction. The color and length of the line show the flow velocity, magnitude and direction.

In Figure 4.19 we show the streamlines for our cases. On the left we report the situation of the Stenotic case, on the right of the Stenotic pwg case. The instants at which the figures are taken are the same as for the velocity field.

If we observe what we obtain, it seems that the vortices are a bit more compact in the Stenotic pwg case with respect to the Stenotic one, especially at the diastolic peak ($t = 0.55\ s$). The reason of this fact could be that the presence of the pressure guide wire limits the space for the possible formation of vortices.

We want still to underline that our study is only a preliminary study of the influence of the guide wire on a real coronary stenosis. As we said in Subsection 4.1.3, we always use first order numerical simulation and surely, by running simulations of second order, we could obtain better results. In Chapter 5 we are going to explain the limits of our procedure and the possible improvements that could lead to better results.

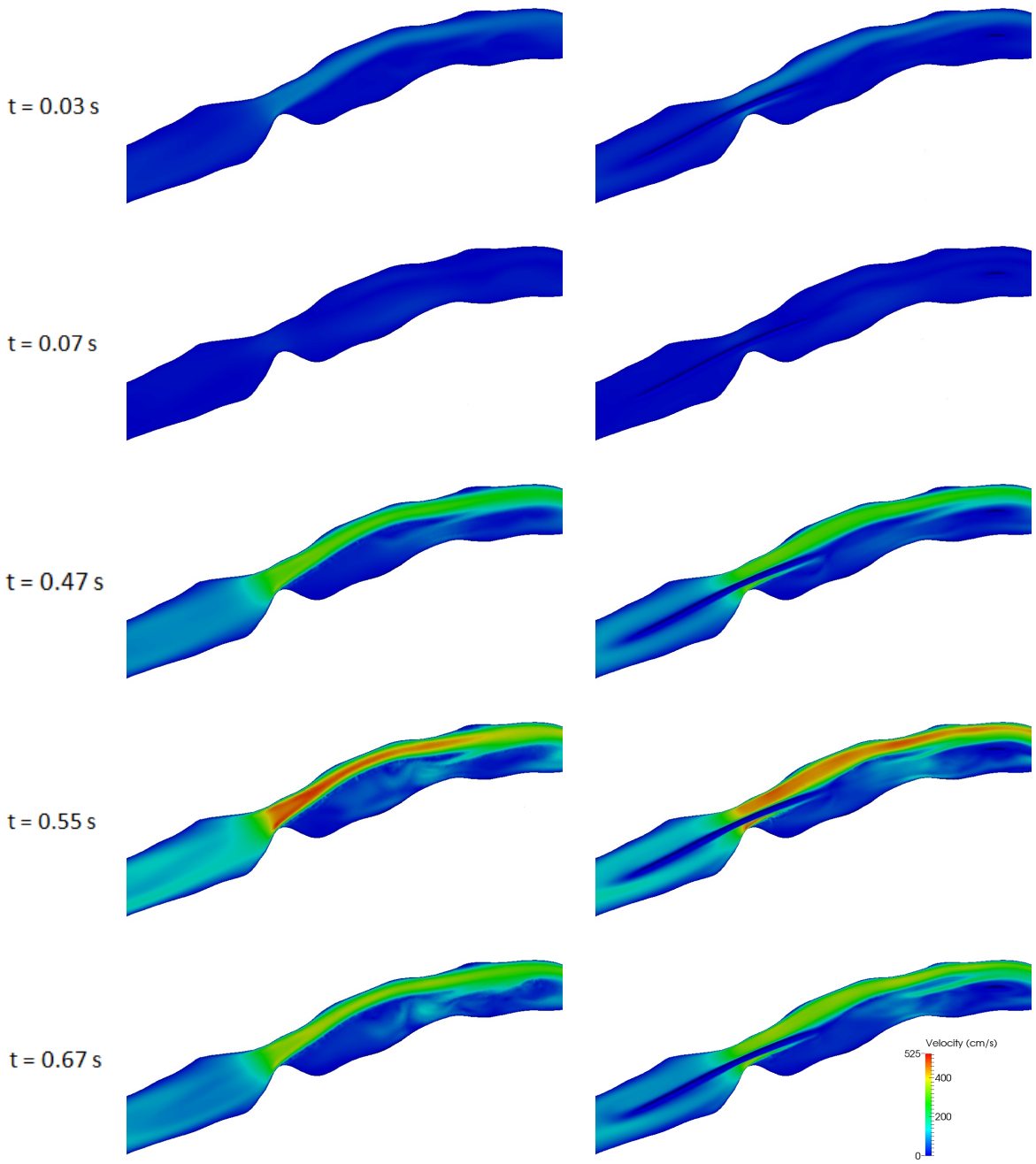

Figure 4.18: Velocity field for the Stenotic (left) and Stenotic pwg (right) case at five different instant: pre-systolic point $t = 0.03\ s$ (first row), systolic point $t = 0.07\ s$ (second row), early diastole $t = 0.48\ s$ (third row), diastolic peak $t = 0.55\ s$ (fourth row) and post-diastolic phase $t = 0.67\ s$ (fifth row).

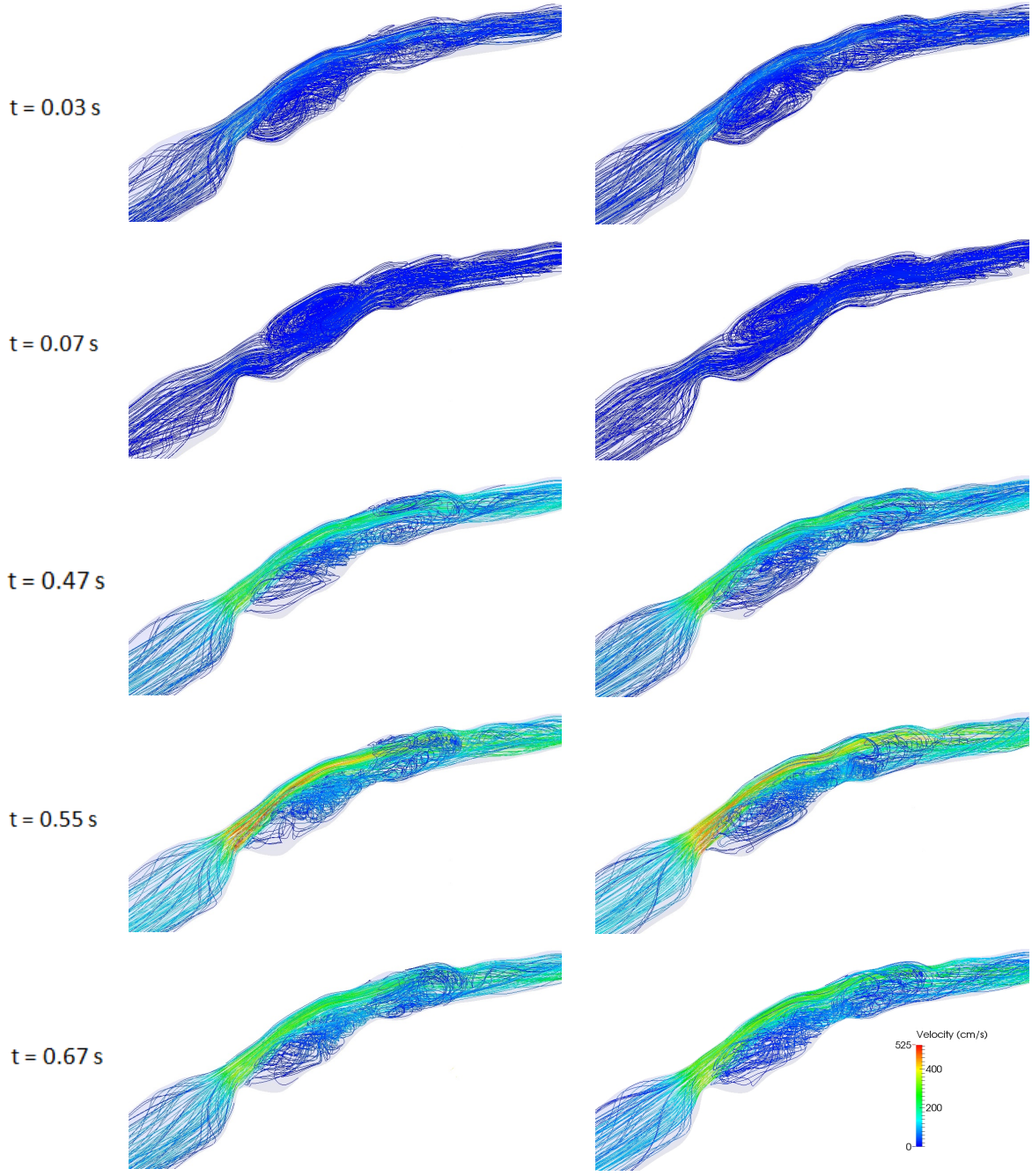

Figure 4.19: Streamlines for the Stenotic (left) and Stenotic pwg (right) case at five different instant: pre-systolic point $t = 0.03\ s$ (first row), systolic point $t = 0.07\ s$ (second row), early diastole $t = 0.48\ s$ (third row), diastolic peak $t = 0.55\ s$ (fourth row) and post-diastolic phase $t = 0.67\ s$ (fifth row).

Chapter 5

Limitations and possible improvements

In this final chapter we describe the limits of our computational work and possible future developments of this thesis.

5.1 Limitations

Our numerical simulations have some limitations that require further examination. We recall the assumptions made in Chapter 2: in all our work, we have considered blood as a Newtonian, homogenous, incompressible fluid. Moreover we have assumed rigid walls of the vessels, but we should not forget that real vessels are influenced also by the effect of the compliance. A modeling approach for this case is to use fluid structure interaction.

Moreover, we know that our computational study was performed on the model with and without guide wire only considering the reconstruction of the stenotic vessel, which departs from the aorta and ends as distally as possible from the stenosis. We have neglected all the bifurcations and therefore all the branches that depart from the nodes and do not reach the stenotic zone. However, through the use of VMTK, it is possible to carry out a more complete reconstruction of the coronary tree visible from the CT scan at our disposal. The final result in our case is shown in Figure 5.1. A more complete work should consider simulations on this geometry, because blood flow is redistributed through the different bifurcations and this could have repercussions on the pressure drop due to the presence of the stenosis. In the next section we show a possible way to deal with this problem, in particular we carry out a theoretical study in order to find suitable boundary conditions to impose at the outlets. The limitation in considering the geometry of Figure 5.1 for our numerical experiments was the creation of the mesh for the configuration which considers the presence of the guide. In fact, the procedure described in Subsection 3.3.2 goes well only if we consider a single vessel without any bifurcation. For this reason, in this first preliminary study, we decide to consider only the stenotic vessel.

Another thing to keep in mind is that, in the medical practice, the pressure guide wire is pushed as far as possible from the stenosis (at a certain point the diameter of the coronary is so small that the guide could not pass over). At this point, which is the more distal point from the stenosis, the pressure value p_d is recorded. We recall that our model ends as distally as possible from the stenosis, but, anyway, it comes from a truncation of the coronary branch and for this reason, the point in which we evaluate the pressure do not precisely correspond

to that of the medical practice.

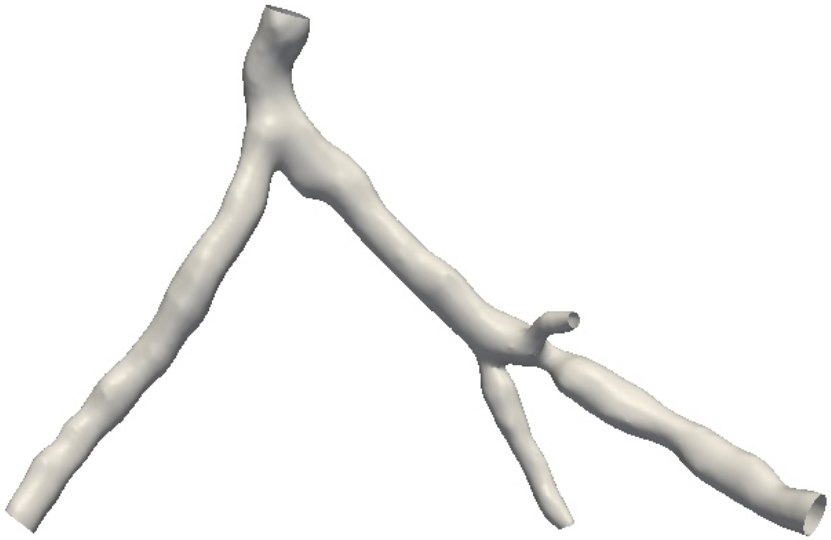

Figure 5.1: The reconstruction of the coronary tree from the CT scan at our disposal.

5.2 Possible improvements

In this section we describe two possible ways which could lead to a general improvement of our results.

5.2.1 Flow extensions

The first thing we can do is to consider the so-called *flow extensions*, which are cylindrical extensions added to the inlets of a model. They have an important role, because they ensure that the flow is fully developed when it enters the computational domain and, in this way, the solution in the vessel is not influenced by the imposed boundary conditions.

The lenght L_h that have to be added to the vessels inflow can be estimated using a semi-empirical law valid for steady laminar flow [56]:

$$\frac{L_h}{D} = 0.05\, Re,$$

where Re is the Reynolds number and D is the diameter.

5.2.2 Considerations about outflow boundary conditions

In this subsection we present a possible way to choose suitable outflow boundary conditions if we consider a model of the coronary tree with bifurcations. Often, in numerical simulation, zero-pressure boundary conditions on all the outlets of the model is used for its semplicity,

but this is not entirely correct from a physical point of view because it neglects the change in pressure which happens during blood flow. In particular, we have to take in account the mechanism of autoregulation, which, in basal conditions, allows the accomodation of the same blood flow in a stenotic vessel and in the case of a normal one. This is a fundamental mechanism in order to satisfy the myocardium demand of oxygen and is reached by the vasodilatation of the microcirculation, that leads to a reduction in the microvasculature resistance. In hyperemic conditions this reduction reaches its physiological limit and the mechanism of autoregulation does not work as in the basal case.

For this reason, if we consider the reconstruction of the coronary tree of Figure 5.1 or, in general, a model with some bifurcations, the value of the pressure we have to impose at the outlet surface of the stenotic branch could not be the same as the value imposed at the end of the healthy branches. In order to try to understand how we can find a more correct value of the pressure at the outlets, we have to take into account how pressure changes through an healthy or a stenotic vessel. On this purpose we make a theoretical study considering a simplified case.

In Figure 5.2 we represent our schematic situation. We make the hypotesis to have a coronary vessel which divides into three branches with more or less the same diameter. The same geometrical configuration is assumed also at the outlets sections of the vessels (positioned in correspondence of the dashed red line).

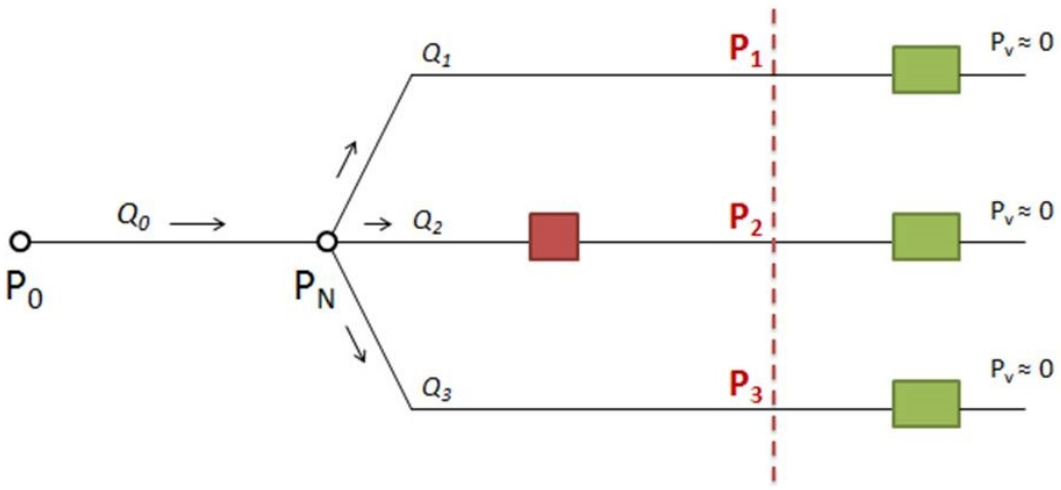

Figure 5.2: Schematic representation of the situation.

If we observe Figure 5.2, P_0 is the pressure at the beginning of the branch, whereas P_N is the pressure in the node N. From the node N depart the three branches. The branch 1 and 3 are healthy, branch 2, instead, has a stenosis. We indicate with a rectangle the pressure losses, in red the one due to the stenosis (localized loss, expressed by $\Delta P_{sten} = R_{sten1}(Q_2)^2 + R_{sten2}Q_2$), in green those due to the presence of the microcirculation (distributed losses, expressed by $\Delta P^i_{perf} = R^i_{perf}Q_i$ for $i = 1, 2, 3$). The venous pressure P_v, that is the pressure after the microvasculare region, can be assumed equal to zero.

At the node N we can apply the continuity equation for a incompressible fluid in a steady flow, that is, blood flow divedes into three parts, in such a way that

$$Q_0 = Q_1 + Q_2 + Q_3. \tag{5.1}$$

We now analyzed the pressure drop $\Delta P = P_N - P_V$ in the three branches. In this context, we cite the work of Zerbini [22], which provides a qualitative energy balance when a stenotic artery is present.

(a) Pressure drop ΔP in the healthy vessels: branch 1 and branch 3.

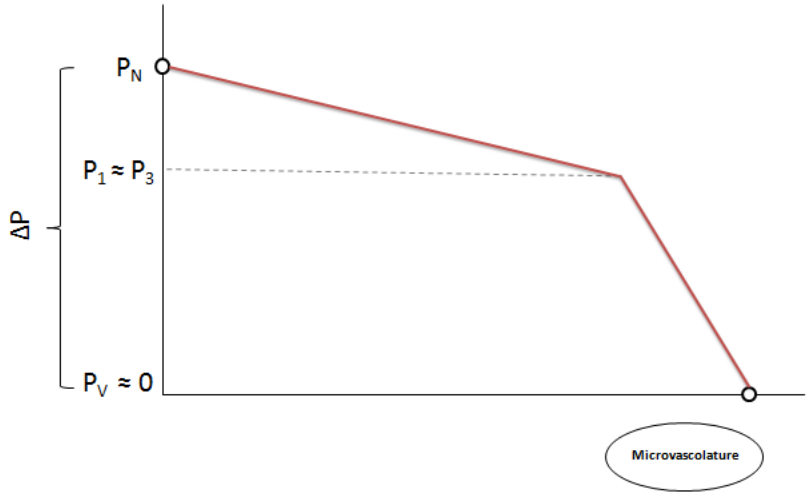

Figure 5.3: Representation of the pressure variation in an healthy vessel.

Since we are considering healthy branches with quite the same geometrical characteristics (namely, diameter and length), it is reasonable to think that $P_1 \sim P_3$.

- branch 1: the total pressure drop is detemined by the sum of distal pressure $\Delta P^1_{dist} = P_N - P_1$ and the pressure drop due to the perfusion of the microvasculature $\Delta P^1_{perf} = P_1 - P_v$, that is

$$\Delta P = \Delta P^1_{dist} + \Delta P^1_{perf} = (R_{dist} Q_1) + (R^1_{perf} Q_1). \tag{5.2}$$

- branch 3: the total pressure drop is detemined by the sum of distal pressure $\Delta P^3_{dist} = P_N - P_3$ and the pressure drop due to the perfusion of the microvasculature $\Delta P^3_{perf} = P_3 - P_v$, that is

$$\Delta P = \Delta P^3_{dist} + \Delta P^3_{perf} = (R_{dist} Q_3) + (R^3_{perf} Q_3). \tag{5.3}$$

(b) Pressure drop ΔP in a stenotic vessel: branch 2.

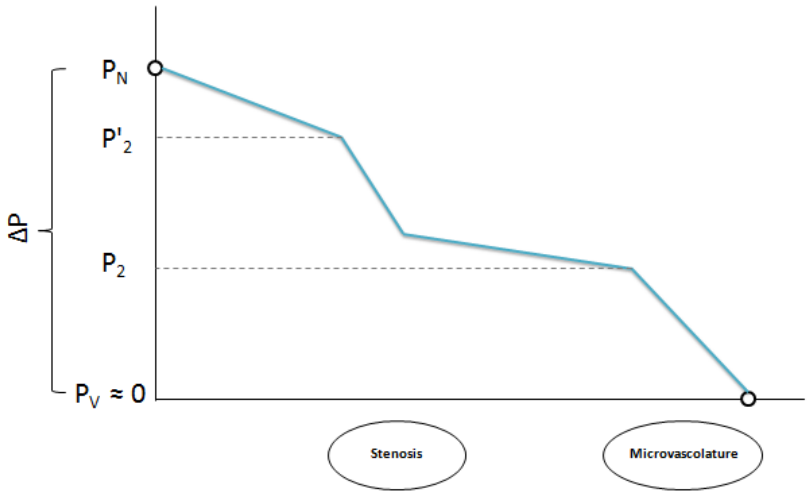

Figure 5.4: Representation of the pressure variation in a stenotic vessel.

The total pressure drop in this case is detemined by the sum of distal pressure $\Delta P^2_{dist} = P_N - P_2^{'}$, the pressure drop due to the presence of the stenosis $\Delta P_{sten} = P_2^{'} - P_2$ and that due to the perfusion of the microvasculature $\Delta P^2_{perf} = P_2 - P_v$, that is

$$\Delta P = \Delta P^2_{dist} + \Delta P_{sten} + \Delta P^2_{perf} = (R_{dist}Q_2) + (R_{sten1}(Q_2)^2 + R_{sten2}Q_2) + (R^2_{perf}Q_2). \tag{5.4}$$

We visualize the two cases, (a) and (b), in a single graph, making a distinction between the basal and the hyperemic case. We have to take in mind that we are under the assumption of three branches with more or less the same diameter.

Basal flow

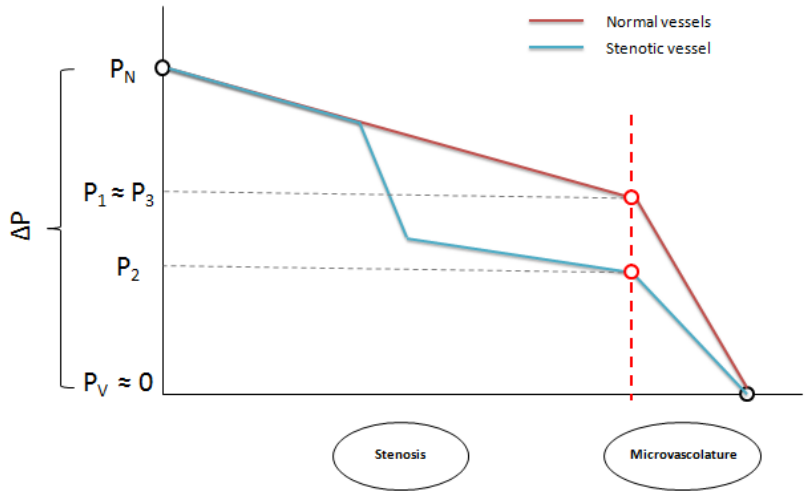

Figure 5.5: Qualitative scheme of the pressure drop: basal case.

In basal conditions, the resistance of the microcirculation R^i_{perf} for $i = 1, 2, 3$ are not the same. We can assume $R^1_{perf} \sim R^3_{perf}$ for the similar configuration of the microcirculation feeded by the vessels , but R^2_{perf} in the stenotic branch has a different value. In fact, in the presence of a stenosis, the system reacts by reducing the microvasculature resistance in order to maintain the same amount of blood flow as in the healthy case.

The dashed red line in Figure 5.5 indicates the points where our outlet surfaces are located. We can simply see that the pressure we have to impose at the outlet of an healthy vessel (i.e. P_1 and P_3) and at the outlet of a stenotic one (i.e. P_2) are not the same. The value of P_2 must be lower than that of P_1 and P_3. We prove this fact with mathematical relations, considerind the branches 1 and 2. The same considerations holds also for the healty branch 3 instead of branch 1.

Comparing equations (5.2) and (5.4), we can write:

$$(R_{dist}Q_1) + (R^1_{perf}Q_1) = (R_{dist}Q_2) + (R_{sten1}(Q_2)^2 + R_{sten2}Q_2) + (R^2_{perf}Q_2),$$

$$Q_1(R_{dist} + R^1_{perf}) = Q_2(R_{dist} + R_{sten1}Q_2 + R_{sten2} + R^2_{perf}). \tag{5.5}$$

Since we are considering three vessels with quite the same geometrical configuration, due to the autoregulation mechanism we should assume:

$$Q_1 \sim Q_2 \sim Q_3. \tag{5.6}$$

For this reason, (5.5) becomes

$$R_{dist} + R^1_{perf} = R_{dist} + R_{sten1}Q_2 + R_{sten2} + R^2_{perf},$$

in particular

$$R^1_{perf} = R_{sten1}Q_2 + R_{sten2} + R^2_{perf}.$$

Since $R_{sten1}Q_2 + R_{sten2} > 0$, we conclude that $R^2_{perf} < R^1_{perf}$ and, since $Q_1 \sim Q_2$, we have

$$P_2 - P_v = R^2_{perf}Q_2 < R^1_{perf}Q_1 = P_1 - P_v.$$

We conclude

$$P_2 < P_1.$$

We would like to know if there is a relation between these two different values of pressure. On this purpose, we make a balance between the end of each vessel (indicated by the dashed red line) and after the microvasculature, we obtain:

$$P_1 - P_v = R^1_{perf}\, Q_1,$$

$$P_2 - P_v = R^2_{perf}\, Q_2,$$

$$P_3 - P_v = R^3_{perf}\, Q_3.$$

We conclude that, under basal flow conditions, we have to find the values of pressure which guarantee the same flow rate in all the three branches (5.6). The value of P_2 will result lower than that of P_1 and P_3.

Hyperemic flow

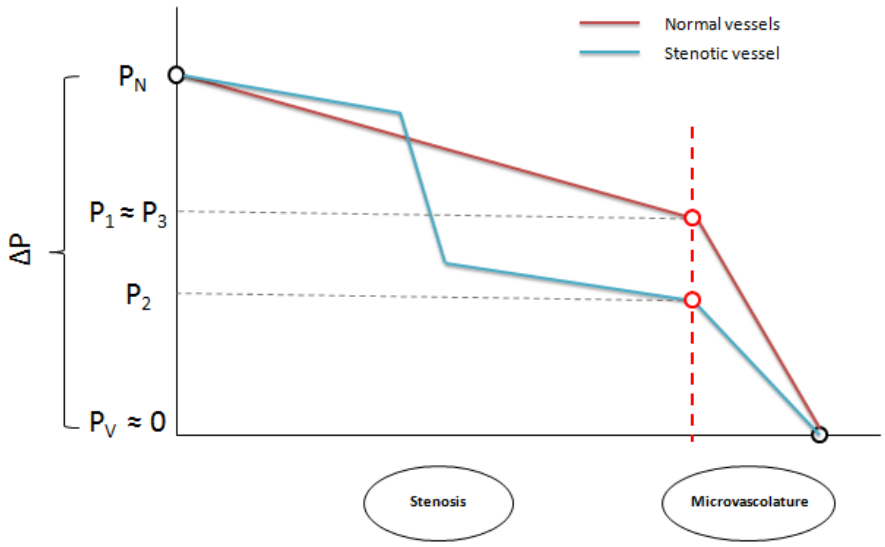

Figure 5.6: Qualitative scheme of the pressure drop: hyperemic case.

Now we suppose to be in hyperemic conditions. We recall that in this particular conditions the myocardial resistance is minimal and could be considered constant, that is, we can assume $R^{'} = R^1_{perf} = R^2_{perf} = R^3_{perf}$. If we observe Figure 5.6, we can simply detect that also in this case the value of pressures P_1 and P_3 with respect to P_2 is not the same. As in the basal case, P_2 must be lower than P_1 and P_3. We demonstrate it by means of mathematical relations. We start comparing (5.2) and (5.4). The apex h stands for indicate that we are considering the hyperemic flow.

$$(R_{dist}Q^h_1) + (R^{'}Q^h_1) = (R_{dist}Q^h_2) + (R_{sten1}(Q^h_2)^2 + R_{sten2}Q^h_2) + (R^{'}Q^h_2),$$
$$Q^h_1(R_{dist} + R^{'}) = Q^h_2(R_{dist} + R_{sten1}Q^h_2 + R_{sten2} + R^{'}). \tag{5.7}$$

In this case, the autoregulation mechanism does not work as in the basal case, and, surely,

$$Q^h_1 \neq Q^h_2.$$

But, since

$$R_{dist} + R^{'} < R_{dist} + R_{sten1}Q^h_2 + R_{sten2} + R^{'},$$

from (5.7), we can conclude

$$Q^h_2 < Q^h_1.$$

In this way

$$P_2 - P_v = R^{'}Q^h_2 < R^{'}Q^h_1 = P_1 - P_v.$$

So we can conclude that, also in the hyperemic case,

$$P_2 < P_1.$$

As done for the basal case, we would like to know if there is a relation between these two different values of pressure. We make a balance between the end of each vessel (dashed red line) and after the microvasculature:

$$P_1 - P_v = R^{'} Q_1^h,$$

$$P_2 - P_v = R^{'} Q_2^h,$$

$$P_3 - P_v = R^{'} Q_3^h.$$

Now, knowing that $R^{'}$ is the same and assuming the venous pressure $P_v \sim 0$, we can write

$$\frac{P_1}{Q_1^h} = \frac{P_2}{Q_2^h} = \frac{P_3}{Q_3^h}.$$

Assuming that $P_1 \sim P_3$ and $Q_1^h \sim Q_3^h$ because are both healthy branch with the same dimensions, the hyperemic condition on the pressure drop will be:

$$\frac{P_1}{P_2} = \frac{Q_1^h}{Q_2^h} \qquad \text{or} \qquad \frac{P_3}{P_2} = \frac{Q_3^h}{Q_2^h}. \tag{5.8}$$

We conclude that, in hyperemic conditions, we have to find two pressure values such that relation (5.8) is satisfyed.

So we conclude that, when we deal with a model with bifurcations, in presence of a stenotic branch, we must not impose the zero-pressure condition at all the outlets. If we are under the assumptions of our theoretical considerations (that is, vessels with quite the same geometrical configuration), we have to find the correct value of the pressure to impose at the outlet of the stenotic branch with respect to the healthy vessels. In particular:

- in basal conditions, we have to impose different pressure values in such a way that this choice guarantees the same flow rate in each vessel;
- in hyperemic conditions, we have to find two pressure values which ratio equals the ratio between the two hyperemic flow measured at the outlets, in order to satisfy (5.8).

In both cases, we have to face an inverse problem and the value of the pressure at the outlet of the stenotic branch will be lower than that at the outlet of the healthy ones.

Our analysis considers a simplified situation of three vessels with quite the same dimensions. If we consider a real case as in Figure 5.1 where we have branches with different geometries, things become even more complex because we need some informations about how blood flow redistributes through different areas.

Conclusions

Our aim was that to point out the effects of the guide wire on the pressure drop in a real reconstructed coronary stenosis. According to our approach, the variation of the pressure drop along the stenotic vessel minimally changes if we consider the two configurations with and without guide wire. The influence of the latter, therefore, would seem to be negligible.

It is important to consider these results in the context of our hypothesis and approximations, namely blood as a Newtonian, homogenous, incompressible fluid and rigid walls of the vessels. Moreover, our computational study was carried out only considering the stenotic vessel, neglecting in this way all the bifurcations of the model and the fact that blood flow redistributes through the different branches.

In the final chapter we have discussed some possible improvements which could make the simulations more close to what happens in the medical practice. In particular, results could change if we consider not only the stenotic vessel, but the reconstruction of Figure 5.1 with all the bifurcations. Our study is only a preliminary work on this field and, surely, by relaxing some of our assumptions, we could better simulate the medical practice of the FFR detection.

Furthermore, another thing to take in mind is that we perform only simulations first order accurate in time and, of course, by means of second order numerical simulations, we could get more precise results.

There are also other aspects which could be taken into account in future works in order to try to give an explanation of the wide dispersion of the FFR data we see in Figure (1.13). For example, it could be interesting to see if factors like the position of the stenosis in the vessel (at the beginning of the coronary, at the end, after a bifurcation, etc) or the shape of the stenosis itself (symmetrical or asymmetrical) somehow influence the measurement of the pressure drop.

Bibliography

[1] Nico H.J. Pijls, Bernard de Bruyne, *Coronary Pressure*, Springer Nature, 1997.

[2] J.R. Levick, *An Introduction to Cardiovascular Physiology*, Butterworth and co (Publishers) Ltd, 1991.

[3] Gerard J. Tortora, Bryan Derrickson, *Principles of Anatomy and Physiology.*

[4] Alfio Quarteroni, Alberto Valli, *Numerical Approximation of Partial Differential Equations*, Springer, 1994.

[5] Alfio Quarteroni, *Numerical Models for Differential Problems*, Volume 2, Modeling, Simulation & Applications.

[6] Mitsuyasu Terashima, H. Kaneda, T. Suzuki, *The role of Optical Coherence Tomography in Coronary Intervention*, Korean J Intern Med 2012, 27:1-12.

[7] Riccardo Neri, Matteo Cassin, Vasile Sirbu, Giulio Guagliumi, Sergio Mondillo, Gian Luigi Nicolosi, *Tomografia a coerenza ottica (OCT) delle arterie coronariche*, 1043-1071.

[8] C.G. Caro, T.J. Pedley, R.C. Schroter and W.A. Seed, *The Mechanics of the Circulation*, Second Edition, Cambridge University Press.

[9] Xuming Dai, Szymon Wiernek, James P. Evans, MArschall S Runge, *Genetics of coronary artery disease and myocardial infarction*, Wourld Journal of cardiology 2016, 8(1):1-23.

[10] Yohanes Adiputra, Shao-Liang Chen, *Clinical Relevance of Coronary Fractional Flow Reserve: Art-of-state*, Chinese Medical Journal, May 20,2015, Volume 128.

[11] R.F. Wilson, K. Wyche, B.V. Christensen, S. Zimmer, D.D. Laxson *Effects of Adenosine on Human Coronary Arterial Circulation*, Circulation 1990, 82:1595-1606.

[12] Bernard de Bruyne, Jozef Bartunek, Stanislas U. Sys, Nico H.J. Pijls, Guy R. Heyndrickx, William Wijns, *Simultaneous Coronary Pressure and Flow Velocity Measurements in Humans*, Circulation 1996, 94:1842-9.

[13] K. Lance Gould, Kirk Lipscomb, Glen W. Hamilton, *Instantaneous Flow Response and Regional Distribution During Coronary Hyperemia as Measures of Coronary Flow Reserve*, The American Journal of cardiology, 1974.

[14] H.J. Kim, I.E. Vignon-Clementel, C.A. Figueroa, K.E. Jansen, C.A. Taylor, *Developing computational methods for three-dimensional finite element simulations of coronary blood flow*, Finite Element in Analysis and Design 46 (2010), 514-525.

[15] C.A. Taylor, C.A. Figueroa, *Patient-Specific Modeling of Cardiovascular Mechanics*, Annual Review of Biomedical Engineering, 2009, Vol.11:109-134.

[16] Wilbert Aarnoudse, William F. Fearon, Ganesh Manoharan, Maartje Geven, Frans van de Vosse, Marcel Rutten, Bernard de Bruyne, Nico H.J. Pijls, *Epicardial Stenosis Severity Does Not Affect Minimal Microcirculatory Resistance*, American Heart Association, 2004.

[17] Nico H.J. Pijls, Jacques A.M. van Son, Richard L. Kirkeeide, Bernard de Bruyne, K. Lance Gould, *Experimental Basis od Determining Maximum Coronary, Myocardial, and Collateral Blood Flow by Pressure Measurements for Assessing Functional Stenosis Severity Before and After Percutaneous Transluminal Coronary Angioplasty*, Circulation, 1993, 1354-1367.

[18] B. Guerciotti, C. Vergara, S. Ippolito, A. Quarteroni, C. Antona, R. Scrofani, *Computational study of the risk of restenosis in coronary bypass*, Biomechanics and Modeling in Mechanobiology, 2016, 16:313-332.

[19] A.Quarteroni, A. Manzoni, C. Vergara, *The cardiovascular system: Mathematical modelling, numerical algorithms and clinical applications*, MOX report, n. 38, 2016.

[20] Tecchio Allegra, *Pressure variations in real stenotic coronaries: a computational study*, Master Thesis, 2017.

[21] Stella Simone, *Computational study of the influence of the pressure guide wire on the coronary pressure*, Master Thesis, 2017.

[22] Zerbini Matteo, *Fractional Flow Reserve estimation in stenotic coronaries: a computational study of the influence of the pressure guidewire*, Master Thesis, 2018.

[23] A. Quarteroni, M. Tuveri, A. Veneziani, *Computational vascular fluid dynamics: problems, models and methods*, Computing and Visualization in Science, 163-197, march 2000.

[24] A. Quarteroni, L.Formaggia, *Mathematical modelling and numerical simulation of the cardiovascular system*, 2002.

[25] F.J.H. Gijsen, F.N. van de Vosse, J.D: Jansssen, *The influence of the non-Newtonian properties of blood on the flow in large arteries: steady flow in a carotid bifurcation model*, Journal of Biomechanics 1999, 32:601-608.

[26] Sethuraman Sankaran, Hyun Jin Kim, Gilwoo Choi and Charles A. Taylor, *Uncertainty quantification in coronary blood flow simulations: impact of geometry, boundary conditions and blood viscosity*, Journal of Biomechanics, http://dx.doi.org/10.1016/j.jbiomech.2016.01.002.

[27] Shyam Srinivasan, Deepa Madathil, *3-Dimensionale Computational Study of Blood Flow in Pathophysiologically affected Arteries simulated in OpenFOAM*, 2016.

[28] Youcef Saad, Martin H. Schultz, *GMRES: a generalized minimal residual algorithm for solving nonsymmetric linear system*, SIAM Journal ofn Scientific and Statistical Computing, 7(3):856-869, July 1996.

[29] Marzio Sala, Michael Heroux, *Robust algebraic preconditioners using IFPACK 3.0*, 2005.

[30] Alfio Quarteroni, Riccardo Sacco, Fausto Saleri, *Matematica numerica*, Springer-Verlag, 2008.

[31] www.vmtk.org.

[32] D.J. Withey, Z.J. Koles, *Medical Image Segmentation: Methods and Software*, 2007.

[33] Tenn Francis Chen, *Medical Image Segmentation using Level Sets*, Technical Report, 2008.

[34] Susanna Migliori, Claudio Chiastra, Marco Bologna, Eros Montin, Gabriele Dubini, Cristina Aurigemma, Roberto Fedele, Francesco Burzotta, Luca Mainardi, Francesco Migliavacca, *A framework for computational fluid dynamic analyses of patient-specific stented coronary arteries from optical coherence tomography images*, Medical Engineering and Physics 47 (2017), 105-116.

[35] Liang Wang, Dalin Tang,Akiko Maehara, Zheyang Wu, Chun Yang, David Muccigrosso, Jie Zheng, Richard Bach, Kristen L. Biliar, Gary S. Mintz, *Fluid-structure interaction models based on patient specific IVUS at baseline and follow-up for prediction of coronary plaque progression by morphological and biomechanical factors: A preliminary study*, Journal of Biomechanics, 2018.

[36] D.A. Steinman, *Image-based computational fluid dynamics modeling in realisticarterial geometries*, Annals of Biomedical Engineering, 30:483-497, 2002.

[37] C.A. Taylor, D.A. Steinman, *Image-based modeling of blood flow and vessel wall dynamics: applications, methods and future directions*, Annals of Biomedical Engineering: sixth International Bio-Fluid Mechanics Symposium and Workshop, March 28-30, 2008 Pasadena, California, 38(3): 1188-1203, 2010.

[38] E. Boutsianis, H. Dave, T. Frauenfelder, D. Poulikakos, S. Wildermuth, M. Turina, Y. Ventikos, G. Zund, *Computational simulation of intracoronary flow based on real coronary geometry*, European Journal of Cardio-Thoracic Surgery, 2004, 248-256.

[39] P.D. Morris, A. Narracott, H. von Tengg-Kobligk, D.A.S. Soto, S. Lungu, P. Evans, N.W. Bressloff, P.V. Lawford, D.R. Hose, J.P. Gunn, *Computational fluid dynamics modelling in cardiovascular medicine*, BMJ Journals, Volume 102, Issue 1.

[40] Panaglotis K. Siogkas, Michail I. Papafaklis, Antonis I. Sakellarios, Kostas A. Stefanou, Christos V. Bourantas, Lambros S. Athanasiou, Therim P. Exarchos, Katerina K. Naka, Lampros K. Michalis, Oberdan Parodi, Dimitrios I. Fotiadis, *Patient-Specific Simulation of Coronary Artery Pressure Measurements: An In Vivo Three-Dimensional Validation Study in Humans*, BioMed Research International, 2015.

[41] Ettienne Boileau, Sanjay Pant, Carl Roobottom, Igor Sazonov, Jingking Deng, Xianghua Xie, Perumal Nithiarasu, *Estimating the accuracy of a reduced-order model for the calculation of fractional flow reserve (FFR)*, Int J Numer Meth Biomed Engng, 2018.

[42] Eric K.W. Poon, Umair Hayat, Vikas Thondapu, Andrew S.H. Ooi, Muhammad Asrar Ul Haq, Stephen Moore, Nicolas Foin, Shengxian Tu, Cheng Chin, Jason P. Monty,

Ivan Marusic and Peter Barlis, *Advances in three-dimensional coronary imaging and computational fluid dynamics: is virtual fractional flow reserve more than just a pretty picture?*, Coronary Artery Disease 2015, Vol 26 Supplement 1.

[43] Paul D. Morris, Desmond Ryan, Allison C. Morton, Richard Lycett, Patricia V. Lawford, D. Rodney Hose, Julian P. Gunn, *Virtual Fractional Flow Reserve From Coronary Angiography: Modeling the Significance of Coronary Lesions*, JACC: CARDIOVASCULAR INTERVENTION, 2013.

[44] Charles A. Taylor, Timothy A. Fonte, James K. Min, *Computational Fluid Dynamics Applied to Cardiac Computed Tomography for Noninvasive Quantification of Fractional Flow Reserve*, Journal of the American College of Cardiology, Vol.61, No.22, 2013.

[45] Alina G. van der Giessen, Harald C. Groen, Pierre-Andrè Doriot, Pim J. de Feyter, Antonius F.W. van der Steen, Frans N. van de Vosse, Jolanda J. Wentzel, Frank J.H. Gijsen, *The influence of boundary conditions on wall shear stress distribution in patients specific coronary trees*, Journal of Biomechanics, 2011, 1089-1095.

[46] Rupak K. Banerjee, Koustubh D. Ashtekar, Tarek A. Helmy, Mohamed A. Effat, Lloyd H. Back, Saeb F. Khoury, *Hemodynamic diagnostics of epicardial coronary stenosis: in-vitro experimental and computational study*, BioMedical Engineering Online, 2008.

[47] Kimmel SE, Localio AR, Krone RJ, Laskey WK, *The effects of contemporary use of coronary stents on in-hospital mortality. Registry Committee of the Society for Cardiac Angiography and Interventions*, Journal of the American College of Cardiology, 2001, 499-504.

[48] Rupak K. Banerjee, Abhijit Sinha Roy, Lloyd H. Back, Martin R. Back, Saeb F. Khoury, Ronald W. Millard, *Characterizing momentum change and viscous loss of a hemodynamic endpoint in assessment of coronary lesions*, Journal of Biomechanics 40(2007), 652–662.

[49] OpenStax College, *Anatomy and Physiology*, OpenStax CNX.

[50] A. Quarterioni, C. Vergara, *Computational models for hemodynamics*, MOX-Report, No. 23/2017.

[51] Vincenzo Casulli, Eleuterio Toro, Michael Dumbser, *Semi implicit numerical modeling of axially symmetric flows in compliant arterial systems*, Numerical Methods in Biomedical Engineering, 2011.

[52] L. Bertagna, S. Deparis, L. Formaggia, D. Forti,A. Veneziani, *The LifeV library: engineering mathematics beyond the proof of concept*, MOX Report, No. 53/2017.

[53] www.lifev.org.

[54] Abhijit Sinha Roy, Rupak K. Banerjee, Lloyd H. Back, Martin R. Back, Saeb Khoury, Ronald W. Millard, *Delineating the guide-wire flow obstruction effect in assessment of fractional flow reserve and coronary flow reserve measurements*, Am J Physiol Heart Circ Physiol 289, H392-H397, 2005.

[55] Sarfaraz Kamangar, Irfan Anjum Badruddin, N.Ameer Ahamad, Kalimuthu Govindaraju, N. Nik-Ghazali, NJ. Salman Ahmes, A. Basarudin, T.M. Yunus Khan, *The Influence of Geometrical Shapes of Stenosis on the Blood Flow in Stenosed Artery*, Sains Malaysiana 46(10)(2017), 1923–1933.

[56] Yunus A. Cengel, John M. Cingala, *Fluid mechanics: fundamentals and applications*, Mcgraw-Hill, First Edition, 2006.